Experimental investigation and modal analysis of the wake behind a flat-back Ahmed body

by

Chin Wang Chen

A thesis submitted in partial fulfillment of the requirements for the degree of

Master of Science

Department of Mechanical Engineering
University of Alberta

Abstract

To enhance the aerodynamic performance of a vehicle, a fundamental understanding of the flow is required. This can be achieved through flow characterization of simplified models such as the Ahmed body. However, uncertainties regarding the topology of flow motions in the wake persist due to the limitations of previous measurement and analysis methods. In this research, the three-dimensional wake flow behind a flat-back Ahmed body is investigated at Re_H = 10,000, based on the freestream velocity and the height of the body, H. The flow was measured using planar and time-resolved tomographic particle image velocimetry measurements, and subsequently analyzed using two modal decomposition techniques.

The current proper orthogonal decomposition (POD) analysis indicates that the most energetic flow motion is attributed to the well-known bi-stability, accounting for 9.1% of the total turbulent kinetic energy of the wake flow. It is followed by other flow motions with energy below 1.5%, such as vortex shedding. In the current study, the lack of temporal coherence in spatial patterns obtained from POD was addressed by employing its space-time formulation, known as spectral proper orthogonal decomposition (SPOD).

The coherent flow motions at each discrete St_H within the range of 0.007 to 1.228 are characterized using SPOD analysis, where St_H is the Strouhal number based on H. The analysis has discerned the known flow motions, including bi-stability, vortex shedding, and shear layer instability, each occupying a specific St_H range. The bi-stability mode demonstrates the switching between two asymmetric states of the wake. Each asymmetric state is characterized by the presence of a skewed toroid vortex attached to a pair of vertically oriented counter-rotating streamwise vortices. The bistable motion also results in significant modifications to the separation bubble, which causes the

separation bubble to enlarge and elongate in the streamwise direction. Furthermore, the results reveal that the vortex shedding mechanism and shear layer instability are primarily associated with the shedding of a pair of counter-rotating quasi-streamwise vortices and toroidal vortices, respectively. Additionally, a new type of motion, namely the swirling motion, is identified at St_H between 0.014 and 0.123. Unlike the bi-stability mode, the swirling motion leads to the wake alternating between a symmetric and an asymmetric state. Its topology is characterized by two sets of counter-rotating streamwise structures that have varying orientations depending on the wake state. The swirling motion comprises both rotational motion in the crossflow plane and streamwise motion of the wake barycentre. This flow motion bears similarities to the bubble pumping and switching attempts mentioned in earlier studies. Overall, this study contributes to a more comprehensive understanding of the wake of a flat-back Ahmed body by detailing the spatiotemporal information of the high-energy flow motions.

Preface

The Ahmed body model used in the experiments was designed by me. I conducted all the experiments myself, with the assistance of PhD candidate Sen Wang. In addition to the experiments, I carried out all the analyses of the experimental data under the supervision of Dr. Sina Ghaemi. The attached figures, starting from Chapter 3 of this thesis, were generated by me. The MATLAB code for the SPOD algorithm in Appendix B was written by me, with modifications made to the original code developed by Dr. Oliver Schmidt from the University of California.

The measurements were conducted at the water flume located in the Mechanical Engineering Building at the University of Alberta. The flat plate used for installing the Ahmed body was preliminarily designed by MSc student Findlay McCormick. Furthermore, the acrylic prisms used for the measurements were 3D printed in Dr. David Nobes' laboratory.

This research was conducted in collaboration with PhD candidate Sen Wang and Dr. Sina Ghaemi, and serves as the basis for a journal publication. The paper has been submitted to the Journal of Fluid Mechanics — Cambridge University Press for the review process.

Table of contents

List of tables

Table of figures

Chapter 1. Introduction

The energy loss attributed to aerodynamic drag for ground vehicles is dissipative and non-recoverable. Therefore, reducing vehicle drag has become a priority for both governments and the automotive industry in order to mitigate fuel consumption and carbon emissions. The aerodynamic losses of heavy-duty and commercial vehicles, such as trailers and motor coaches, are significant due to their large drag area and their long-distance operation on highways. A government study shows that the aerodynamic drag can account for up to 70% of the fuel consumption of a trailer-tractor operating on a highway (Patten *et al*. 2012). Another study demonstrated a drag reduction of 11.8% for a trailer operating at 65 mph by installing a boat tail device (Patten *et al*. 2010). This reduction is equivalent to a significant fuel saving of about 7.3% and a reduction of 10,366 kg of CO2 emissions per vehicle annually.

Simplified models are widely utilized in research to investigate the aerodynamics and flow physics of road vehicles. In this regard, Ahmed *et al*. (1984) proposed a three-dimensional (3D) bluff geometry, commonly known as the Ahmed body, which incorporates only the fundamental features of a generic car. The Ahmed body is characterized by a flat front face and rounded corners that join a long rectangular body. To simulate the ground effect of the vehicle, the model is elevated above the floor with four cylindrical supports. While the rear face of the Ahmed body can adopt various slant angles to mimic different notchback configurations, the flat-back Ahmed body, with a rectangular rear face perpendicular to the flow, has gained significant prominence in fundamental investigations of vehicle aerodynamics due to its extensive applicability. In addition to the Ahmed body, several simplified models have been proposed to study specific vehicle types. These include the Windsor body (Howell, Sheppard & Blakemore, 2003), the ground transportation system (Croll *et al*., 1996), and the simplified lorry (Cabitza, 2015). Despite their varying frontal geometries and aspect ratios, these models exhibit similar wake dynamics to that of the Ahmed body.

A schematic of the flat-back Ahmed body is shown in figure 1.1. In accordance with the context of this thesis, the origin of the Cartesian coordinate system O is defined at the center of the rear face of the Ahmed body. The directions are defined as follows: x represents the streamwise direction, y represents the direction normal to the ground, and z represents the spanwise direction. The components of the instantaneous velocity are denoted as U, V, and W, following the same order as the axes of the coordinate system. Finally, the lowercase letters u, v, and w represent the fluctuating velocity components. The mean value and magnitude of any quantity are indicated as $\langle ... \rangle$ and $|...|$, respectively.

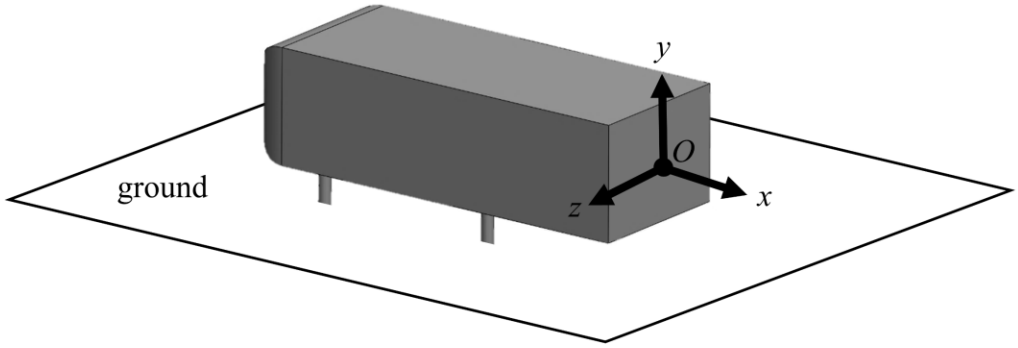

Figure 1.1 Schematic representation of a flat-back Ahmed body based on Ahmed *et al*. (1984) with the coordinate system shown.

The flat-back Ahmed body exhibits a common flow characteristic with high-drag vehicles, in which the bluntness and the abrupt geometry change result in a large region of separated flow at the rear face (Ahmed *et al.* 1984). The drag breakdown analysis by Ahmed *et al.* (1984) indicated that the low pressure acting on the rear face of a flat-back Ahmed body forms approximately 72% of the total drag force at Reynolds number of $Re_H = 1.3 \times 10^6$. Here, $Re_H = U_\infty H/\nu$ where U_∞ is the freestream velocity, H is the height of the rear face, and ν is the fluid's dynamic viscosity. At a lower Re_H of 4×10^5, a more recent investigation by Evrard *et al.* (2016) estimated that about 52% of total drag is due to the low pressure of the rear face. Despite the apparent discrepancy, both measurements highlight the importance of the low-pressure field induced by the wake dynamics.

The preliminary study by Ahmed *et al.* (1984) was limited to the time-average flow field obtained by single-port pressure and hotwire measurements with low spatial resolutions. Further insights were gained through planar particle image velocimetry (PIV) in the last two decades (e.g., Khalighi

et al. 2001; 2012; Grandemange *et al.* 2013; Volpe *et al.* 2015; Evrard *et al.* 2016; Fan *et al.* 2020; Haffner *et al.* 2020). The literature has identified several energetic flow motions in the flat-back Ahmed body's wake, such as bi-stability (Grandemange et al. 2012), vortex shedding, and bubble pumping motions (Berger *et al*., 1990; Duell & George 1999), which cover a wide range of temporal scales. Although most of these flow dynamics are indicated in the spectral analysis, their 3D topology and dynamics are subjected to different discrepancies. Still, studies have shown the potential to enhance the aerodynamic performance of the Ahmed body by attenuating the bi-stability and/or pumping motions (e.g., Duell & George *et al.* 1999; Khalighi *et al.* 2012; Grandemange *et al.* 2014; Evrard *et al.* 2016; Li *et al.* 2016; Haffner *et al.* 2020).

Several discrepancies observed in previous investigations can be attributed to the limitations of measurement techniques, including limited spatial dimensions and/or insufficient temporal resolution. For instance, previous investigations had to conjecture the complex 3D topology of the instantaneous wake and the bubble pumping mechanism due to point-wise hotwire measurements or, at best, using two-dimensional (2D) PIV measurements in a plane. To address these discrepancies, the wakes of Ahmed and Windsor models have been investigated using tomographic PIV (tomo-PIV) (Perry *et al.* 2016a; Pavia *et al.* 2020) and 3D particle tracking velocimetry (Booysen *et al.* 2022), respectively. Although the 3D flow analysis by Perry *et al.* (2016a) was preliminary, they highlighted the challenges of obtaining sufficient tracer particles and spatial-dynamic range in large-scale tomo-PIV measurements. The subsequent investigation by Pavia *et al.* (2020) attempted to address the uncertainties of the wake topology; however, these measurements were not temporally resolved. Booysen *et al.* (2022) used 3D particle tracking velocimetry (PTV) to investigate the Ahmed body wake at various side-slip angles. Due to experimental limitations, both Pavia *et al.* (2020) and Booysen *et al.* (2022) could not utilize time-resolved measurements. As a result, their 3D analyses were limited to ensemble averages and POD analysis.

Previous numerical simulations have provided 3D flow realizations with high spatial and/or temporal resolutions (e.g., Krajnovic & Davidson 2003; Khalighi *et al.* 2001; Khalighi *et al.* 2012; Lucas *et al.* 2017; Dalla Longa *et al.* 2019; Fan *et al.* 2020; Podvin *et al.* 2020; Kang *et al.* 2021). However, the short duration of these simulations due to limited computational power, poses a

significant challenge for more comprehensive investigations using different analyses, besides traditional POD and spectral analysis.

The motivation of the current research is to address uncertainties about the spatiotemporal dynamics of the wake generated by the flat-back Ahmed body. These uncertainties stem from limitations in measurement techniques and analysis methodologies used in previous investigations. To overcome these restrictions and obtain a comprehensive understanding of the flow, the current research employs time-resolved 3D velocity fields and the Spectral Proper Orthogonal Decomposition (SPOD) technique. This unique combination allows for the objective of characterizing spatiotemporal coherent structures of the flow in the frequency domain. The information obtained from the SPOD analysis is utilized to address discrepancies related to the spatiotemporal dynamics of bi-stability and bubble pumping, as well as the spatial topologies of the primary vortical structures associated with vortex shedding and shear layer instability mechanisms. The research aims to provide insights and clarity into these flow behaviors, contributing to a better understanding of the wake dynamics of the flat-back Ahmed body. The outline of the thesis is presented as follows:

Chapter 2: A literature review of the wake flow behind various simplified vehicle models, with a specific focus on the flat-back Ahmed body.

Chapter 3: The experimental methodologies include the flow facilities, measurement setups, procedures of data processing and modal decomposition techniques.

Chapter 4: The results and discussion of the wake analysis of the flat-back Ahmed body.

Chapter 5: A conclusion that highlights the important findings of the current wake analysis

Chapter 2. Simplified vehicle wake

This chapter provides an overview of previous findings from both experimental and numerical investigations on wake flows behind simplified vehicle models, with particular emphasis on the flat-back Ahmed body. The subsections begin by introducing the mean flow field and Reynolds stresses of the wake flow. Subsequently, the chapter discusses three high-energy flow motions observed in the wake flow, namely bi-stability, bubble pumping, and vortex shedding. The chapter concludes with a section presenting the background of three modal decomposition techniques that have been utilized in previous investigations.

2.1 Mean flow field

Ahmed et al. (1984) conducted a preliminary investigation of the time-averaged wake of an Ahmed body, primarily focusing on the slanted-back configuration. Their study involved measurements of pressure and velocity, which revealed a mean flow topology characterized by a triple deck system. The spatial organization of this flow system is illustrated in figure 2.1, which was redrawn by Choi *et al*. (2014). In this figure, the flow separation occurs on the rear flat-surface, resulting in the formation of two vertically oriented recirculation zones. Additionally, an increase in the taper angle of the upper trailing-edge from 5° to 30° led to flow separation on the slanted surface. In addition, their time-averaged flow measurements at various crossflow planes downstream of the Ahmed body demonstrated the presence of a low-pressure zone caused by the flow separation on the slanted surface. This low-pressure zone induces the rolling up of the top shear layers into a pair of counter-rotating longitudinal vortices that extend further downstream.

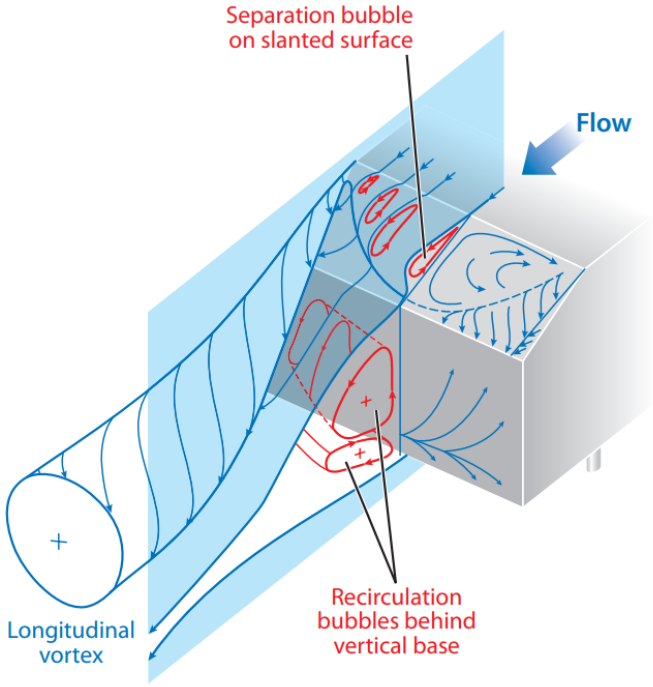

Figure 2.1 A conceptual representation of the mean vortical structures generated behind a slanted-back Ahmed body on one spanwise half of the wake, adapted from Choi *et al.* (2014) with permission.

Khalighi et al. (2001) conducted planar PIV measurements and RANS simulations of a square-back model at a Reynolds number of $Re_H = 1.7 \times 10^5$. Their findings at the horizontal symmetric plane ($y = 0$) revealed that the mean recirculation bubble is comprised of two roughly symmetrical counter-rotating vortex cores. Surprisingly, they observed that the instantaneous wake exhibits left-right asymmetry, favoring one spanwise side (Khalighi *et al.*, 2001). This discrepancy was later attributed to the introduction of long-timescale dynamics, as explained in section 2.3. The presence of left-right symmetrical mean recirculation has also been confirmed in subsequent experimental studies of the flat-back Ahmed body, including Grandemange *et al.* (2013), Volpe *et al.* (2015), Evrard *et al.* (2016), Fan *et al.* (2020), and Booysen *et al.* (2022). These investigations have visualized the rear recirculation in the vertical symmetry plane ($z = 0$) downstream of the flat-back Ahmed body, which also exhibits approximate symmetry. For instance, Fan *et al.* (2020) conducted planar PIV measurements at two symmetry planes of an Ahmed body wake at $Re_H = 9.2 \times 10^4$, as illustrated in figure 2.2. Moreover, the planar PIV measurements performed by Grandemange *et al.* (2013) and Volpe *et al.* (2015) indicated that the time-averaged wake topology is left-right symmetric when measurements are acquired over a sufficiently long duration.

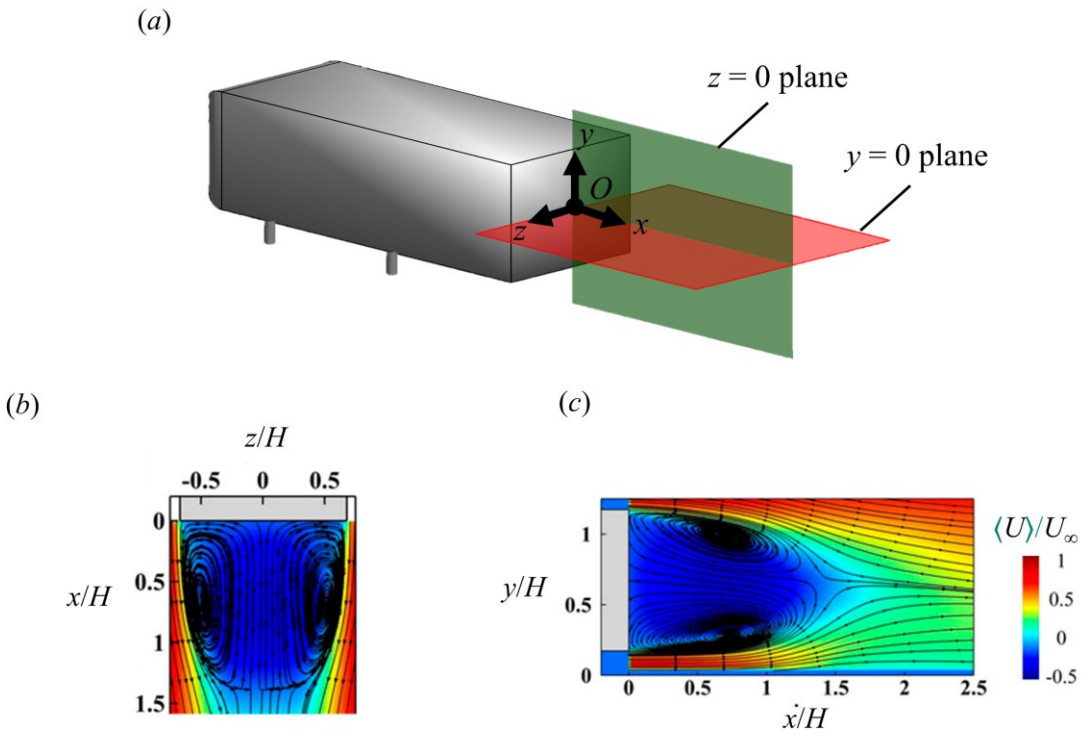

Figure 2.2 (a) Schematic representation of the measurement planes (highlighted in green and red) of planar PIV behind a flat-back Ahmed body, with the accompanying coordinate system displayed. The bottom row shows the time-averaged velocity fields of a flat-back Ahmed body wake in the (*b*) $y = 0$ plane, and (*c*) $z = 0$ plane, adapted from Fan *et al.* (2020) with permission.

At a Reynolds number of $Re_H = 9.2 \times 10^4$, planar PIV measurements conducted by Grandemange *et al*. (2013) revealed that the mean separation bubble, characterized by the region of negative streamwise velocity ($U < 0$), is confined within the rectangular base of the flat-back Ahmed body. This confinement occurs due to the equal growth of shear layers emerging from each rear edge. Remarkably, these findings align with the 3D visualization obtained from time-averaged wake topology via 3D-PTV measurements carried out by Booysen *et al*. (2022) at the same Reynolds number. In figure 2.2, a schematic of the mean separation bubble formation at the rear face of the flat-back Ahmed body is provided for clarity. Furthermore, Booysen et al. (2022) demonstrated that the mean wall-normal and spanwise velocity components exhibit enhanced prominence around the curvature of the recirculation bubble.

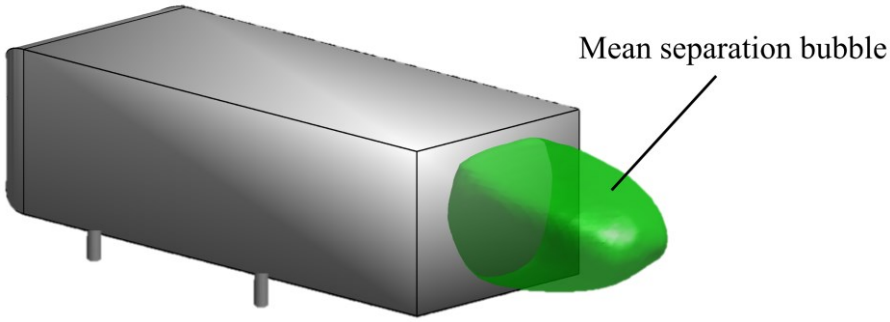

Figure 2.3 A schematic representation of the mean separation bubble forms in the wake of a flat-back Ahmed body.

The wake flow behind the Ahmed body is highly three-dimensional, which can be completely antisymmetric in certain conditions. As noted by Ahmed *et al.* (1984), the strength of bottom recirculation can vary depending on the ground clearance. Later experimental and numerical investigations of Windsor and Ahmed models also observed a top-bottom asymmetric wake due to a stronger upwash flow is promoted from the underbody, which induces a more prominent recirculating flow at the lower half of the base (Perry *et al.* 2016b; Kang *et al.* 2021). Kang *et al*. (2021) demonstrated the top-bottom flow asymmetry from a numerical simulation at $Re_H = 1.7 \times 10^4$ with a thick boundary layer upstream of $\delta_{0.99}/H = 1.7$. Here, $\delta_{0.99}$ is the boundary layer thickness based on 99% of the freestream velocity, U_∞. Their time-averaged wake flow shows a more prominent upwash and lateral flows at the bottom half of the wake, compared to the case of thin upstream boundary layer of $\delta_{0.99}/H = 0.09$.

Regarding the time-averaged vortical structures in the wake of a flat-back Ahmed body, Ahmed *et al*. (1984) proposed the formation of a toroidal vortex through the merging process of the recirculating flow at the rear face, as seen in figure 2.2 (*b*) and (*c*). This toroidal vortex corresponds to the low-pressure region within the recirculating flow. At $Re_H = 1.7 \times 10^5$, Khalighi *et al*. (2001) conducted RANS simulations of a square-back model, which visualized a toroidal pattern of significant negative pressure in the 2D mean pressure field closed to the flat rear face. Krajnovic and Davidson (2003) conducted LES simulations on a square-back model at $Re_H = 2.1 \times 10^5$, which highlighted the instantaneous structures associated with the formation of the time-averaged toroidal vortex. Evrard et al. (2016) conducted an experimental investigation using planar PIV at the near wake region of a flat-back Ahmed body. They proposed that the wake is left-right

symmetric due to the implementation of deep cavity at trailing-edge, which leads to the formation of time-averaged toroidal vortex as illustrated in figure 2.4. Subsequent experimental and numerical studies (i.e., Grandemange *et al.* 2013; Khalighi *et al.* 2012; Lucas *et al.* 2017; Dalla Longa *et al.* 2019; Fan *et al.* 2020; Kang *et al.* 2021) also observed the toroidal vortex through the visualization of negative pressure isosurfaces in the time-averaged pressure field.

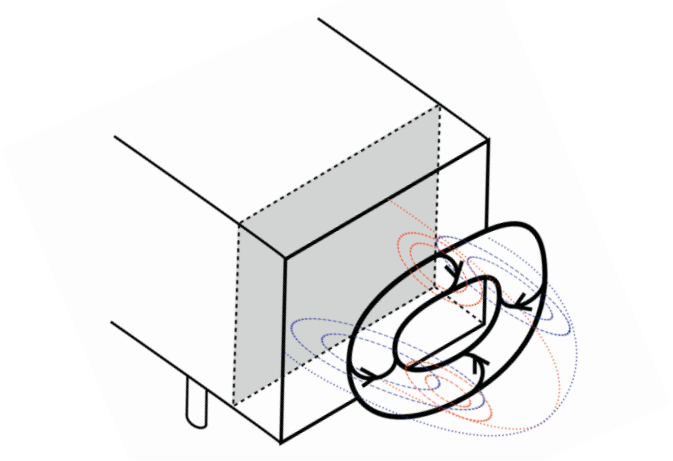

Figure 2.4 A schematic representation of the mean vortical structure in the wake of a flat-back Ahmed body, featuring a deep cavity (extended section beyond the dashed line). The conceptual drawing is adapted from Evrard *et al*. (2016) with permission.

The pair of time-averaged longitudinal vortices observed by Ahmed *et al.* (1984) in the slanted-back Ahmed body wake (see figure 2.1) are also indicated in the time-averaged wakes behind other flat-back vehicle-shaped bodies with various aspect ratios (Bearman 1997; Barlow *et al.* 1999; McArthur *et al.* 2016). Moreover, the numerical simulation by Krajnovic & Davidson (2003) showed evidences of longitudinal vortical structures from the mean flow at 3.5H downstream a square-back Ahmed body. For the flat-back model with a rectangular trailing-edge, the results of stereo-PIV measurements by Grandemange *et al.* (2013) also showed a pair of counter-rotating longitudinal vortices from the mean streamwise vorticity field at the crossflow plane of 2H downstream from the rear face, similar to the findings of Ahmed *et al.* (1984) from the slanted-back model. Grandemange *et al.* (2013) suggested that part of the induced drag is attributed to the crossflow forces caused by these longitudinal vortices.

2.2 Reynolds stresses

The experimental investigation by Grandemange *et al.* (2013) suggested that the Reynolds stresses in the shear layers contribute to a significant base drag. Their results of PIV measurements show that the streamwise normal stresses are particularly strong at the shear layers. This finding is consistent with other experimental (e.g., Khalighi *et al.* 2001; Haffner *et al.* 2020; Booysen *et al.* 2020) and numerical studies (e.g., Lucas *et al.* 2017; Fan *et al.* 2020; Kang *et al.* 2021). Grandemange *et al.* (2013) indicated that the top and bottom shear layers are more intense than those of the lateral pair, when inspecting the streamwise Reynolds stresses in the crossflow plane 1H downstream of the base. Besides, the wall-normal and spanwise components of the normal stresses are more prominent around the tip of the mean recirculation bubble. Moreover, their results indicated that the stress distribution are vertically asymmetric due to the presence of ground (Grandemange *et al.* 2013).

The 3D-PTV measurements of Booysen *et al.* (2022) uncovered that the 3D topologies of streamwise normal stresses are uniformly distributed around the shear layers, and gradually bent towards the base's centerline (an arbitrary axis extending downstream from the origin) as the streamwise distance increases. Furthermore, the positive and negative magnitudes of streamwise-spanwise shear stresses appear as two streamwise-elongated structures. These structures are located on the model's spanwise sides at about the middle height (y = 0), and slowly taper along the streamwise direction. Regarding streamwise-wall-normal stress, the associated positive and negative structures extend downstream from the top and bottom rear edges. The spatial distribution of intense Reynolds stresses indicates the regions where velocity fluctuations or flow unsteadiness occur in the flow.

2.3 Bi-stability

This subsection presents the findings of bi-stability behavior in the wake of vehicle-shaped models, which has been previously observed in investigations of wakes behind slanted-back vehicle bodies (Lawson, Garry & Faucompret, 2007) and a 3D backward-facing step with a pyramidal-shaped leading-edge (Herry, Keirsbulck & Paquet, 2011). The experimental investigation of Grandemange *et al*. (2012) confirmed the existence of the bi-stability behavior in the wake of a

flat-back Ahmed body under laminar flow conditions. Their flow visualizations revealed a pitchfork bifurcation in the spanwise direction when experimenting at four Re_H, ranging from 310 to 415. The bifurcation is characterized as a random process where the wake is biased toward either spanwise side of the wake for an indefinite duration, resulting in two possible asymmetric states at Re_H = 365. As Re_H reached 415, the wake became unsteady and remained asymmetric on the same spanwise side as its previous state (Grandemange *et al.* 2012). The subsequent investigations found that the pitchfork bifurcation persisted in the turbulent flow from Re_H of 9.2×10^4 up to 2.5×10^6 (Grandemange *et al.* 2012; Grandemange *et al.* 2013), indicating its presence is insensitive to Reynolds number. Moreover, the wake unsteadiness causes by the bi-stability behavior led to the instantaneous wake switches between two preferred spanwise locations (Grandemange *et al.* 2013).

The literature has characterized the bi-stability behavior using the barycentre of the wake deficit in the z-direction (Grandemange *et al.* 2013; Volpe *et al.* 2015; Haffner *et al.* 2020), the base pressure gradient in spanwise direction (Grandemange *et al.* 2013; Evrard *et al.* 2016; Li *et al.* 2016; Dalla Longa *et al.* 2019), and the leading mode obtained from the proper orthogonal decomposition (POD) analysis of velocity and/or base pressure measurements (Volpe *et al.* 2015; Pavia *et al.* 2018; Fan *et al.* 2020; Pavia *et al.* 2020). According to Grandemange *et al*. 2013, the barycentre of wake deficit in the z-direction, z_b, is computed by

$$z_b = \frac{\iint_A z(1 - U/U_\infty)dA}{\iint_A (1 - U/U_\infty)dA}, \tag{2.1}$$

which is the momentum deficit over the area A within the wake flow where $U/U_\infty < 1$. The barycentre of the wake deficit shares the same physical foundation as locating the center of mass of an object. Consider an arbitrary 2D object with varying density at different locations, represented as ρ_{obj}, which is a function of the horizontal and vertical coordinates (X and Y, respectively). The horizontal coordinate for the center of mass of this object, denoted as X_{cm}, can be determined by evaluating the double integral: $X_{cm} = \iint_A X(\rho_{obj})dA \,/\, \iint_A (\rho_{obj})dA$. Here, A represents the area of the arbitrary object, and dA represents infinitesimally small areas divided from the arbitrary object. When determining the center of the wake, the density term (ρ_{obj}) is replaced with the momentum deficit, defined as $(1 - U/U_\infty)$. This substitution is made because the wake region exhibits a velocity scale of $U/U_\infty < 1$, indicating a velocity deficit compared to the

freestream velocity of $U/U_\infty = 1$. By applying the same principle, the barycenter of the wake deficit provides a quantifiable measure for the center of the wake

Through the evaluation of the spanwise barycentre of the wake deficit (referred to as z_b) over time, Grandemange et al. (2013) discovered the phenomenon of switching between asymmetric states, as depicted in figure 2.5. Interestingly, this switching occurs, on average, after approximately $1000H/U_\infty$, which is approximately three orders of magnitude longer than the two sets of vortex shedding motions observed by Grandemange et al. (2013). Despite the prolonged periods of asymmetry, the time-averaged statistics are symmetrical since the two asymmetric states are equiprobable (Grandemange *et al.* 2013; Volpe *et al.* 2015). Grandemange *et al.* (2013) and Volpe *et al.* (2015) characterized the lateral bi-stability using probability density function (PDF) evaluated upon the base pressure gradients or barycentre of wake deficit in the spanwise direction. The PDFs of these parameters in the wall-normal direction yielded only one Gaussian peak around the wake center. On the contrary, the PDFs showed two Gaussian peaks, confirming that the mean wake is a superposition of two lateral asymmetric states (Grandemange *et al.* 2013; 2014). The probability density function of z_b in figure 2.5 illustrates that both asymmetric states become equally probable over a prolonged duration, despite the asymmetry during shorter periods. Perry *et al.* (2016b) and Pavia *et al.* (2020) also provided the same evidence based on the temporal coefficient of leading POD mode. This bi-stability, characterized by its random nature and extended timescales, prompted Grandemange et al. (2013) to perform spectral analysis on the measured signals obtained from off-centre locations, which revealed an approximate -2 log trend in the low-frequency range.

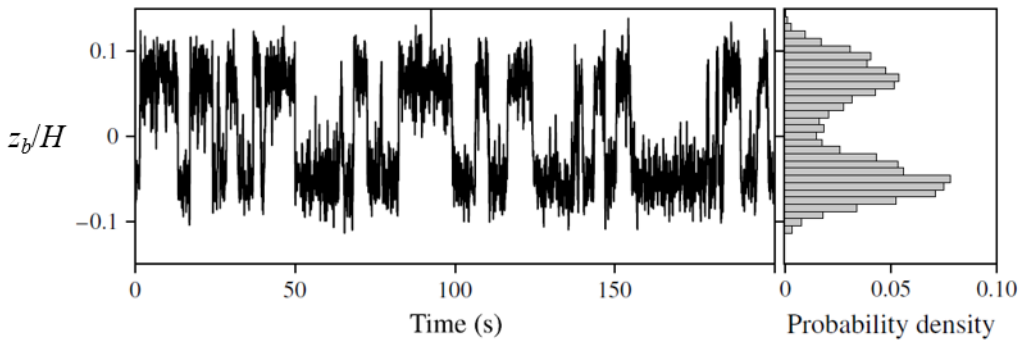

Figure 2.5 Time history of barycentre of wake deficit in the spanwise direction, adapted from Grandemange *et al.* (2013) with permission.

The statistical analyses by Grandemange *et al.* (2013) and Volpe *et al.* (2015) demonstrated that the mean topology of each asymmetric state could be extracted via conditional averaging, based on the signs of pressure gradient, streamwise velocity, and barycentre of wake deficits in the spanwise direction. Figure 2.6(*a*) demonstrated the topology of one of the asymmetric states acquired using conditional averaging, based on where the pressure gradient in spanwise direction is negative. The results indicate that the rear recirculation is inherently biased towards one spanwise side. As depicted from the 2D streamlines, the asymmetric wake consists of two unequal-sized vortices within the recirculation bubble. Volpe *et al.* (2015) shows that the spatial averaging of both states results in a left-right symmetric wake topology similar to the natural mean flow. As shown in figure 2.6(*b*), the results of Grandemange *et al.* (2013) also indicated more substantial Reynolds stresses in the shear layer, and higher overall drag due to the side force generated by these asymmetric states.

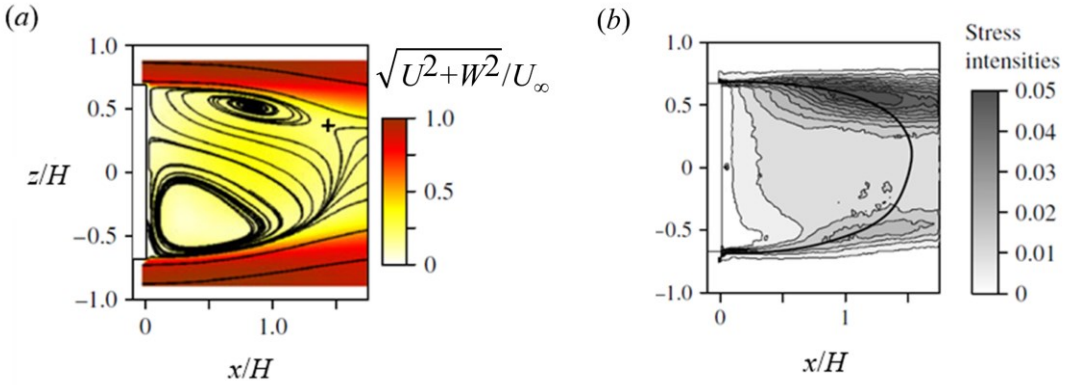

Figure 2.6 The figure illustrates (*a*) normalized velocity magnitude and streamlines, and (*b*) streamwise Reynolds stresses behind a flat-back Ahmed body, obtained from conditional averaging based on the flow fields that are biased toward the positive spanwise side. Plots are adapted from Grandemange et al. (2013) with permission.

The sensitivity of bi-stability behavior was extensively studied using different clearances, model height-to-width ratios, and yaw angles. At $Re_H \approx 365$, Grandemange *et al.* (2012) found that bifurcation only occurred at $C/H \geq 0.04$, suggesting that the bi-stability strongly depends on the ground clearance. At $Re_H = 9.2 \times 10^4$ and 1.5×10^5, Grandemange *et al.* (2013) and Cadot *et al.* (2015) respectively indicated a similar critical clearance of around $C/H \geq 0.1$. By testing different the clearance and Re_H, from 1.78×10^4 to 1.6×10^5, Cadot *et al.* (2015) found that the critical clearance is a slowly decreasing function of Reynolds number. The parametric study by Plumejeau *et al.* (2020) proposed a slightly larger threshold of $C/H \geq 0.13$, when experimenting with three

Reynolds numbers from 1.4×10^5 to 4.3×10^5. Regardless of the discrepancies, Grandemange *et al.* (2013) and Plumejeau *et al.* (2020) suggested that the absence of bi-stability is associated with the flow separation from the ground when the underbody flow is limited by the viscous effect attributed to the small clearance. Furthermore, Grandemange *et al.* (2013) stated that the bistable fluctuations would manifest in the wall-normal direction when the model height-to-width ratio is larger than one; as observed in the wake of GTS (McArthur *et al.* 2016) and simplified lorry (Dalla Longa *et al.* 2019) models. Besides, Grandemange *et al.* (2013) mentioned that the bi-stability is extremely sensitive to the alignment of the experimental setup. For instance, the misalignment in the tomo-PIV measurement of Perry *et al.* (2016a) resulted in a permanently asymmetric wake. Volpe *et al.* (2015) showed that the bi-stability completely vanishes at yaw angles larger than 1°. Meanwhile, Lahaye *et al.* (2013) and Perry *et al.* (2016b) have the same observation at a smaller angle of 0.3°.

Due to the limitation of 2D measurements, interpretations of the vortical system during the asymmetric wake were proposed in a series of experimental investigations (Evrard *et al.* 2016; Perry *et al.* 2016b; Pavia *et al.* 2018). Evrard *et al.* (2016) conducted planar PIV measurements in the symmetry planes at $Re_H = 4 \times 10^5$. They interpreted that the mean topology of each bi-stable state consists of one large horseshoe vortex, as shown in figure 2.2(*a*). Another interpretation is established by Perry *et al.* (2016b) in the investigation of Windsor body wake at 7.7×10^5. With access to an extra vertical off-symmetry PIV plane, the study suggested that the asymmetric wake can be governed by two independent vortices, as shown in figure 2.2(*b*), each associated with the bi-stability and wake oscillation dynamics. These interpretations are elucidated through the stereo-PIV measurements at $Re_H = 5.78 \times 10^5$ by Pavia *et al.* (2018). Pavia *et al.* (2018) proposed that the asymmetric states are consisted of a more complex vortical structure, as shown in figure 2.2(*c*). This structure connects all the observable vortices from previous PIV measurements with the upper streamwise vortex tail prevailing over the bottom one. More recently, this interpretation was confirmed by the tomo-PIV measurements of Pavia *et al.* (2020), which indicated a similar vortical structure in the 3D visualization of Lambda-criterion and streamwise vorticity.

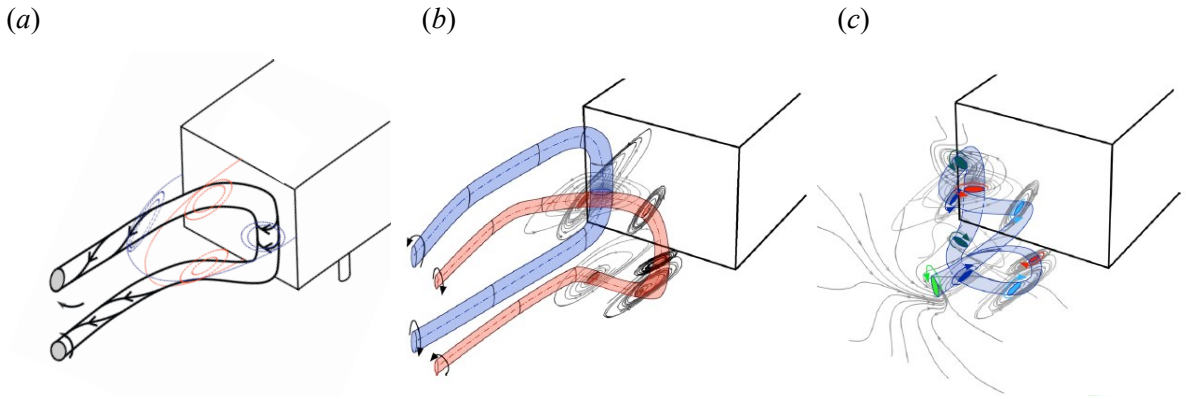

Figure 2.7 Schematic interpretations of coherent structures associated with one of the spanwise asymmetric states resulting from the bi-stability behavior. (*a*), (*b*), and (*c*) are adapted from the works of Evrard *et al*. (2016), Perry *et al*. (2016b), and Pavia *et al*. (2018), respectively, with permission.

In regards to the findings from numerical simulations, the natural switching of the bi-stable wake was not captured until the recent LES simulation by Dalla Longa *et al.* (2019), which poses the challenge of capturing the long-timescale behaviour with limited computing power. Numerical investigations have observed instantaneous coherent structures (i.e., hairpin vortex) shed from the shear layer during the switching process (Dalla Longa *et al.* 2019; Fan *et al.* 2020; Kang *et al.* 2021), as illustrated in figure 2.8 below. The shedding of hairpin vortex is argued to potentially trigger the bi-stability switching; however, this observation has not yet been reported in any experimental work.

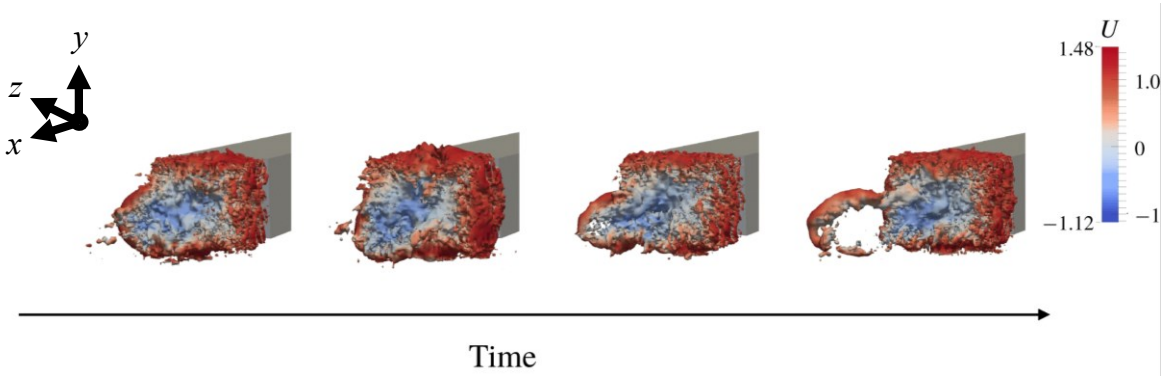

Figure 2.8 Visualizations of isosurfaces of the pressure coefficient, displayed at a threshold of 0.15 and colored by streamwise velocity at four different time instants right before the switching of the bi-stable state occurs. Plots are adapted from Dalla Longa *et al*. (2019) with permission.

Investigations also highlighted the presence of bi-stability from the leading POD mode with distinctively higher energy compared to the higher-order modes (e.g., Fan *et al.* 2020; Perry *et al.*

2016a; Podvin *et al.* 2020; Pavia *et al.* 2020; Booysen *et al.* 2022). The energy of the leading POD mode is subjected to large discrepancies across literatures, since the convergence of POD is sensitive to multiple parameters, such as the analysis domain sizes and number of velocity components accounted (Podvin *et al.* 2020). In the horizontal symmetry plane, investigations have reported the first POD mode with 15% to 35% energy (e.g., Perry *et al.* 2016a; Perry *et al.* 2016b; Fan *et al.* 2020; Podvin *et al.* 2020). For volumetric POD analysis, the first 3D POD mode captures between 12% to 30% of energy (e.g., Perry *et al.* 2016a; Pavia *et al.* 2020; Booysen *et al.* 2022). The streamwise component of the leading POD mode exhibits two identical negative and positive structures along the spanwise side of the wake, which indicates a high degree of spanwise wake asymmetry due to bi-stability. Previous works also showed the -2 log trend in the PSD of the leading POD mode coefficient (e.g., Volpe *et al.* 2015; Fan *et al.* 2020; Podvin *et al.* 2020).

2.4 Vortex shedding

Vortex shedding can occur in the wake of vehicle-shaped bodies, similar to those observed in the wakes of simple geometries, such as sphere and circular disk (Berger *et al.* 1990). The early investigations provided evidence of periodic vortex shedding motions in the Ahmed body wake. For instances, Khalighi *et al.* (2001) visualized the instantaneous vortical structures shedding downstream in the $z = 0$ plane without providing their corresponding spectral information. Later, the numerical investigation by Krajnovic & Davidson (2003) identified a peak from the power spectral of the side-force coefficient signal at $St_H = 0.22$, which has a similar frequency compared to the spanwise vortices found in a slanted-back model (Bearman 1997). Although the unsteady Reynolds-averaged Navier-Stokes simulations of Khalighi *et al.* (2012) captured vortical structures shedding downstream of the upper shear layer at $St_H = 0.17$, the spectral analysis indicates that it is only prominent along the vertical symmetry plane.

Grandemange *et al.* (2012) conducted flow visualizations at low Reynolds numbers using fluorescent dye. When the wake is unsteady at Re_H of 365 and 415, Grandemange *et al.* (2012) show that there are vortex loops shedding downstream of the Ahmed body. The unsteadiness of the flow was speculated to cause oscillations in wall-normal and spanwise directions. Based on the speculation from this flow visualization and experimental observations at $Re_H = 9.2 \times 10^4$, Grandemange *et al.* (2013) suggested that the interactions between each opposing pair of shear

layers can induce a set of vortex loops shedding downstream at different frequencies. The shedding of vortex loops resulted in the global wake to oscillate in both the wall-normal and spanwise directions, as shown in top and bottom drawing of figure 2.9(*a*), respectively. The oscillatory motions are characterized by a short timescale of ~$5H/U_\infty$. Due to the shorter distance between both horizontal rear edges, the frequency of the wall-normal oscillation is higher than the spanwise oscillation (Grandemange *et al.* 2013). Grandemange *et al.* (2013) noted that vortex shedding in the spanwise direction is one-sided, and its direction depends on the bi-stability, as shown in the bottom drawing of figure 2.9(*a*). The indication of one-sided vortex shedding is also demonstrated in the analysis of later experimental studies (e.g., Plumejeau *et al.* 2020; Haffner *et al.* 2020). Moreover, the LES simulation by Lucas *et al.* (2017) is able to capture one-sided vortex loops shedding downstream of the shear layer.

Experimental studies have identified two frequencies corresponding to each oscillating mode from the power spectral density of velocity fluctuations (Grandemange *et al.* 2013; Volpe *et al.* 2015; Fan *et al.* 2020; Plumejeau *et al.* 2020). From 1H to 3H downstream of the flat-back Ahmed body's rear face, these studies identified oscillations in the spanwise and wall-normal directions at around St_H = 0.13 and 0.18, respectively, where St_H is defined based on U_∞ and H. However, the ground proximity of the Ahmed body could result in weaker wall-normal oscillations, compared to spanwise oscillations. Plumejeau *et al.* (2020) observed greater St_H when the experimental setup was replaced with a smaller ground clearance, but the values decreased to those reported by Grandemange *et al.* (2013) as the ground clearance increased.

At a Reynolds number of approximately 4×10^5, Lucas et al. (2017) observed a spectral peak at similar St_H of approximately 0.16 when the probe was positioned at the upper and right-side shear layers. This finding is presented in figure 2.9(*b*), where the Q-criterion isosurfaces reveal the presence of vortex loops being shed downstream of the shear layer on one spanwise side, resembling those depicted by Grandemange *et al*. (2013). In a numerical investigation conducted by Dalla Longa *et al*. (2019), substantial hairpin vortices originating from the tilted toroidal vortex were documented as evidence. Furthermore, Kang *et al*. (2021) conducted a numerical study and reported similar vortical structures being shed in the shear layers, which were visualized using the Lambda-criterion.

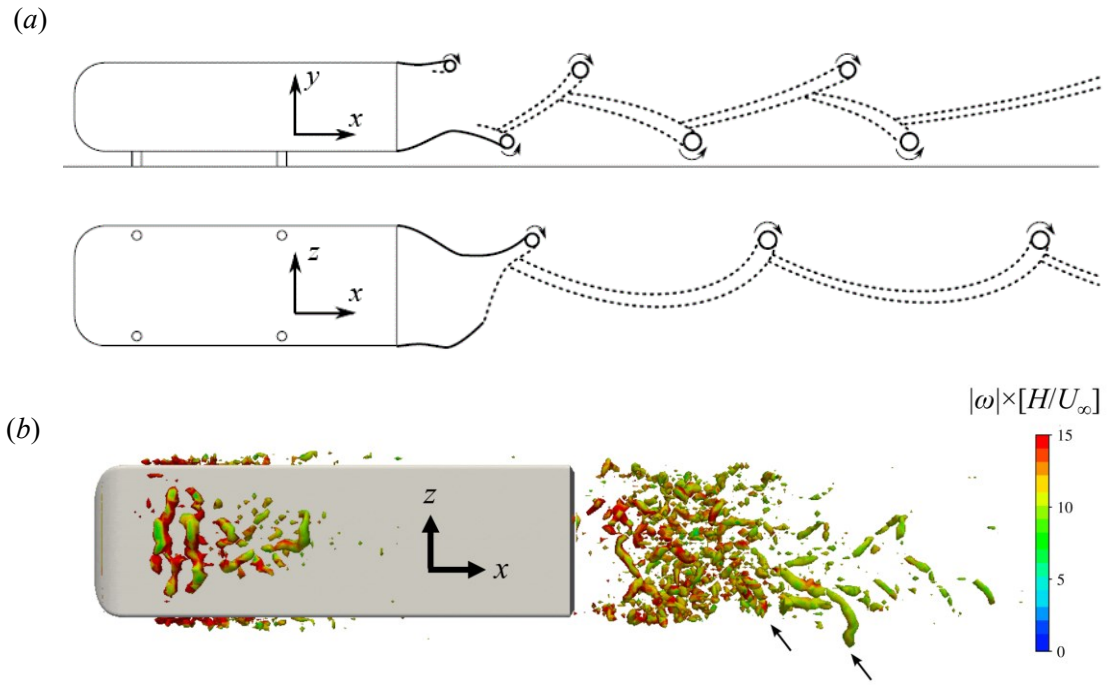

Figure 2.9 (*a*) Conceptual representations of the vortex shedding motions in the streamwise-wall-normal (*xy*) plane (top) and streamwise-spanwise (*xz*) plane (bottom), adapted from Grandemange *et al.* (2013) with permission. (*b*) Instantaneous visualization of normalized *Q*-criterion isosurface at a threshold of 22, colored by vorticity magnitudes with arrows denote the vortex loops, adapted from Lucas *et al.* (2017) with permission.

The indications of spanwise and wall-normal vortex shedding motions are shown in the leading POD modes through the power spectral densities of POD coefficients. Due to the inherent shortcoming of POD in distinguishing flow motions at different timescales, studies have shown the spanwise vortex shedding motion being captured in the first POD mode that also includes the bi-stable motion of the wake (e.g., Volpe *et al.* 2015; Pavia *et al.* 2018; Fan *et al.* 2020; Booysen *et al.* 2022). However, some studies only observed the energy of spanwise oscillating motion from higher-order POD modes (e.g., Fan *et al.* 2020; Podvin *et al.* 2020). Meanwhile, these investigations only indicated the wall-normal vortex shedding motion from the higher-order modes. Still, the spatial organizations and frequencies of these vortex shedding modes are subjected to discrepancies in the literature. For instances, the base pressure measurements by Volpe *et al.* (2015) found spectral peaks at the vortex shedding St_H of 0.13 and 0.19 from the leading bi-stability mode and a wall-normal asymmetric higher-order mode, respectively. Furthermore, Fan *et al.* (2020) identified two POD mode pairs at $St_H = 0.15$ and 0.19 with localized patterns that demonstrate phase offsets of π/2. At Re_H of 10,000, Podvin *et al.* (2020) indicated two sets of noticeably higher $St_H = 0.19$ and 0.23 from the higher-order modes. Fan *et al.* (2020)

and Podvin *et al.* (2020) noted that the vortex shedding modes pairs have similar energies. Moreover, Pavia *et al.* (2020) have reported a wall-normal asymmetric and spanwise symmetric modes, besides the first mode associated with bi-stability. By reconstructing the flow using these POD modes, they observed small vorticies break-off from the streamwise tails that are extended from the near wake toroid. They interpreted that these small-scale structures could to the vortex shedding mechanism, mentioned by Grandemange *et al.* (2013), and mentioned the necessity of time-resolved measurements to confirm this interpretation.

2.5 Bubble pumping

The origin of the bubble pumping motion goes back to the wake of circular disks and spheres where the rear stagnation point oscillates, and as a result, the separation bubble undergoes axisymmetric oscillations (Berger *et al.* 1990). At $Re_H \approx 2.0 \times 10^5$, Duell & George (1999) and Khalighi *et al.* (2001) provided evidence of bubble pumping at $St_H \approx 0.07$, based on base pressure and hotwire measurements in the vertical symmetry plane. Both studies proposed a similar explanation for the mechanism, as illustrated in figure 2.10. The mechanism is thought to be linked to the small vortices that are formed in the upper and lower shear layers at $St_H \approx 1$ (Duell & George 1999; Khalighi *et al.* 2001), similar to the shear layer instabilities found in the circular disk wake by Berger *et al.* (1990). Moreover, Duell & George (1999) also detected some lower-frequency motions from the upper shear layer at around one-half and one-fourth the frequency of the vortices form at the separation point near the rear edge. They speculated that the lower-frequency motions are formed due to vortex pairing, which increases the size of the upstream vortices as they travel to the stagnation point. The low-frequency pumping mode detected at the free-stagnation point is, therefore, linked to these vortices shed at the free stagnation point as the recirculation bubble reaches its maximum size (Duell & George 1999).

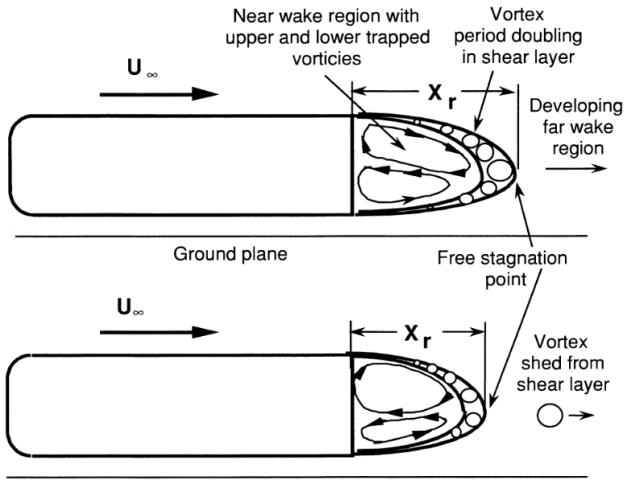

Figure 2.10 Schematic drawings of the interpretation of bubble pumping mechanism by Duell & George (1999), where top and bottom show that the separation bubble expands and contracts, respectively. Figure is extracted from Duell & George (1999) with permission.

The phenomenon of bubble pumping has been investigated further in later studies; however, the investigation of Grandemange *et al.* (2013) did not observe any indication of a low-frequency pumping mode. At $Re_H = 5.11 \times 10^5$, Volpe *et al.* (2015) observed the in-phase pressure fluctuations between the top and bottom sides of the rear face at $St_H = 0.08$. They speculated this to the bubble pumping mode causing periodic contraction and expansion of the separation bubble in the vertical plane crossing the mid-span of the wake. The base pressure measurements by Pavia *et al.* (2018) also indicated the similar coherence in the vertical plane and suggested that the pumping mode can be linked to the squeezed and stretched motions about the horizontal section of the complex vortical structure, as shown in figure 2.11. This interpretation has explained the pressure difference between the two opposing spanwise halves of the base (Pavia *et al.* 2018). Potential evidence of the pumping mode was also observed in the area-averaged spectra of base pressure fluctuations by Dalla Longa *et al.* (2019) and Haffner *et al.* (2020). At $Re_H = 2.0 \times 10^4$, Dalla Longa *et al.* (2019) reported the bubble pumping mode at $St_H \approx 0.04$ for the Ahmed body wake, which is by far the lowest frequency.

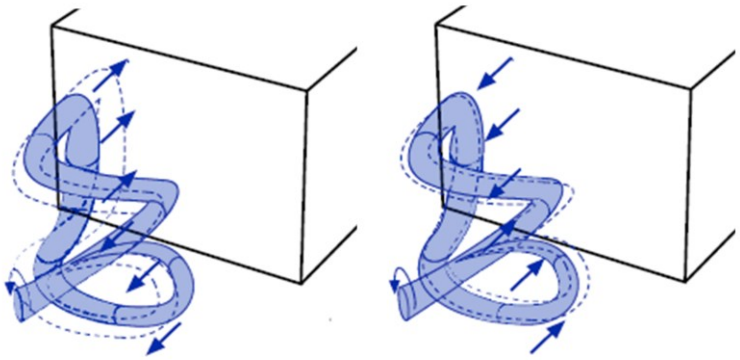

Figure 2.11 Schematic representations of the bubble pumping interpretation adapted from Pavia *et al*. (2018) with permission. The vortical structure stretching (left) and squeezing (right) in the streamwise direction.

Further evidence of the bubble pumping was also observed in the streamwise component of POD mode that exhibit spanwise symmetry. Such a spatial mode's pattern has been observed in the POD analysis, based on base pressure fluctuations (Volpe *et al.* 2015) and velocity fluctuations in streamwise-spanwise plane by (Fan *et al.* 2020). The 3D POD analysis of Pavia *et al*. (2020) and Booysen *et al*. (2022) also observed a POD mode with similar spanwise symmetry. At Reynolds number of $Re_H = 5.0 \times 10^5$, Haffner *et al.* (2020) also identified the bubble pumping mode from the PSDs of separation bubble area and strength, as well as the SPOD mode at $St_H \approx 0.07$. Their SPOD analysis also indicated two high-frequency motions at $Re_H \approx 0.5$ and 1 in both symmetry planes, which were claimed to be associated with the shear layer instabilities. Although these high-frequency motions can be associated with the conjecture of bubble pumping seen in figure 2.10, to the author's knowledge, the connection between the two motions have not been discussed yet. In general, the presence and the spatial dynamics of the bubble pumping mode requires additional investigations.

2.6 Modal decompositions

Modal decompositions are useful mathematic tools to reduce the dimensionality of data and visual them at lower dimensions. One of the modal decomposition techniques, the space-only formulation of POD, is often used in previous experimental investigations of Ahmed body and Windsor body wakes (e.g., Lahaye *et al.* 2013; Volpe *et al.* 2015; Perry *et al.* 2016a; Perry *et al.* 2016b; Pavia *et al.* 2018; Pavia *et al.* 2020; Fan *et al.* 2020; Podvin *et al.* 2020; Booysen *et al.* 2022). In this

formulation, the eigenvectors and eigenvalues of the two-point "spatial" correlation tensor result in a set of spatial modes, which temporal changes of magnitude are described by a set of coefficients. This formulation is easy to implement since it does not require time-dependent measurements, while the coefficients of the spatial modes have random time dependence (Schmid 2010; Towne, Schmidt & Colonius 2018). As a result, the spatial modes do not necessarily represent structures that are coherent in time and are often a mix of flow motions at various frequencies (Schmidt & Colonius, 2020). Such a decomposition of velocity field is not ideal for identifying turbulent structures that must have both spatial and temporal coherences. For example, Volpe *et al.* (2015) and Pavia *et al.* (2018) have indicated the amalgamation of the bi-stable motion and the spanwise oscillations – two motions with different timescales – in the first POD mode. The coupling between bi-stability and oscillatory modes is emphasized in the numerical investigations conducted by Podvin *et al.* (2020; 2021). For instance, their POD reduced-order model, comprising bi-stability and higher-order modes (i.e., vortex shedding motion), demonstrates that the switching of asymmetric states is associated with the instantaneous augmentation of the POD coefficients for the higher-order modes.

The lack of temporal coherence of POD modes can be addressed using dynamic mode decomposition (DMD), which requires time-dependent measurements. Rowley *et al.* (2009) first connected the ideology of DMD to the Koopman operator theory (Koopman 1931) that established the physical foundation of DMD. The method relies on a linear approximation of the Koopman operator, which is a linear mapping between the current and subsequent flow field (Schmid 2010). By performing the eigendecomposition on the matrix that represents the linear mapping, the DMD formulation is able to isolate individual coherent structures in the flow based on their frequencies. Furthermore, each DMD mode is linked to a single frequency as well as its growth/decay rate (Rowley *et al.* 2009; Schmid 2010; Bagheri 2013; Towne *et al.* 2018). DMD was employed in the numerical investigation of Evstafyeva *et al.* (2017) for identifying flow structures in a streamwise-spanwise plane of an Ahmed body wake at low Reynolds numbers. The method is also applied in the numerical study of Dalla Longa *et al.* (2019) for a simplified lorry model at $Re_H = 20{,}000$ with bi-stability in the wall-normal direction. Their DMD analysis in a 3D domain showed that the bubble pumping mode consists of a toroidal structure, and the vortex shedding consists of a large structure formed of shear layers merging.

An alternative technique that can address the shortcoming of space-only POD is using the space-time formulation of POD that decomposes the two-point "space-time" correlation tensor into orthogonal modes that each oscillates at a certain frequency (Lumley 1970; Picard & Delville 2000). This technique is referred to as SPOD and requires a collection of time-dependent flow realizations. SPOD has been overshadowed by the space-only formulation, since it typically requires planar or tomo-PIV hardware with a high acquisition rate. It has recently been recalled by Towne *et al.* (2018), who further elaborated the connections between SPOD, DMD, and space-only POD. Their results show that both SPOD and DMD extract dynamically significant coherent structures. In addition, SPOD modes are optimal to capture the energy present in turbulent flow as the space-only POD (Towne *et al.* 2018). To this date, only Haffner *et al.* (2020) applied SPOD to planar PIV and light intensity measurements of the flat-back Ahmed body wake. Their SPOD analysis demonstrated evidences of bubble pumping, vortex shedding, and two localized high-frequency modes at $St_H \approx 0.5$ and 1. Although computational fluid dynamics provides time-resolved realizations of the flow field, the limited computational resources have prevented to obtain long sequences that are sufficient for spectral POD.

Chapter 3. Experimental methodology

This chapter begins by providing detailed information on the measurement methodologies, which encompass the flow facilities, measurement setups, and procedures of data processing. The following subsections explain the primary analysis tools utilized in the current study, namely the POD and SPOD algorithms, along with their implementations.

The flow facility and the model's size were selected to enable time-resolved tomo-PIV within a measurement volume covering the full near-wake region. For this reason, the experiments were carried out in a water flume to benefit from two factors. First, for a desired Reynolds number, the smaller kinematic viscosity of water requires a smaller model, and therefore, a smaller measurement volume, relative to experiments carried out using air in wind tunnels. Second, the density of water allows utilizing large tracers that scatter more light. The smaller measurement volume and the larger tracer particles allowed recording tomo-PIV images with sufficient signal-to-noise ratio for a measurement volume with dimensions of $2.6H \times 1.5H \times 2.2H$ in streamwise (x), vertical (y), and spanwise (z) directions, respectively. In addition to tomo-PIV, planar PIV measurements were carried out for preliminary characterization of the flow upstream and downstream of the model. In the following sections, the flow facility, planner PIV, tomo-PIV, and the implementation of the modal decomposition are described.

3.1 Flow facility

The measurements were conducted in a free-surface water flume, as shown in figure 3.1, at the fifth-floor laboratory of Mechanical Engineering Building. The rectangular test section is located between two reservoirs, and has a length, width, and height of 5.0 m, 0.68 m, and 0.50 m, respectively. Two centrifugal pumps (DEMING 4011 4S) that operate in parallel circulate the flow

in the flume, and a required flow speed is controlled by a variable frequency drive. The upstream reservoir consists of guide vanes, a honeycomb structure and two layers of mesh to straighten the flow and generate a uniform velocity profile before the flow enters a small contraction section upstream of the test-section. To provide optical access, the bottom and side walls of the test-section are made out of glass. The water level and flow speed were set to 0.32 m and U_∞ = 0.396 m/s during all the measurements of this investigation.

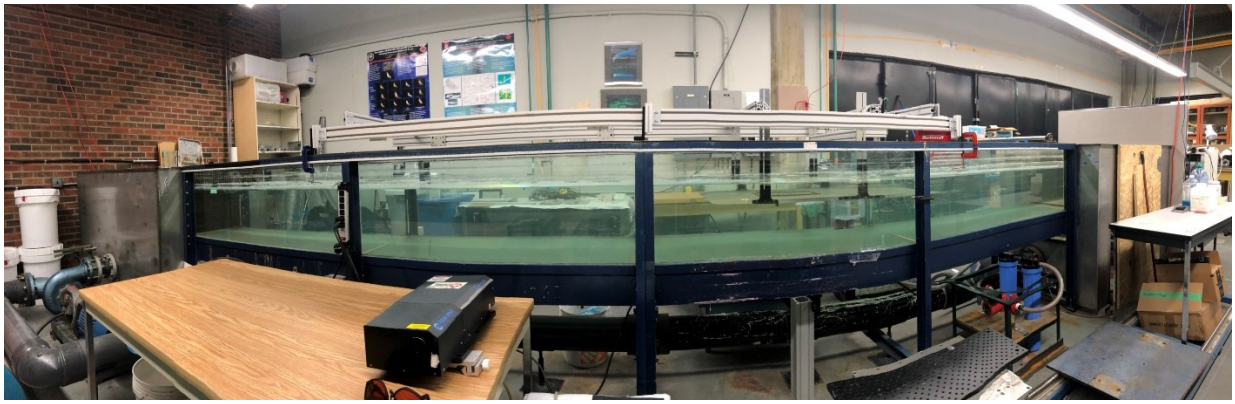

Figure 3.1 The water flume with the flat plate installed within the test section.

A schematic of the measurement setup (without the cameras and laser) is shown in figure 3.2. The flat-back Ahmed body was mounted upside-down along the spanwise center of a flat plate, featuring an optimized LE profile (Hanson, Buckley & Lavoie 2012) and a high tapered angle TE. The flat plate had a total length of 700 mm and a width of 620 mm. The Ahmed body was also placed 195 mm away from the bottom wall and 126 mm below the free surface of the water flume. The two distances minimized the interference of the wake flow with the turbulent boundary layer of the bottom flume wall and with the free-surface waves.

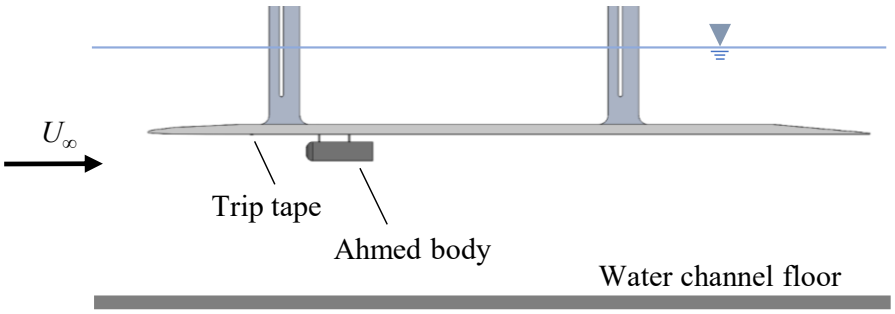

Figure 3.2 Schematics of experiment configuration viewing from the side.

The LE of Ahmed body was at a distance of l_1 = 259 mm downstream of the plate's LE, which is about 1.8 times of the original work (Ahmed *et al.* 1984). At this location, the Reynolds number based on l_1 and U_∞, is 1.0×10^5, which is smaller than the critical Reynolds number for natural laminar-to-turbulent transition (Schlichting & Gersten 2016). Preliminary planar PIV experiments were conducted without the installation of Ahmed body, as shown in figure 3.3. The two Imager ProX (LaVision GmbH) 14-bit CCD cameras are horizontally parallel to each other and the stitched field-of-view (FOV) of both cameras covered a distance from the plate's LE to the LE of the Ahmed body in the streamwise direction. The alignment of the flat plate was examined from the results of mean velocity field, which showed the flow is fully attached to the LE without separation, consistent with the original work (Ahmed *et al.* 1984). These measurements showed a boundary layer shape factor of 1.86 at l_1. To obtain a stable boundary layer, a tripping tape with a rectangular cross-section of 1 mm × 4.5 mm (wall-normal height × streamwise length) was installed at l_2 = 160 mm downstream of the plate's LE and across the full span of the plate.

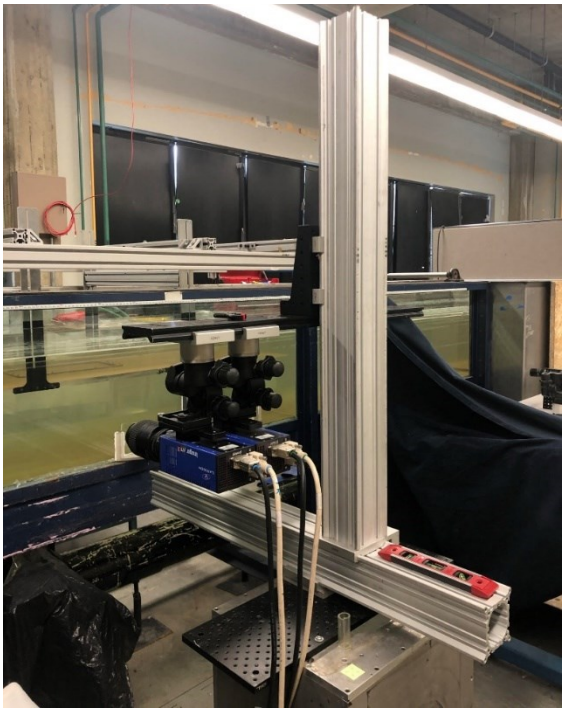

Figure 3.3 The preliminary planar PIV experiment with two cameras viewing upstream of the installation location of Ahmed body

The location of the tape (l_2) and its height (h) were selected to ensure laminar-to-turbulent transition and to allow sufficient flow development before the flow reaches the Ahmed body. The first criterion was evaluated by calculating two different Reynolds numbers described by Schlichting & Gersten (2016) and Brasow and Knox (1958). The former is calculated based on the displacement thickness at l_2, while the latter is based on h and the streamwise velocity at h. When the trip step was absent, both Reynolds numbers of $Re_1 = 443$ and $Re_h = 291$ were calculated l_2, which are relatively close to the suggested values. Next, the final confirmation was carried out by PIV measurement at l_1, after the tripping tape was installed. The measurements showed a shape factor of 1.47 (without the Ahmed body), indicating that a turbulent boundary layer was achieved. Meanwhile, the boundary layer thickness (based on 99% of U_∞) at l_2 was $\delta_{tr} = 5.7$ mm. This results in $17.5\delta_{tr}$ distance between the tripping tape and the Ahmed body, which is larger than the $15\delta_{tr}$ criterion suggested by Elsinga & Westerweel (2012). Hence, the trip step location was far enough and had a negligible three-dimensional effect around the Ahmed body. PIV measurements also showed a boundary layer thickness, $\delta_{0.99}$, of 8.6 mm, based on 99% of U_∞ at l_1 (without Ahmed body).

The Ahmed body featured a flat back (no taper at the rear face) and had a 1:9.6 scale with respect to the original model of Ahmed *et al.* (1984). The drawings of Ahmed body and flat plate are attached in Appendix A. The model was machined from acrylic using a computerized numerical control (CNC) router. The front and rear faces were painted in black to reduce reflections of the laser light during the experiments. The total length L of the body was 109.0 mm, and the height H and width W of the rear face were 30.0 mm and 40.0 mm, respectively. The Ahmed body was levitated from the floor by four M18-8 precision shoulder screws with an outer diameter of 3 mm diameter. The clearance between the model and the plate, C, was set to 11.2 mm. Grandemange *et al.* (2013) and Cadot *et al.* (2015) showed that the bi-stability is present when $C/H > 0.1$. The current clearance-to-height ratio is larger than the $C/H = 0.17$ used by Ahmed *et al.* (1984) due to the smaller $C/\delta_{0.99} = 1.3$ of the current experiments. The larger clearance allows a higher flow rate to pass through the gap between the Ahmed body and the flat plate, which prevents the formation of any wall-attached separation bubble downstream of the model.

The Reynolds number, defined as $U_\infty H/\nu$, was $Re_H = 10{,}000$, where ν is the kinematic viscosity of water. This Re_H is smaller than most previous experimental investigations ranging from 9.2×10^4 to 2.5×10^6 (e.g., Ahmed *et al.* 1984; Grandemange *et al.* 2013; Volpe *et al.* 2015; Evrard *et al.* 2016; Pavia *et al.* 2018; Pavia *et al.* 2020; Plumejeau *et al.* 2020; Haffner *et al.* 2020). Haffner *et al.* (2020) indicated that the low transition occurs at a similar Re_H of 9,000, but the justification is unclear. Regardless, the Re_H in the current study matches the Re_H of recent numerical simulations by Podvin *et al.* (2020, 2021). Podvin *et al.* (2020) observed that the flow features are similar to those reported by Evrard *et al.* (2016) experiments at higher $Re_H = 4.0 \times 10^5$.

3.2 Planar particle image velocimetry

The planar PIV is a non-intrusive measurement technique for measuring two-dimensional-two-components velocity fields. A basic PIV system consists of the following components, as illustrated by Raffel *et al.* (2018). The system consists of tracer particles seeded into the examined fluid. The light source is typically generated using a double-pulsed laser beam, which is expanded into a thin light sheet through laser optics to illuminate the measurement plane. The tracer particles are illuminated as they pass through the laser sheet. The scattered lights from these particles are recorded by the recording system, consisting of a CCD camera and imaging optics. The camera

views perpendicularly to the measurement plane with its focus plane coincides with the light sheet. To avoid capturing any out-of-plane motions for planar PIV, it is recommended is to employ a thin laser sheet that is ~1 mm thick and a sufficiently small camera's depth-of-focus. The recording system converts the scattered lights into measures of light intensities that form the final particle-image. Then, the spatial cross-correlation algorithm is applied to these images to obtain the velocity field. Here, the velocity field is computed based on the displacement vectors and time interval between two illuminations of the laser, Δt. In order to obtain velocity vectors with low uncertainties, it is important to carefully adjust Δt to acquire an appropriate particle displacement between the two cross-correlation images. A 15 pixels particle displacement is recommended at the freestream (Raffel *et al.* 2018).

The PIV measurement has two types of recording methods: double-frame and single-frame. For double-frame recording, the recordings are taken between two laser pulses with short Δt, and each image pair is separated by a longer duration. Among the entire sequence of double-frame measurements, the cross-correlation is only performed between the time-resolved image pairs. This method allows for longer measurements but the resulted velocity fields between two image pairs are not time-resolved. For single-frame recording, measurements are taken at each laser pulse. In this method, one particle image is taken at a time with a constant Δt between all images. In order to compute the time-resolved velocity fields, the Δt between the sequential pair of images also has to be time-resolved.

A planar PIV experiment was carried out to characterize the mean flow features at the upstream and downstream of the Ahmed body. The PIV system consisted of two Imager ProX (LaVision GmbH) 14-bit CCD cameras with a pixel size of 7.4 × 7.4 μm^2. Both cameras were equipped with Nikon lenses with the same focal length of f = 105 mm and an aperture setting of f/5.6. The upstream and downstream measurements were conducted simultaneously on the xy plane crossing through $z/H = 0$, as shown in figure 3.4. The first camera imaged the field-of-view (FOV) indicated as FOV1 upstream of the Ahmed body, while the second camera imaged FOV2 downstream of the model. Both cameras image using a cropped sensor (2047 × 1001 pix) at a magnification of approximately 0.1. FOV1 and FOV2 had a similar dimension of 146.4 × 71.5 mm^2 and 149.8 × 73.2 mm^2, respectively. The digital resolution of the first camera was 71.5 μm/pix, and the second camera was 73.2 μm/pix. Both field-of-fields are slightly overlapped with the leading- and trailing-

edges of the Ahmed body. A dual-cavity Nd: YAG laser (Gemini, NewWave Research) with 110 mJ/pulse was used as the illumination source. The laser beam was expanded through a combination of two cylindrical lenses and two spherical lenses with 1 mm thickness covering both FOV1 and FOV2. Two sets of 1,500 double-frame images were collected using a pulse separation of Δt = 1500 μs at 9.4 Hz.

The silver-coated spherical glass beads (SG02S40 Potters Industries) with a density of 4 g/cm^3 and diameter of 2 μm were used as the seeding particle. The corresponding particle response time $t_p = \rho_p d_p^2/18\mu$ and settling velocity $u_p = (\rho_p - \rho)\, d_p^2 g/18\mu$ were 9.8 × 10^{-7}s and 7.2 × 10^{-6} m/s, respectively. The fidelity of particles following the fluid flow was examined using two parameters, namely the Stokes number $Stk = t_p/t_f$, and Froude number $Fr = u_p/u_c$ (Bewley, Sreenivasan & Lathrop, 2008). Here, t_f is defined as the characteristic timescale, and u_c the characteristics velocity of the flow estimated based on the vortex shedding period (~7×H/U_∞) and U_∞, respectively. The Stokes number of the tracers is 1.8 × 10^{-6}, which is smaller than the recommended value of 0.1 (Samimy & Lele, 1991). The Froude number is 1.8 ×10^{-5}, several orders of magnitude smaller than unity (Bewley, Sreenivasan & Lathrop, 2008).

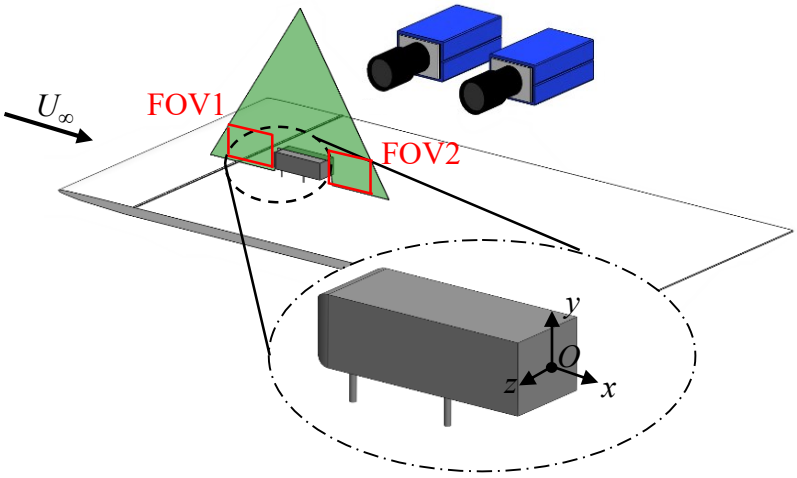

Figure 3.4 Schematics of the two cameras, tripwire, laser sheet, flat plate, and the Ahmed body for planar PIV experiment viewing upside-down. The measurement was conducted on the *xy* cross section upstream and downstream of the model: FOV1 and FOV2. The coordinate system at the Ahmed body base is shown in the enlarged-view of the model, where the origin *O* is at the base's center.

To improve the signal-to-noise ratio (SNR) of all double-frame images, the minimum intensity of all images was calculated and then subtracted from each image. The resulting images were then normalized using the average intensity of all the minimum-subtracted images. The 2D vector fields

were obtained through double-frame cross-correlation with a multi-pass algorithm in Davis 8.3 (LaVision GmbH). The final interrogation window was 32 × 32 pixels (2.2 × 2.2 mm^2). A window overlap of 75% was applied between neighboring interrogation windows. About 3% of the velocity vectors were identified as spurious and were removed based on the universal outlier detection method (Westerweel & Scarano, 2005).

3.3 Tomographic particle image velocimetry

This section first illustrates the principles of tomo-PIV, as described by Elsinga *et al.* (2006), followed by the details of tomo-PIV measurements of the Ahmed body wake. The procedures of tomo-PIV experiment can be illustrated with the 6 following components (Scarano, 2013). Firstly, an illuminated volume is generated using a laser beam and optics to illuminate the tracer particles within the measurement volume (or 3D object). Secondly, 3 to 6 cameras are employed in either linear or cross configuration to image the measurement volume at different viewing angles. Thirdly, the particle image (2D projection of the light intensity fields) should be in focus achieved by matching the cameras' focal depths with the thickness of illuminated volume. Scheimpflug adapter is typically required for a camera with a large viewing angle to mitigate the requirements of focal depth by aligning the focal plane with the measurement volume. Furthermore, target calibration is conducted in advance to map the relationship between the camera planes and measurement volume. Moreover, the particle images are used to reconstructed a volume consisting of 3D array of cubic voxel elements. This step is accomplished via tomographic reconstruction using the multiplicative algebraic reconstruction techniques (MART). The MART is an iterative algorithm to determine the spatial particle distributions, in which a voxel would only be assigned with nonzero values if a particle is detected along all cameras' line-of-sights. Finally, the three-dimension-three-components velocity fields are obtained via 3D cross-correlation between two reconstructed volumes spaced by Δt.

According to Wieneke (2008), self-calibration is an essential procedure prior to tomographic reconstruction, since the mapping of image-to-object space has to be corrected in order to reduce the triangulation error. Once the number of sub-volumes is identified, the triangulation is performed to obtain the 3D particles' positions from the particle images of all cameras. To calculate better statistics of the disparity map, a collection of particle images from all cameras is

used. Then, a 2D map would display the particles' disparities within each sub-volume, and the disparity vector field shows the highest disparity peak within each sub-volume. It is also optional to smoothen the disparity vector field depending on the situation. For accurate 3D calibration, the above procedure is recommended to repeat until the residual disparity is below 0.1 (Wieneke, 2008). Finally, the mapping functions between all cameras and the 3D object space are corrected based on the final disparity map.

According to Elsinga *et al.* (2006), excessive particle density can decrease the quality of tomographic reconstruction due to ghost particles, although it can potentially yield a higher spatial resolution. The detrimental effect can be compensated by implementing more cameras, but it is important to ensure that the cameras' line-of-sights do not overlap so particles can be identified from different angles. A high viewing angle can decrease the reconstruction quality, since the image source density can increase with the over-extended intersection of the line-of-sight. On the other hand, a small viewing angle can cause the imaged particles to elongate along the image's depth. Scarano (2013) shows that the linear camera configuration suffers from lower reconstruction quality when the system aperture is between 20^{o} to 60^{o}, and is optimal between 70^{o} to 110^{o}.

The unsteady organization and temporal evolution of the wake were characterized using tomo-PIV measurements. The tomo-PIV system consisted of four high-speed cameras (Vision Research, Phantom v611) imaging the illuminated volume as the arrangement shown in figure 3.5(*a*). The cameras feature a complementary metal–oxide–semiconductor (CMOS) sensor with 1280 × 800 pixels, each 20 × 20 μm^2. During all measurements, all cameras had a cropped sensor size of 1184 × 704. All cameras had the same digital resolution of 70.0 μm/pix and a magnification of 0.3. Each camera was equipped with Nikon lenses (f = 105 mm) and a Scheimpflug adapter to reduce the requirement of depth-of-focus and aperture setting. An aperture setting of f/22 was applied to all cameras, resulting in a DOF of approximately 66 mm. This was roughly equal to the thickness of illuminated volume, in order to mitigate out-of-focus particles. The camera viewing angles were measured with respect to the z-axis. Both upstream cameras had a small viewing angle of about 5^{o}, while the downstream cameras had a larger viewing angle of approximately 36^{o}. Two water-filled prisms were installed on the glass wall of the flume to minimize image distortions for both

downstream cameras. The aperture angle of current system is limited since the FOVs of upstream cameras can be blocked by the trailing-edge of Ahmed body as viewing angles increase.

An Nd: YLF (Dual-head DM20-527DH, Photonics Industries) laser with 20mJ per pulse was employed to illuminate the measurement volume. The laser beam passed through three cylindrical lenses to form a large elliptical cross-section that gradually expanded in the illumination direction. The expanded beam was directed perpendicular to the flat plate (in the negative y direction) from the bottom glass wall of the water flume. A relatively "top-hat" intensity profile across the cross-section is obtained by cropped the low-intensity boundaries of laser volume using knife edges. The illuminated volume had a cross section of (Δx, Δz) = (85 mm, 67 mm) at $y = -H/2$ and (81 mm × 65 mm) at $y = +H/2$ plane. The measurement volume is indicated by the red box in figure 3.5, denoted by V, which had the dimensions of 78 × 45 × ~65 mm^3 (2.6H × 1.5H × 2.1H) in x, y, and z directions, respectively.

(*a*)

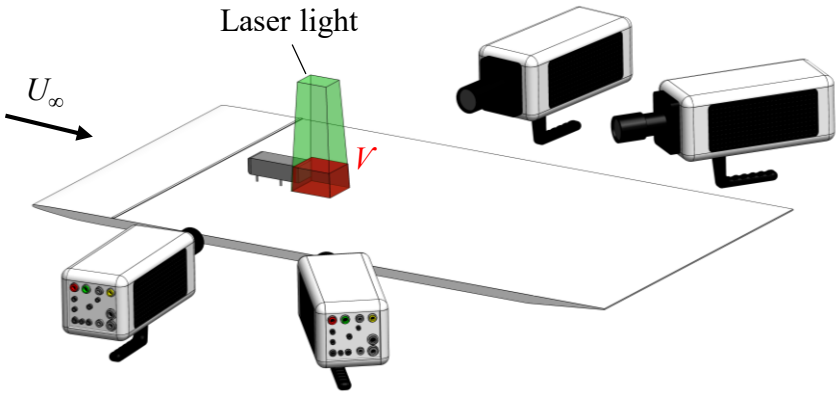

(*b*)

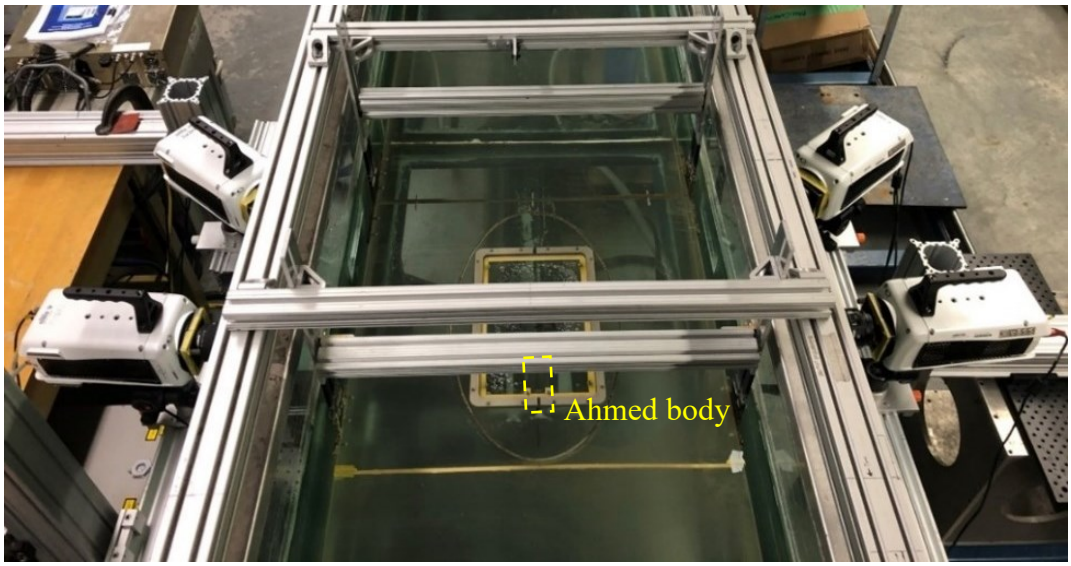

Figure 3.5(*a*) An upside-down schematic of the tomo-PIV configuration showing the four high-speed cameras, the laser light (green), and measurement volume V (red). (*b*) A photograph of the tomo-PIV measurement setup viewing from the top with four cameras, flat plate, tripwire, and Ahmed body (hidden below the flat plate).

Tomo-PIV measurements in large volumes require powerful illumination sources and tracer particles that scatter sufficient light. The current cameras aperture also leads to less capturable lights. To address the limited laser power, the spherical polystyrene spheres (TS250 Dynoseeds) with a density of around 1.05 g/cm^3 and mean diameter of 250 μm were selected as the seeding particles. In addition to the good light-scattering properties of these tracers, their small density results in a small response time of $t_p = 4 \times 10^{-3}$ s. Therefore, the estimated *Stk*, based on t_p and the vortex shedding timescale is 7.6×10^{-3}, which is smaller than the maximum recommended value of $St \sim 0.1$ (Samimy & Lele 1991). The settling velocity of the tracers is also 1.9×10^{-3} m/s, and

therefore the $Fr = 4.7 \times 10^{-3}$, which is several orders of magnitude smaller than unity (Bewley *et al.* 2008). The seeding density was inspected from the 2D image to be approximately 0.03 particles per pixel, which yields a quality factor of about 0.95 (Elsinga *et al.* 2006). The particle image diameter is between 3 to 5 pixels. The combination of these two parameters results in the maximum recommended source density of $N_s = 0.3$ (Scarano 2013).

The imaging system was calibrated using a dual-plane 3D calibration target (type 10, Lavision GmbH). A total of five calibration planes were applied by traversing the plate in the z direction with 12 mm increments. The mapping function between the cameras and measurement volume was constructed using the third-order polynomial fit in Davis 8.4 (LaVision GmbH). For volume self-calibration, the initial disparity map showed a significant image distortion. After applying the volume self-calibration, the calibration error reduced from 1.3 down to about 0.05 pixels, which is below the 0.1 pixels threshold for tomo-PIV as suggested by Wieneke (2008).

The tomo-PIV images were recorded as double-frame and time-resolved single-frame images. The double-frame images allowed for obtaining a longer duration of non-correlated data at a low acquisition frequency for faster statistical convergence. In contrast, the single-frame data at a higher acquisition frequency allowed for resolving the high-frequency dynamics of the flow. For double-frame recording, 3 datasets of 3,107 double-frame images were collected at 25 Hz using a laser pulse separation of $\Delta t = 3{,}500$ μs. The total duration of each set is 124.3 s, which is equivalent to $1641 \times H/U_\infty$ (larger than the bi-stability timescale of $\sim 1000 H/U_\infty$). For time-resolved measurements, 10 datasets of 6,212 single-frame images were collected at a recording rate of 280 Hz. Each time-resolved dataset was 22.2, which is $292 \times H/U_\infty$ (shorter than the bi-stability timescale). The time-resolved data can be used for spectral analysis of the flow between St of 0.003 to 21.2 (half the acquisition frequency). A similar maximum particle displacement of around 18 pixels was obtained for both double-frame and single-frame images. The 10 time-resolved datasets provide the stochastic ensemble required for SPOD computations.

For processing the tomo-PIV images, first, the minimum of all images was subtracted from each image. This was followed by subtracting the local minimum of image intensity within a kernel size of 5 pixels. The images were also normalized using a local average with a kernel of 100 pixels. The measurement volume was reconstructed using the fast Multiplicative Algebraic Reconstruction Technique (fast-MART) in Davis 8.4 (LaVision GmbH) following the algorithm

of Atkinson & Soria (2009). The reconstructed volume has 1116 × 645 × 931 voxels in x, y, and z directions. The vector field was obtained using the direct correlation in Davis 8.4 (LaVision GmbH). The final interrogation volume was 48 × 48 × 48 voxels (3.36 × 3.36 × 3.36 mm^3) with a 75% overlap, resulting in 93 × 54 × 78 vectors in the x, y, and z directions, respectively. The spurious vectors formed about 2% of the total number of vectors. These vectors were detected using the universal outlier detection (Westerweel & Scarano 2005) and replaced using linear interpolation. Finally, the measurement volume, V, was further cropped to 83 × 47 × 56 vectors (2.3H × 1.3H × 1.6H) to remove noisy borders. The fast-MART and direct correlation processes for each single-frame dataset (6,213 images) were carried out using a 16-core processor (AMD Ryzen 9 5950X) over a duration of 2 weeks.

3.4 Proper orthogonal decomposition

The background and method of POD are illustrated in this subsection. For brevity, the space-only formulation of POD is simply referred to as POD here, which is an algorithm for extracting spatially orthogonal organizations (or modes) from a collection of flow snapshots, acquired from measurements or numerical simulations. In this thesis, the term "flow snapshot" specifically refers to an instantaneous velocity field that is either two or three dimensional. Since the POD modes are computed based on the mean square of fluctuating velocity, their spatial patterns essentially represent the turbulent kinetic energy of the flow. Meanwhile, the POD eigenvalues represent the amounts of energy contributed by each POD mode ranked in descending order (Taira *et al.* 2017). The POD decomposes temporal or spatial correlation matrix formed by the velocity fields into a series of orthogonal POD modes that optimally describe the spatial variations of the flow. This can be illustrated through the Galerkin projection method for reconstructing low-order models. In this formulation, a collection of flow snapshots, $\boldsymbol{X}$, can be described as the sum of a finite number of time and space variables (Taira *et al.* 2017):

$$\boldsymbol{X}(x,y,z,t) = \sum a_j(t)\boldsymbol{\Phi}_j(x,y,z), \text{ for } j = 1 \text{ to } M, \tag{3.1}$$

where $\boldsymbol{\Phi}_j$ is the vector of spatial POD mode, a_j the array of POD temporal coefficient, and M the number of flow fields among $\boldsymbol{X}$. The temporal coefficient describes the temporal evolution of the POD mode. If the flow snapshots among $\boldsymbol{X}$ are time-resolved, the evolution of a_j can be treated as a signal to analyze the frequency of flow motions contained in a POD mode using Fourier

transform (Taira *et al.* 2017). However, it is important to note that a single POD mode cannot guarantee the identification of a specific flow motion at a particular frequency. As seen in equation (3.1), the time and space information of the flow are stored in two separated variables, which means the flow patterns captured by POD modes are not temporally correlated.

In regards to the algorithm, there are two ways to compute POD modes. One way is by solving the eigendecomposition of the N by N spatial correlation matrix $1/N(\boldsymbol{X}\boldsymbol{X}^T)$, where N is the spatial dimension of $\boldsymbol{X}$, and superscript T denotes the transpose operation (Lumley 1967). However, this method is generally not recommended if the spatial dimension of flow snapshot, N, is tremendously large, which is usually the case for 3D data. In the current research, the POD computations are carried out based on the "snapshot method" of Sirovich (1987) upon the three double-frame tomo-PIV datasets. The snapshot method allows for solving the POD modes from the M by M temporal correlation matrix, $1/M(\boldsymbol{X}^T\boldsymbol{X})$, where M is usually much smaller than N. The only downside of the snapshot method is that the algorithm can only resolve up to the M^{th} order of POD mode instead of N^{th} order. Nevertheless, M number of POD modes are typically more than sufficient to capture the essential features in the flow.

The POD algorithm is used in the current context to extract the most energetic flow motions in the Ahmed body wake. The velocity fields used to calculate the POD modes are obtained from double-frame measurements that are not temporally correlated. Hence, the convergence of spatial POD modes is benefit from these double-frame measurements with longer acquisition durations. To begin the POD computations, the temporal mean is subtracted from each 3D velocity field to obtain their fluctuating components. Then, each of the mean subtracted 3D velocity field is reshaped into a column-wise vector $\boldsymbol{x}_i \in \mathrm{R}^N$, and the three components (i.e., u, v, and w) are stacked vertically. Here, N is equal to the number of velocity component times the number of grid points of 3D velocity field ($3 \times 218{,}456$). The $\boldsymbol{x}_i$ vectors are then grouped together in a 2D matrix $\boldsymbol{X} = [\boldsymbol{x}_1, \boldsymbol{x}_2, \ldots, \boldsymbol{x}_M] \in \mathrm{R}^{N \times M}$, where $M = 9321$ is the total number of snapshots. Following the snapshot method, the eigendecomposition operation is performed on the temporal correlation matrix, $1/M(\boldsymbol{X}^T\boldsymbol{X})$, to obtain $\boldsymbol{U}$ and $\boldsymbol{\sigma}$. Here, $\boldsymbol{U}$ is a matrix consists of all the eigenvectors of $\boldsymbol{X}^T\boldsymbol{X}$, and $\boldsymbol{\sigma}$ is the matrix of POD eigenvalues. The energy of each POD mode, σ, is embedded along the diagonal elements of matrix $\boldsymbol{\sigma}$. Finally, the matrix of POD modes, denoted as $\boldsymbol{\Phi}$, is computed as $\boldsymbol{X}\boldsymbol{U}\boldsymbol{\sigma}^{-1/2}$, where each POD mode, $\boldsymbol{\Phi}_j$, is represented as a column-wise vector among $\boldsymbol{\Phi}$.

3.5 Spectral proper orthogonal decomposition

The SPOD is a variant of the original POD theorem (Lumley, 1967) that can address the shortcoming of POD by decomposing the flow into structures that are coherent in both space and time (Towne *et al.* 2018; Schmidt & Colonius, 2020). In this formulation, the spatial modes are eigenvectors of the cross spectra density (CSD) matrices obtained from Fourier realizations of the flow; therefore, this technique limited to flow snapshots that are temporally resolved. An in-house SPOD code was developed in MATLAB (MathWorks) based on the SPOD algorithm detailed by Towne *et al.* (2018) that is attached in Appendix C. The computations are performed using 10 time-resolved tomo-PIV datasets, with each dataset containing 6,213 flow snapshots recorded at a frequency of 280 Hz.

The steps to compute the SPOD modes and eigenvalues in the current investigation are summarized as follows. First, each dataset is divided into 3 equal segments with 50% overlap, which results in a total number of $S = 30$ segments. In fact, this procedure is equivalent to applying Welch's method to a 1D signals to achieve better statistical convergence for its spectrum, which is the foundation of SPOD method. Meanwhile, the overlap is not applied across the datasets to avoid discontinuities between the time-resolved flow fields. The data of each segment is organized into a 2D matrix, $\boldsymbol{X}_k = [\boldsymbol{x}_1, \boldsymbol{x}_2, \ldots, \boldsymbol{x}_M] \in \mathrm{R}^{N \times M}$, where k is the index of the segment varying from 1 to 30. Similar to POD, $\boldsymbol{x}_i$ is a column-wise vector of the 3D velocity field with a length of $N = 3 \times 218{,}456$. The total number of flow snapshots within each segment, M, is equal to 3106. Due to the finite onboard memory of the high-speed cameras (8 GB), acquisition of a very long dataset is not possible. Therefore, the current segmentation procedure detailed in the in-house SPOD code is slightly different from the algorithm described by Towne *et al.* (2018). Their code requires to load all data segments simultaneously. Here, the in-house code proceeds the computation one segment at a time to avoid the saturation in memory. This difference is imposed by the finite onboard memory of high-speed cameras, which prevents acquiring very long datasets.

In the current study, the following procedures are performed one segment at a time. Here, the Hamming window with optimized coefficients (Schmidt & Colonius 2020):

$$w(i) = 0.54 - 0.46 \cos\left(\frac{2\pi i}{M}\right) \text{ for } i = 1, \ldots, M, \tag{3.2}$$

is multiplied to the rows of each segment, $\boldsymbol{X}_k$, to mitigate spectral leakage. A correction factor of 2 for Hamming window is also multiplied to compensate for the effect of window on the amplitude of the spectrum, as recommended by Schmidt & Colonius (2020). Each segment is then converted from time to frequency domain via the fast Fourier transform (FFT) operation. The Fourier representation of each $\boldsymbol{X}_k$ is $\boldsymbol{Q}_k = [\boldsymbol{q}_1, \boldsymbol{q}_2, \ldots, \boldsymbol{q}_K] \in \mathbb{C}^{N\times K}$, where $\boldsymbol{q}_l$ is a column-wise vector of Fourier realizations at frequency index l. The index $l = 1$ corresponds to a frequency of 0 Hz, while the last index of l corresponds to 140 Hz ($St_H = 10.6$). The frequency resolution of the current SPOD analysis is 0.09 Hz or St_H of 0.007. Next, the column-wise vector $\boldsymbol{q}_l$ that corresponds to frequency index l from all $\boldsymbol{Q}_k$ matrices is grouped into a single matrix, $\boldsymbol{Q}_l = [\boldsymbol{q}_l^1, \boldsymbol{q}_l^2, \ldots, \boldsymbol{q}_l^S] \in \mathbb{C}^{N\times S}$.

Next, the following procedures repeat for $l = 1$ to K. The cross-spectral density (CSD) matrix, $\boldsymbol{C}_l$, for each frequency l is constructed via the snapshot method (Sirovich 1987; Schmidt & Colonius 2020), which utilizes the lower-order CSD matrix formed by $\boldsymbol{C}_l = (1/S)\boldsymbol{Q}_l^T\boldsymbol{Q}_l$. Finally, the SPOD modes and eigenvalues are computed following $\boldsymbol{C}_l\boldsymbol{\phi}_l = \boldsymbol{\phi}_l\boldsymbol{\lambda}_l$ and $\boldsymbol{\Psi}_l = \boldsymbol{Q}_l\boldsymbol{\phi}_l$. Here, $\boldsymbol{\phi}_l$ is the eigenvector of $\boldsymbol{C}_l$, and $\boldsymbol{\Psi}_l$ includes the SPOD modes at frequency index l. The matrix $\boldsymbol{\Psi}_l$ has the form of $[\Psi_l^1, \Psi_l^2, \ldots, \Psi_l^S] \in \mathbb{C}^{N\times S}$. The eigenvalue λ_l^n corresponding to SPOD mode n at wavenumber l (Ψ_l^n) is embedded in the diagonal elements of $\boldsymbol{\lambda}_l$.

Since the CSD matrix is a covariance matrix formed by Fourier realizations at l frequency, the SPOD modes are optimal to capture the variation of the flow at l frequency in both the real and imaginary states. In other words, the first SPOD mode is optimal to capture the turbulent kinetic energy, as well as the phase differences between Fourier realizations of the flow at l frequency. In fact, SPOD modes at each discrete frequency are spatially orthogonal and their significance is determined based on the energy they possess (Towne *et al*. 2018; Nekkanti & Schmidt 2021).

In the analysis of the subsequent sections, the SPOD modes are used to reconstruct a periodic reduced order model (ROM) using the leading mode at selected frequencies (Nekkanti & Schmidt 2021). The ROM model of the U component at frequency index, l, is computed according to

$$U_{\mathrm{ROM}} = \langle U\rangle/U_\infty + \mathcal{R}e(\Psi_{u,l}/U_\infty \times \mathrm{e}^{\mathrm{i}\Phi}). \tag{3.3}$$

Here, $\mathcal{R}e$ is the real part of a complex number. For any grid point of the measurement domain, $\langle U\rangle$ is the average velocity, $\Psi_{u,l}$ denotes the streamwise component of leading mode at frequency index l. The phase Φ is also defined as $2\pi f_l t$ in which f_l is the frequency (in Hz) corresponding to index

l. The duration of each ROM cycle is different as it is equal to $1/f_l$. Similar equations based on $\Psi_{v,l}$ and $\Psi_{w,l}$ are also used to reconstruct ROMs of the V and W components indicated as V_{ROM} *and* W_{ROM}, respectively. In addition, to reconstruct the ROM of the velocity fluctuations, equation 3.3 is reduced to

$$u_{\mathrm{ROM}} = \mathcal{R}e(\Psi_{u,l}/U_\infty \times \mathrm{e}^{\mathrm{i}\Phi}). \tag{3.4}$$

Similar equations are also used to reconstruct v_{ROM} and w_{ROM}.

Chapter 4. Results

This chapter demonstrates the results of the current analysis of the wake flow behind the flat-back Ahmed body. These results include the characterization of the mean flow field, the barycentre of wake deficit, as well as the findings obtained from the POD and SPOD analyses. The SPOD section is further divided into four subsections, each dedicated to elucidating specific flow motions identified from the current SPOD analysis.

4.1 Mean flow characterization

This section evaluates the mean flow characteristics using planar- and tomo-PIV measurements. Figure 4.1(*a*) shows the $\langle U \rangle / U_\infty$ contour in the *xy* plane upstream of the Ahmed body. A small region of reversed flow is observed over the flat plate right after the tripping tape at $x/H \approx -7$. The streamlines show a parallel flow that encounters the front face of the Ahmed body forming a stagnation point on the front face of the body at $y/H \sim 0$. In figure 4.1(*b*), contours of $\langle U \rangle / U_\infty$ in the *xy* plane show a recirculation zone downstream of the Ahmed body holding two counter-rotating vortices. The strongest backflow is between the two vortices and reaches a magnitude of $\sim 0.25 U_\infty$, similar to the previous investigations (Grandemange *et al.* 2013; Vople *et al.* 2015; Perry *et al.* 2016a; Fan *et al.* 2020; Pavia *et al.* 2020).

The clearance between the bottom face of the Ahmed body and the flat plate affects the underbody flow rate. If this flow rate is too small, a secondary separation bubble forms on the flat plate downstream of the Ahmed body, and the bi-stable switching of the wake disappears (Plumejeau *et al.* 2020). In figure 4.1(*b*), no indication of a secondary separation bubble is present, suggesting the underbody clearance is sufficient. The sufficient underbody clearance is also evident when the shear layer thickness is compared with the underbody clearance. The shear layer thickness is $0.2C$

in the current investigation, estimated based on the region of intense vorticity. This value is comparable with the shear layer thickness of 0.1C estimated by Grandemange *et al.* (2013) and 0.27C by Kang *et al.* (2021).

The length of the separation bubble, L_s, is also an important parameter since it is inversely proportional to the base drag of the vehicle (Grandemange *et al.* 2014). This parameter can be estimated from the location of the saddle point labelled with the letter "S" in figure 2(*b*). The estimated L_s of the current flow is 1.24H, which is smaller than L_s of 1.4H to1.5H reported at higher Re_H by Grandemange *et al.* (2013), Volpe *et al.* (2015), and Fan *et al.* (2020). The smaller L_s of the current investigation is consistent with the trend observed by Plumejeau *et al.* (2020), showing that the L_s reduced from 1.41H to 1.31H when Re_H decreased from 4.29×10^5 to 1.43×10^5. Plumejeau *et al.* (2020) attributed the smaller L_s to lower underbody flow caused by the thicker boundary layer at smaller Re_H.

The state of the boundary layer developed on the upper surface of the Ahmed body can be evaluated by characterizing the intensity of the fluctuations. At streamwise location of $x/H = 0$, the maximum standard deviation of the velocity fluctuations is approximately 0.2U_∞, indicating the turbulent state of the upper boundary layer. Similar measurements by Grandemange *et al.* (2013) indicated a maximum standard deviation of 0.35U_∞ at the upper edge of the rear face.

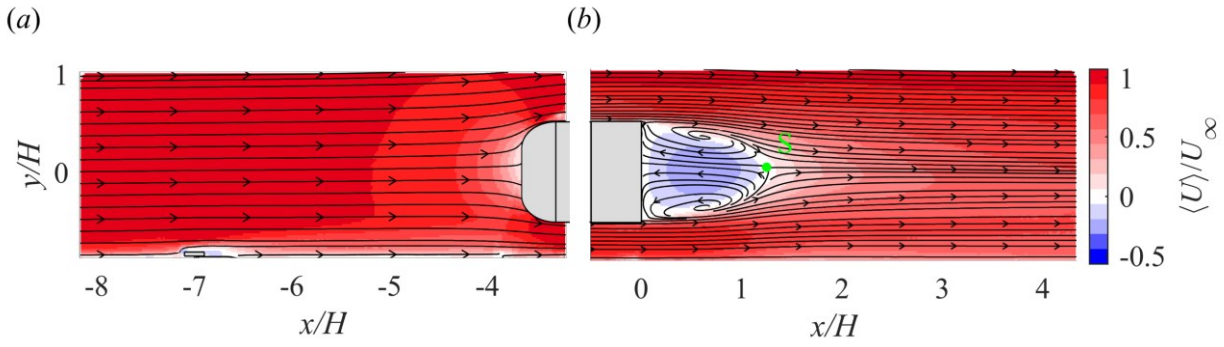

Figure 4.1 Flow streamlines and contours of normalized streamwise velocity from planar PIV at (*a*) upstream and (*b*) downstream of the Ahmed body in the $z/H = 0$ plane.

The 3D topology of the mean wake flow is characterized using the double-frame tomo-PIV measurements in figure 4.2. The 3D isosurface of zero streamwise velocity (green isosurface) in figure 4.2(*a*) shows the boundaries of the mean separation bubble, suggesting a relatively symmetric separation bubble. The main vortical structure of the mean flow is also a toroidal vortex

as seen from the purple isosurface of Q-criterion (Hunt, Wray & Moin 1998). The 2D streamlines of figure 4.2(d) in $y/H = 0$ plane reveal that two mean recirculation regions are slightly different, and the saddle point is at $z/H \sim 0.2$. The spanwise asymmetry is attributed to inadequate statistical convergence caused by the long duration of each asymmetric state of the bi-stable mode. Similar slight asymmetries in the mean velocity contours are observed in Grandemange *et al.* (2013), Volpe *et al.* (2020), and Booysen *et al.* (2022).

In figure 4.2(b), the negative and positive isosurfaces of $\langle V \rangle / U_\infty$ show different topologies for the isosurfaces of downward and upward flow. The downward flow (blue isosurface) consists of two lobes that are slightly different in size. The shape indicates that the intense downward motions are on either side of the spanwise centre at $z/H \sim \pm 0.33$. In contrast, the upward flow topology (red isosurface) shows a single triangular-shaped region with the peak of the upward at the spanwise centre. Kang *et al.* (2021) also demonstrated two off-centred downward zones and a strong central upward for an Ahmed body placed in a thick boundary layer. Despite the shape difference, the volume within the displayed isosurfaces of upward and downward is approximately similar. Figure 3(e) also shows the upward and downward motions where the streamlines curve around the end of the separation bubble at $x/H \sim 1$. In addition, the recirculation zones generate an upward zone close to the upper edge and a downward zone close to the lower edge of the rear face.

The spatial organization of the two opposing spanwise motions is shown in figure 4.2(c) and (f). There are small zones of spanwise motion near the rear face in figure 4.2(c), while the larger zones are farther downstream. The zones of spanwise motions are elongated in the y direction and slightly asymmetric with respect to the $z/H = 0$ plane. Figure 4.2(f) shows that the weaker spanwise motions form upstream of the recirculation zone, while the stronger motions form close to the end of the separation bubble at $x/H \sim 1$.

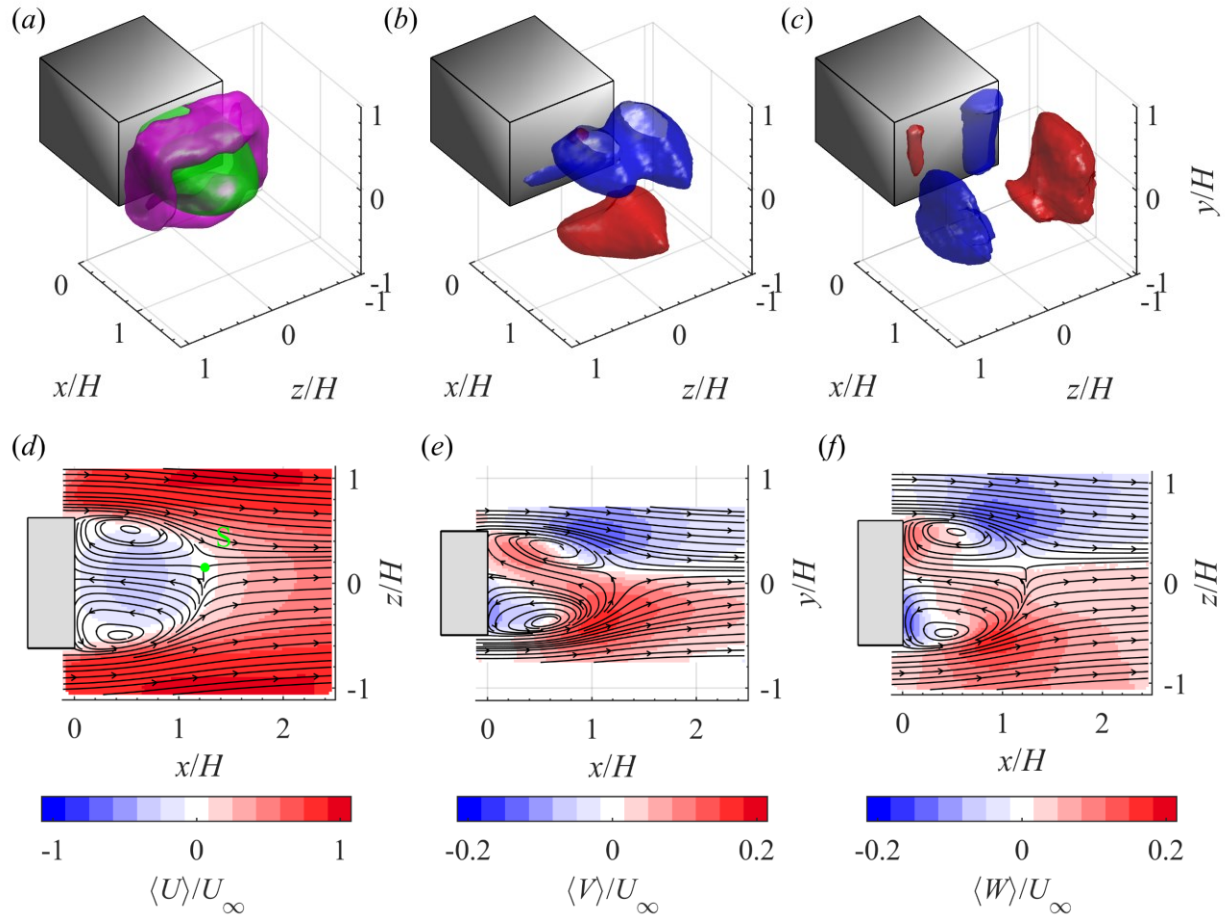

Figure 4.2 3D and 2D visualizations of the mean velocity field from tomo-PIV measurements. (*a*) Isosurface of $\langle U\rangle/U_\infty = 0$ (green) and normalized *Q*-criterion, $QH/U_\infty = 6.4$ (purple). (*b*) Isosurfaces of $\langle V\rangle/U_\infty = \pm 0.1$, and (*c*) $\langle W\rangle/U_\infty = \pm 0.1$. Red shows +0.1, and blue shows −0.1. (*d*) 2D contours of $\langle U\rangle/U_\infty$ at $y/H = 0$ plane, (*e*) contour of $\langle V\rangle/U_\infty$ at the $z/H = 0$, and (*f*) contour of $\langle W\rangle/U_\infty$ at $y/H = 0$.

4.2 Barycentre of the wake deficit

To evaluate the presence of the bi-stable mode and investigate the oscillations of the separation bubble, the barycentre of the wake deficit is analyzed. Unlike previous investigations that calculated the barycentre of the wake within 2D planes (e.g., Grandmange *et al.* 2013; Haffner *et al.* 2020), the current study computes the barycentre using 3D velocity fields obtained from tomo-PIV measurements. Using the 3D data, the spanwise barycentre location is calculated following

$$z_b = \frac{\iiint_V z(1 - U/U_\infty)dV}{\iiint_V (1 - U/U_\infty)dV}. \tag{4.1}$$

Here, the integrals are calculated within volume V within the wake flow where $U/U_\infty < 1$. A similar equation is used for calculating x_b and y_b.

Figure 4.3 displays the distributions of the joint probability density function (JPDF) for y_b and z_b. These distributions were obtained from three double-frame datasets and ten time-resolved datasets of tomo-PIV measurements in figure 4.3(*a*) and (*b*), respectively. To maintain the same orientation of the z-axis as depicted in figure 4.2, the z-axis in figure 4.3 has been flipped such that the positive z-direction is now on the left-hand side. Figure 4.3(*a*) shows two high probability z_b locations at $\pm 0.05H$ due to the spanwise bi-stability (Grandemange *et al.* 2013). These z_b/H locations are consistent with the values reported by Grandemange *et al.* (2013) and Fan *et al.* (2020). However, a slight disparity in the magnitudes of the two peaks is observed due to an insufficient statistical convergence resulting from the prolonged duration of each bi-stable state. As expected, the wake only demonstrates one high probability location in the y direction at $y_b/H = -0.03$, indicating no bi-stable motion in the vertical direction. For time-resolved data with shorter overall duration, the asymmetry is worsened in figure 4.3(*b*) showing a stronger peak at $z_b = +0.05H$ relative to the peak at $z_b = -0.05H$. Upon inspecting the time-series datasets, it is evident that out of the 10 datasets, z_b maintained a positive value in 8 datasets, was negative in one dataset, and switched between positive and negative in the remaining dataset. In terms of duration, z_b was positive in 88% of the measurement time, and negative in 12% of the time for the time-resolved data. The asymmetry can be avoided by collecting additional datasets but the prolonged tomo-PIV data processing prohibited us from collecting additional datasets. However, earlier investigations have revealed that the flow topology of both asymmetric states is comparable, and thus, there is no necessity to equally capture both states (Volpe *et al.* 2015).

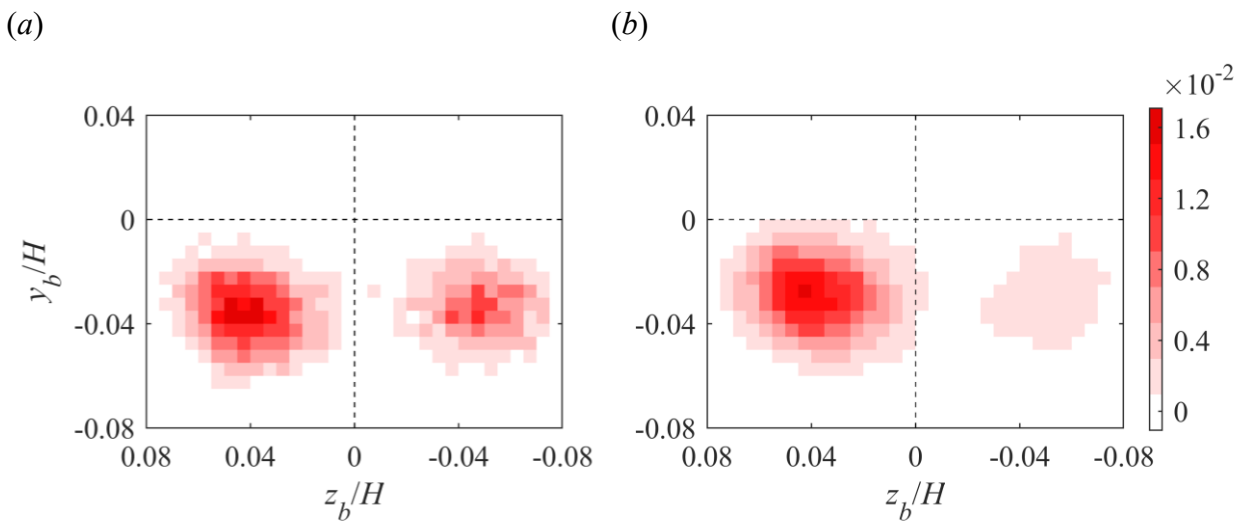

Figure 4.3 JPDF of the barycentre of wake deficits for (*a*) 3 double-frame and (*b*) 10 time-resolved tomo-PIV datasets.

Figure 4.4(*a*) displays the pre-multiplied power spectral density (PSD) of normalized fluctuations of the barycentre locations (i.e., x_b'/H, y_b'/H, and z_b'/H). These spectra depict both the frequency and magnitude of fluctuations in the separation bubble's position. For calculating the PSD, the time-series of barycentre location from each time-resolved tomo-PIV dataset is divided into 3 segments with 50% overlap and then weighted by a hamming window. Therefore, in total 30 segments, each $73H/U_\infty$ long, are used for calculating the PSDs.

At the low Strouhal number (St_H) end of the spectrum, the pre-multiplied power spectral density (PSD) of z_b' exhibits higher energy levels than that of x_b' and y_b', possibly due to spanwise bi-stability. The PSD shows two regions of high energy: the first is between St_H values of 0.03 to 0.09, which is similar to the St_H range reported previously for bubble pumping motion (Duell & George 1999; Khalighi *et al.* 2001; Volpe *et al.* 2015; Dalla Longa *et al.* 2020). However, additional investigation is required to determine if the z_b' fluctuations at this range are due to the bubble pumping motion. The pre-multiplied PSD of x_b' also displays low-frequency fluctuations between St_H = 0.05 to 0.1, but they are less significant than those observed for z_b'. The second region of high energy for z_b' is between St_H values of 0.11 to 0.18 and is attributed to the barycentre oscillations generated by vortex shedding motion, which is proposed based on its similarity to the St_H value reported for spanwise vortex shedding (Grandemange *et al.* 2013). Similar energetic motions are also observed in the pre-multiplied PSD of x_b' and y_b', with narrower and stronger peaks. The peak of y_b' occurs at St_H = 0.16, which is consistent with vertical vortex shedding

(Grandemange *et al.* 2013). Finally, a third small peak at St_H of 1.15 is visible in the x_b' fluctuations spectrum.

Figure 4.4(*b*) presents the pre-multiplied power spectral density (PSD) of the volume fluctuations in the separation bubble. The separation volume, Π, is identified where the velocity $U < 0$, and its fluctuations are denoted as Π'. The spectrum exhibits a low St_H zone at $St_H = 0.04$ to 0.1, which is energetically more significant than the low St_H zone observed for z_b' in figure 4.4(*a*). Haffner *et al.* (2020) investigated the pre-multiplied PSD of the recirculation size based on the streamwise-spanwise cross-sectional area obtained from 2D-PIV measurements. They found a narrow peak at $St_H = 0.06$, which they attributed to the bubble pumping mode. The narrower peak in Haffner *et al.* (2020) could be due to the use of 2D area instead of the 3D volume used in figure 4.4(*b*). However, further investigation of the corresponding flow motions is necessary to confirm if the low St_H range observed in figure 4.4(*b*) is consistent with the bubble pumping motion. The mid-frequency peak at St_H of 0.15 to 0.19 is in agreement with the vortex shedding process, which varies the volume of the separation bubble through vortex roll-up. Additionally, the third peak at $St_H = 1.15$ is more pronounced than the peak observed for x_b' in figure 4.4(*a*). This high St_H motion with smaller energy is attributed to shear layer instabilities mentioned in studies by Duell and George (1999), Khalighi *et al.* (2001), and Haffner *et al.* (2020).

To investigate the correlation between the fluctuations in barycentre location and the separation volume, the coherence function between each coordinate of the barycentre fluctuations (x_b', y_b', z_b') and Π' is shown in figure 4.4(*c*). The analysis reveals that at the vortex shedding St_H of 0.17, the fluctuations in Π' correlated with the fluctuations of all three coordinate locations x_b', y_b' and z_b'. Interestingly, the low St_H fluctuations of Π' only correlate with the fluctuations in x_b', whereas it shows a smaller correlation with y_b' and z_b'. At the higher St_H of 1.15, the fluctuations in Π' also only correlated with x_b'.

The results indicate that the fluctuations of Π' at $St_H = 0.04$ to 0.1 are a result of low energy oscillations of the barycentre in the x-direction, consistent with the expected dynamics of the bubble pumping motion. However, the fluctuations of Π' at the vortex shedding St_H of 0.15 to 0.19 occur along with the barycentre oscillations in all three coordinate directions. Notably, the shear layer instabilities at $St_H = 1.15$ only result in barycentre oscillations in the x-directions, leading to fluctuations of Π'. It's important to note that although the spectral analysis of figure 4.4 allows us

to compare the St_H of these motions with those reported in the literature, it only allows us to speculate about the mechanism behind them. In section 4.4, we will demonstrate the dynamics of these motions at each St_H in detail using the SPOD technique.

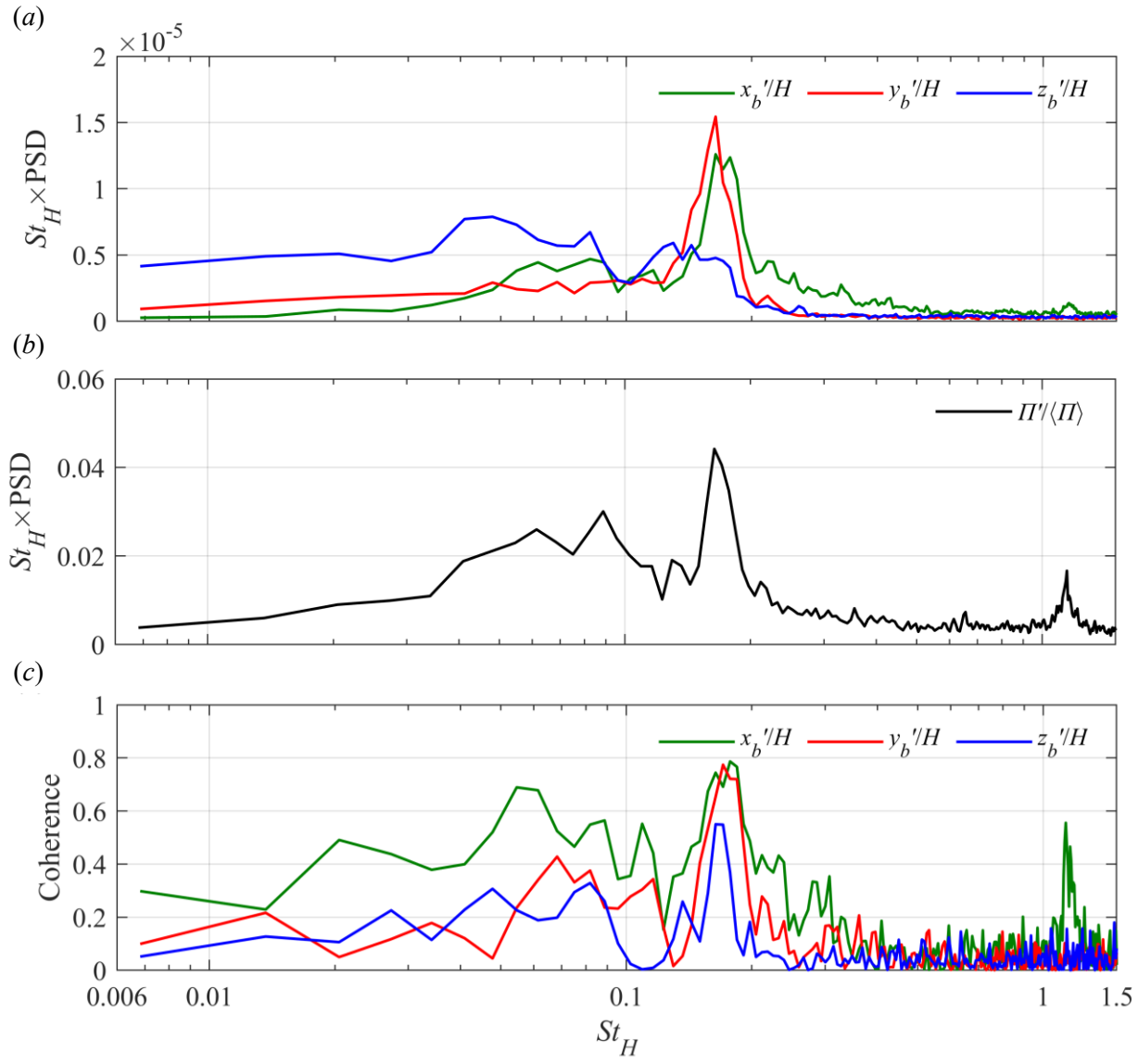

Figure 4.4 (*a*) The pre-multiplied PSD of the normalized fluctuations in barycentre location (x_b'/H, y_b'/H, z_b'/H), (*b*) the normalized fluctuations in backflow volume, $\Pi'/\langle\Pi\rangle$. The coherence function computed between (x_b'/H, y_b'/H, z_b'/H) and $\Pi'/\langle\Pi\rangle$.

4.3 Proper orthogonal decomposition

Several studies have used the Proper Orthogonal Decomposition (POD) technique to model and characterize wake dynamics. For instance, Volpe *et al.* (2015) and Pavia *et al.* (2018) employed POD to analyze pressure fluctuations at the rear-face. Pavia *et al.* (2018) also performed POD of stereoscopic PIV measurements at two crossflow planes. Perry *et al.* (2016a), Pavia *et al.* (2020), and Booysen *et al.* (2022) extended the POD analysis to 3D flow measurements. Fan *et al.* (2020) compared the POD analysis of planar PIV measurements with the POD of planar data from a numerical simulation. Podvin *et al.* (2020; 2021) applied POD to a large 3D domain obtained from direct numerical simulations (DNS). To identify similarities and highlight limitations of the POD analysis, the present study compares its results with those of previous investigations.

Figure 4.5(*a*) shows the energy distribution of the ten leading proper orthogonal decomposition (POD) modes. The first mode in the current study contains 9.1% of the total turbulent kinetic energy, which is smaller than the energy reported in previous studies using 3D measurements. For example, the first mode contained 15% of the turbulent kinetic energy in Perry *et al.* (2016a), 21% in Pavia *et al.* (2020), and 33% in Booysen *et al.* (2022). This discrepancy is likely due to several factors, including the lower Reynolds number of the current experiment and differences in the duration, domain size, and spatial resolution of the measurements. Nevertheless, the energy of the first mode in the current experiment is close to the 8% energy reported for the lead mode by Podvin *et al.* (2020) at a similar Reynolds number of $Re_H = 10{,}000$. Figure 4.5(*b*) shows that the remaining POD modes have significantly smaller energy relative to the first mode. Specifically, the second mode contains about 1.5% of the total energy, and the higher-order modes contain an even smaller percentage of the total energy. The large energy difference between the first POD mode and the remaining modes is consistent with previous POD investigations.

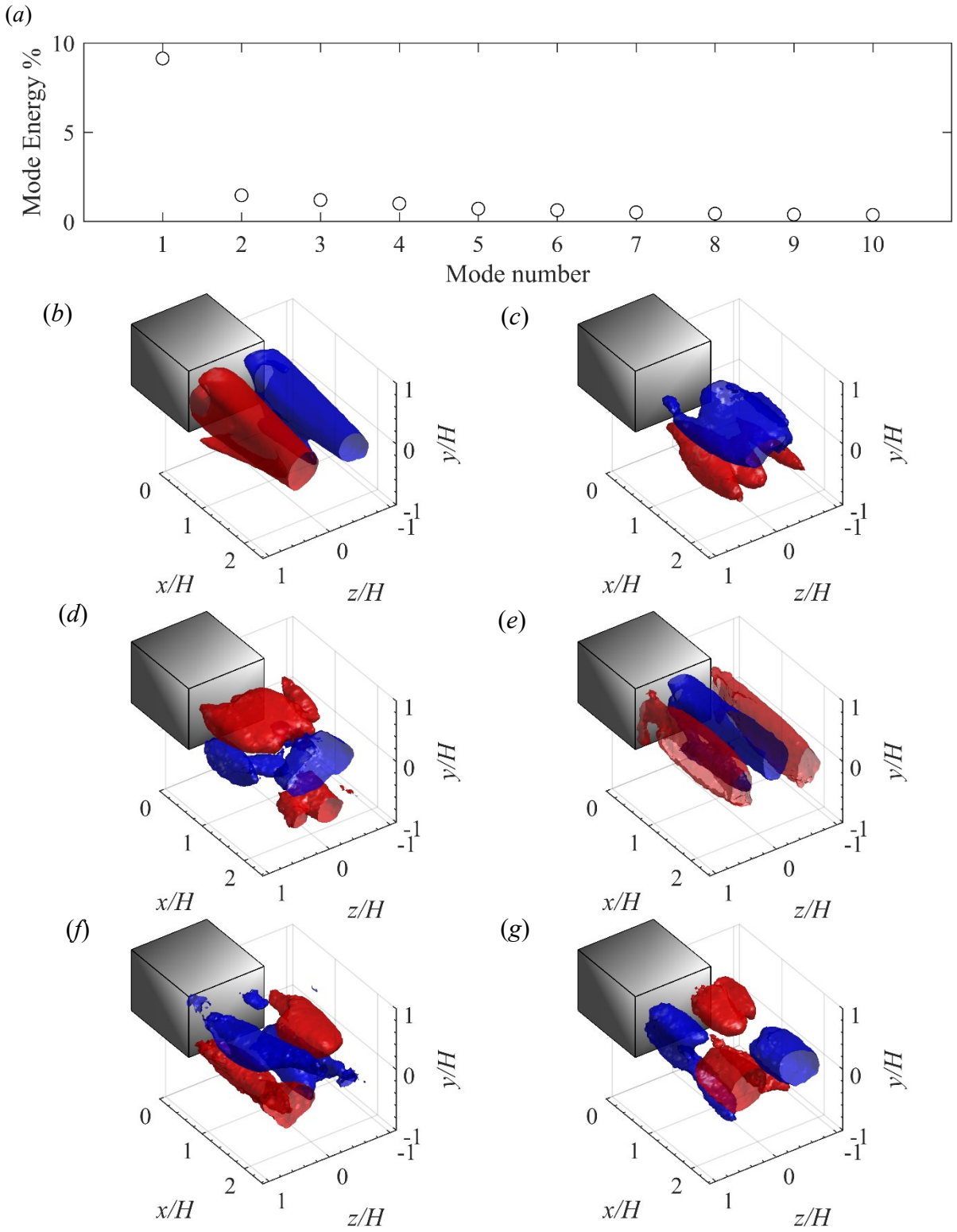

Figure 4.5 (*a*) Energy of 10 leading POD modes. (*b-g*) The spatial structures of the *u*-component for the six leading POD modes. The red and blue iso-surfaces show similar magnitudes of the streamwise component but with opposite signs.

The u-component of the first POD mode in figure 4.5(b) exhibits two streamwise-elongated structures with opposite signs, resulting in a strong antisymmetry of the wake with respect to the vertical midspan plane of $z = 0$. This mode is known as the spanwise symmetry-breaking mode (Pavia *et al.* 2018). Similar modes have been observed in 3D POD analyses by Pavia *et al.* (2020), Podvin *et al.* (2020), and Booysen *et al.* (2022). A spanwise antisymmetry has also been observed in the first POD mode of base pressure in Volpe *et al.* (2015) and crossflow PIV fields in Pavia *et al.* (2018). While Pavia *et al.* (2020) and Podvin *et al.* (2020) attributed the first POD mode to the bi-stability motion, other investigations, including Volpe *et al.* (2015), Pavia *et al.* (2018), and Booysen *et al.* (2022), associated the first POD mode with both bi-stability and spanwise vortex shedding, based on spectral analyses of the mode coefficient.

In figure 6(c), the second POD mode reveals two large structures in the upper and lower halves of the wake. These two structures are vertically antisymmetric about the mid-height plane ($y = 0$). A similar vertical antisymmetry is observed in mode 3 of Pavia *et al.* (2020). In figure 4.5(d), the third mode shows two pairs of structures at $x/H \sim 1$ and 2, which are also vertical antisymmetric about the mid-height plane ($y = 0$) and exhibit strong streamwise periodicity. Similar modes with vertical antisymmetry and streamwise periodicity are seen in Fan *et al.* (2020) and Podvin *et al.* (2020). These features are consistent with the spatial characteristics of a vertical vortex shedding process. Indeed, the coefficients of modes 2 and 3 oscillate with a constant phase offset of $\pi/2$, generating periodic oscillations along the streamwise direction.

The second POD mode in figure 4.5(c) consists of two large structures at the upper and lower halves of the wake. The two structures are antisymmetric with respect to the horizontal mid-height plane ($y = 0$). The vertical antisymmetry of this mode resembles the 3D structures shown in mode 3 of Pavia *et al.* (2020). The third mode in figure 4.5(d) shows two pairs of structures at $x/H \sim 1$ and 2 that are also antisymmetric with respect to the horizontal mid-height plane ($y = 0$). In addition, this mode demonstrates a strong streamwise periodicity. Similar modes with vertical antisymmetry and streamwise periodicity are seen in Fan *et al.* (2020) and Podvin *et al.* (2020). These features are consistent with the spatial characteristics of a vertical vortex shedding process. Upon examining the coefficients of modes 2 and 3, it became apparent that these two modes undergo oscillations with a consistent phase shift of $\pi/2$, which results in periodic oscillations in the streamwise direction.

Figure 4.5(*e*) displays the fourth POD mode, which exhibits three large streamwise elongated structures. Two structures with similar signs are observed at the spanwise sides, while a structure with the opposite sign is located along the mid-span of the wake. The middle structure also splits into upper and lower segments, which are slightly visible behind the semi-transparent red isosurface. This mode exhibits both spanwise and vertical symmetry, as it is symmetric with respect to both the vertical mid-span plane and the horizontal mid-height plane. Previous studies have reported similar symmetry-preserving modes in the POD analysis of base pressure (Volpe *et al.* 2015; Pavia *et al.* 2018), planar PIV (Pavia *et al.* 2018; Fan *et al.* 2020), tomo-PIV (Pavia *et al.* 2020), and 3D-PTV measurements (Booysen *et al.* 2022). Modulating this spatial pattern results in elongation and shortening of the separation bubble in the streamwise direction, which describes the bubble pumping motion.

In figure 4.5(*f*), the fifth POD mode exhibits streamwise structures with alternating signs along the four corners of the base. This mode displays spanwise and vertical antisymmetry, consistent with both spanwise and vertical vortex shedding. Similarly, in figure 4.5(*g*), mode 6 demonstrates comparable antisymmetry to mode 5, while also exhibiting streamwise periodicity. Analysis of the coefficients of modes 5 and 6 shows that they oscillate with a $\pi/2$ offset. Therefore, this pair of spatial modes can contribute to the vortex shedding process in both spanwise and vertical directions.

Figure 4.5 displays spatial modes that can be linked to known wake motions. However, the significance of most modes, except for mode 1, is unclear due to their low energy. Furthermore, as noted in the Chapter 2, not every POD mode necessarily corresponds to a coherent structure, meaning there may not be a direct one-to-one relationship between modes and coherence structures. For instance, modes 2 and 3 capture vertical vortex shedding, while modes 5 and 6 capture both vertical and spanwise shedding. As a result, a more rigorous analysis utilizing SPOD is necessary to identify the coherence structure.

4.4 Spectral proper orthogonal decomposition

Figure 4.6 displays the spectrum of SPOD eigenvalues after multiplying by St_H for the first 10 SPOD modes. A significant energy gap is observed between the first and higher-order modes, which signifies the importance of the leading SPOD mode (Schmidt and Colonius 2020). Thus, the subsequent subsections focus on investigating the first SPOD mode that represents the largest amount of turbulent kinetic energy. The spectrum shown in figure 4.6 is divided into five distinct zones, taking into account the spatiotemporal characteristics of the flow motions, which will be elaborated on in the subsequent subsections. Table 1 summarizes the flow motions of these zones, their corresponding St_H range, and their energy percentage. The latter is calculated with respect to the total energy of the first SPOD mode within $0.007 \leq St_H \leq 10.60$ range.

Zone A corresponds to the bi-stable behavior observed at $St_H < 0.014$. This motion has a long timescale, which manifests in the low St_H range of the spectrum. According to table 1, this zone forms 10.9% of the energy. However, due to the limited number of spanwise switching of the wake barycentre captured in the 10 time-resolved tomo-PIV datasets, the energy of the bi-stability is underestimated. Zone B describes a new type of motion, introduced here as the swirling motions of the wake, in the range of $0.014 \leq St_H < 0.123$. Although no major peak is present within this zone, these motions form 17.6% of the energy. Zone C captures vortex-shedding motions in the range of $0.123 \leq St_H < 0.212$. This zone forms 26.0% of the energy and a peak at $St_H = 0.164$. Zone D forms 20.8% of the energy and represents small-scale structures with no apparent spatiotemporal dynamics within $0.212 \leq St_H < 1.024$. In addition, the small energy gap between the first and higher-order modes further demonstrates the complexity of flow motions contained in Zone D. Finally, zone E features a peak at $St_H = 1.146$ and is associated with shear layer instability with a small energy contribution of 2.7%. For $St_H \geq 1.228$, no peak can be identified from the pre-multiplied spectrum and the energy gap between the first and higher-order SPOD modes is notably small. The following subsections examine the spatiotemporal characteristics of the first SPOD mode within all the zones, except for zone D, which lacks large-scale structures.

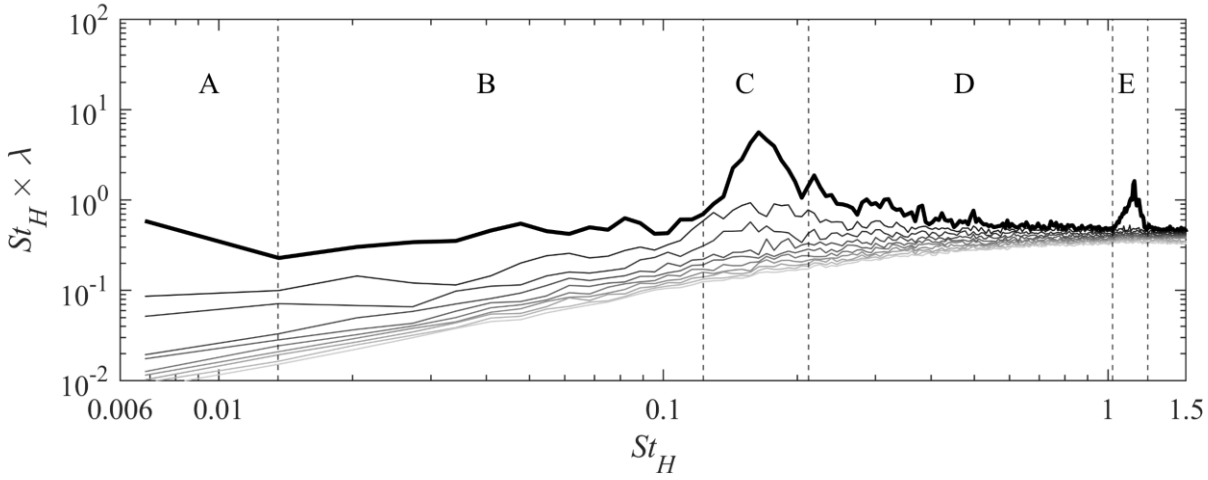

Figure 4.6 Pre-multiplied spectra of eigenvalues for the first 10 SPOD modes. The thick line shows the spectrum of the first SPOD mode, and thin grey lines indicate the higher-order modes. The frequency domain is divided into 5 zones as described in table 1.

Zone	Flow motion	St_H	Energy (%)
A	Bi-stability	< 0.014	10.9
B	Swirling motions	$0.014 \leq St_H < 0.123$	17.6
C	Vortex shedding	$0.123 \leq St_H < 0.212$	26.0
D	Small-scale structures	$0.212 \leq St_H < 1.024$	20.8
E	Shear layer instability	$1.024 \leq St_H < 1.228$	2.7

Table 1. The flow motion and St_H range of zones specified in figure 4.6.

4.4.1 Bi-stability

Figure 4.7 depicts the spatial organization of the SPOD mode at $St_H = 0.007$ in zone A. This SPOD mode features two antisymmetric structures that extend the entire streamwise length of the domain, with their axes positioned slightly above the mid-height plant at $y/H \sim 0.2$. In figure 4.7(*a*) and (*c*), smaller and weaker structures are also visible closer to the wall at $y/H \sim -0.4$. The observed symmetry-breaking pattern provides strong evidence of a spanwise asymmetry in the wake that undergoes switching after long time periods. The x-component of the reduced-order model (u_{ROM})

generated using this SPOD at $St_H = 0.007$ reveals that the two structures switch signs at phase $\Phi = \pi$ and then revert back to their initial sign at $\Phi = 2\pi$.

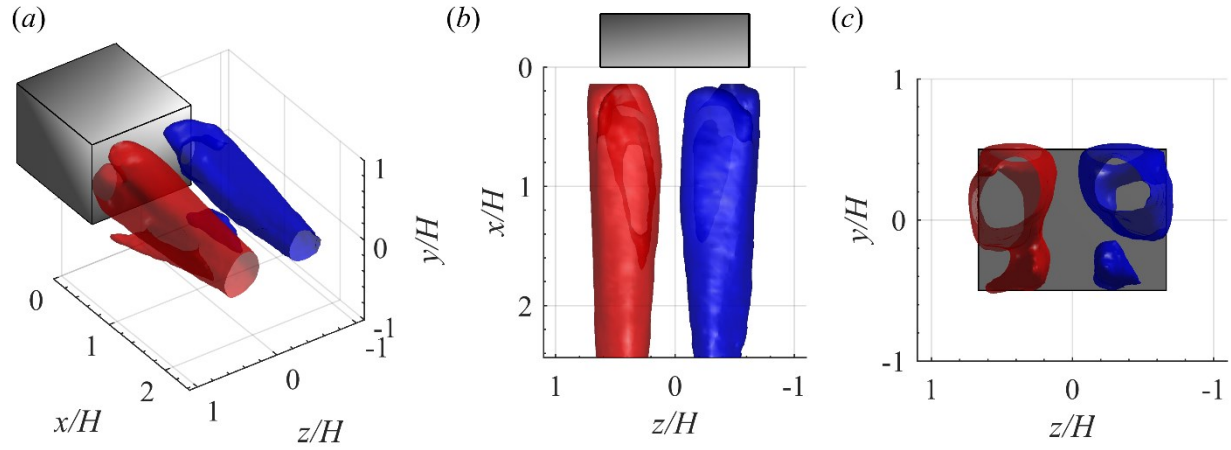

Figure 4.7 Spatial organization of the first SPOD mode at $St_H = 0.007$ in (*a*) isometric view, (*b*) top view, and (*c*) back view. The red and blue isosurfaces show $\Psi_{u,l}/U_\infty = \pm 0.25$ for frequency index $l = 2$.

The barycentre position during the full cycle of the ROM generated using the SPOD mode at $St_H = 0.007$ is shown in figure 4.8. The variation of the barycentre in the *yz* plane is presented in figure 4.8(*a*), and the variation in the *xy* plane is shown in Figure 4.8(*b*). For consistency with figure 4.2, the *z*-axes of figure 4.8 has been flipped, with positive *z* on the left side. The phase of the ROM, when z_b is at the most negative location, zero, and the most positive location, is indicated with $\Phi_1 = \pi$, $\Phi_2 = \pi/2$, and $\Phi_3 = 0.1\pi$, as seen in figure 4.8(*a*). Although the trace of the barycentre forms a closed loop, it appears as a line because it retraces its own path. Therefore, the trajectory follows a line that slightly varies along $y_b/H \sim -0.03$, consistent with the single most probable y_b/H position observed in figure 4.3. In contrast, z_b/H varies over a large range from $z_b/H = -0.11$ and 0.16. This variation is larger than the range observed in JPDFs of z_b/H in figure 4.3. The discrepancy suggests that SPOD modes at other frequencies reduce the range of motion and the asymmetry caused by the first SPOD mode at $St_H = 0.007$. Moreover, figure 4.8(*b*) demonstrates that the variation of the barycentre in the *xy* plane is negligible. Therefore, the SPOD mode at $St_H = 0.007$ mainly causes the wake to fluctuate in the *z*-direction, which is consistent with the definition of the bi-stable motion.

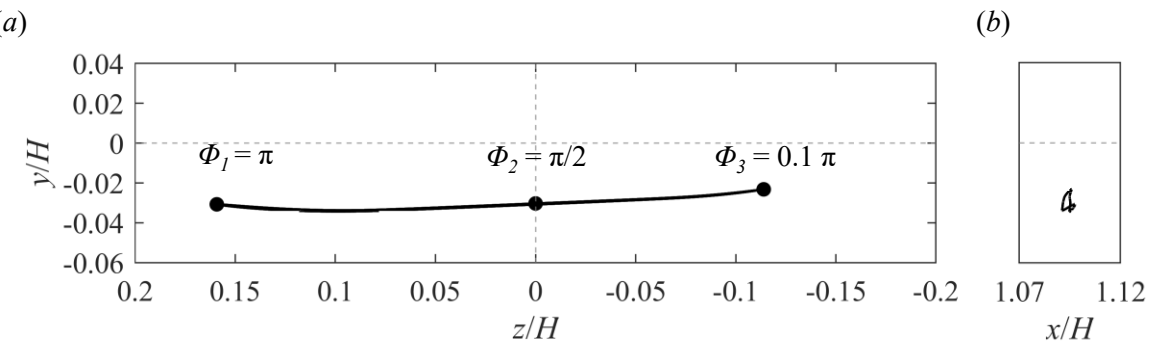

Figure 4.8 The variations of the wake barycentre based on ROM obtained using the SPOD mode at $St_H = 0.007$. (*a*) The trace of y_b/H versus z_b/H, and (*b*) y_b/H versus x_b/H.

Figure 4.9 provides a visualization of the wake topology of the SPOD mode at $St_H = 0.007$ for Φ_1, Φ_2, and Φ_3 phases. The vortical structures and separation bubble are shown in figure 4.9(*a-c*), and *yz* cross-sections that display the streamlines and mode values are seen in figure 4.9(*d-f*). To better understand the direction of rotation for streamwise vortices, a modified parameter called Q' was used in conjunction with the Q-criterion. Specifically, Q' was defined as $\omega_x/|\omega_x| \times [QH^2/U_\infty^2]$, where ω_x is streamwise vorticity.

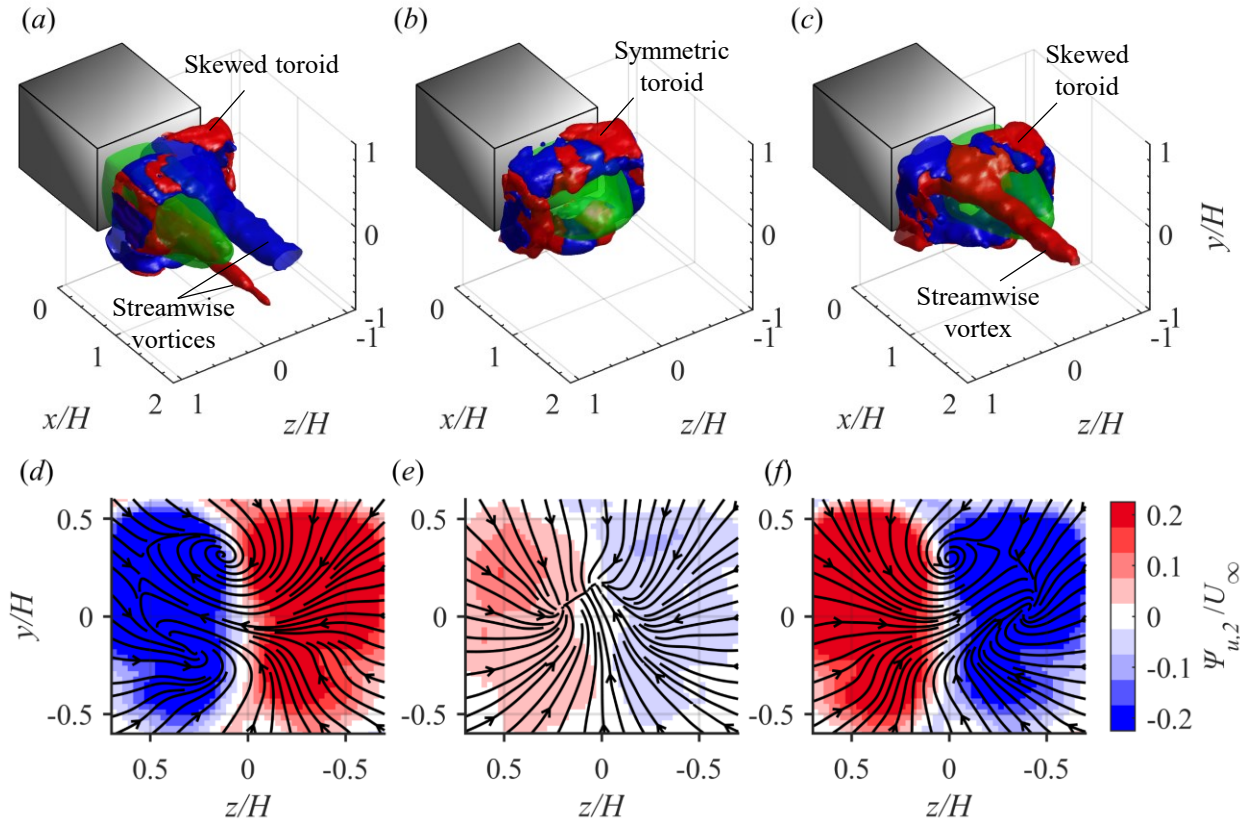

Figure 4.9 Visualizations of the ROM reconstructed from the SPOD mode at $St_H = 0.007$ at (*a*, *d*) $\Phi_1 = \pi$, (*b*, *e*) $\Phi_2 = \pi/2$, and (*c*, *f*) $\Phi_3 = 0.1\pi$. In (*a-c*), the green isosurface shows $U_{ROM} = 0$, red shows $Q' = 0.48$, and blue shows $Q' = -0.48$. In (*d-f*), 2D streamlines correspond to V_{ROM} and W_{ROM} components of the ROM, and the contours show u_{ROM} at the crossflow plane of $x/H = 1.33$.

At the $\Phi_1 = \pi$ in figure 4.9(*a*), vortical structures form a toroidal vortex and two streamwise vortices that extend downstream. The upper streamwise vortex (blue) rotates in a clockwise direction due to its negative ω_x, which is also evident at (y/H, z/H) = (0.4, 0.1) of the *yz* cross-section shown in figure 4.9(*d*). The lower streamwise vortex is weaker and rotates in the counterclockwise direction, resulting in a mushroom-shaped flow pattern of streamlines that induces strong spanwise motion towards positive *z*. The toroid in figure 4.9(a) is skewed, with the side at positive z/H shifted in the downstream direction, and the separation bubble tilted towards positive z/H. This asymmetry is consistent with the barycentre location being at the most positive location at Φ_1 in figure 4.8(*a*). At $\Phi_2 = \pi/2$ in figure 4.9(*b*), the wake symmetry is recovered, and the Q' isosurface shows a symmetrical toroid around the separation bubble, with no evidence of strong streamwise vortices. Figure 4.9(*e*) shows that the magnitude of the SPOD mode ($\Psi_{u,l}$) is small, with the mean velocity dominating the ROM. A stagnation line also appears in the streamlines of figure 4.9(*e*). At phase $\Phi_3 = 0.1\pi$, the separation bubble is tilted toward negative *z*,

and a strong streamwise vortex with counterclockwise rotation appears. Inspection of the streamlines in figure 4.9(*f*) shows that, in addition to this vortex, there is evidence of a weak clockwise vortex that did not appear in the 3D visualization of figure 4.9(*c*). These two vortices result in a strong spanwise motion in the negative z direction. Generally, the flow topology at phase Φ_3 is opposite to that of Φ_1, with the separation bubble tilted towards the negative z direction.

The dynamics of the bi-stable motion shown in figure 4.9 are consistent with the vortical structures of asymmetric states identified by Pavia *et al*. (2018) using stereoscopic PIV in crossflow planes, and by Pavia *et al*. (2020) through flow reconstruction using 3D POD modes. In both investigations, an upper streamwise vortex dominates over a weaker bottom streamwise vortex. Furthermore, Pavia *et al*. (2020) demonstrated that the streamwise vortices originate from the skewed toroid, consistent with visualizations of figure 4.9. However, according to the numerical studies conducted by Dalla Longa *et al.* (2019) and Fan *et al.* (2020), large hairpin vortices separate from the toroid during the switching of asymmetric states. The SPOD mode at $St_H = 0.007$ does not capture these hairpin vortices. It is plausible that the hairpin shedding is captured by the SPOD mode at higher St_H.

The backflow probabilities, γ, have also been calculated using the U_{ROM} of the first SPOD mode at $St_H = 0.007$, and their contours are depicted in figure 4.10(*a*) and (*b*) at the $y/H = 0$ and $x/H = 0.5$ planes, respectively. In figure 4.10(*a*), the darkest red contour ($\gamma = 100\%$) represents the area that always contains a backward flow, whereas the lightest red contour indicates the maximum extent of the backflow region caused by the oscillations of the bi-stable motion. Notably, the contours demonstrate that the backflow region reaches $x/H = 1.74$ and 1.46 when the wake is skewed in the positive and negative z directions, respectively. Consequently, the separation bubble of this ROM model is longer when the wake is skewed toward a spanwise direction. Figure 4.10(*b*) shows a relatively symmetrical distribution of γ in the crossflow plane at $x/H = 0.5$ with no bi-stable motion in the vertical direction.

Figure 4.10(*a*) shows that the separation bubble length, L_s, is longer for asymmetric states than for the symmetric state. The average L_s for $z_b < 0$ is $1.41H$ and for $z_b > 0$ is $1.55H$, both longer than the L_s of $1.24H$ for $z_b = 0$ state. This is in agreement with Grandemange *et al.* (2013) that reported the length of the conditionally-averaged asymmetric wake is slightly longer than the mean separation bubble length. Grandemange *et al.* (2014) also found that L_s of a stable asymmetric

wake forced by a small rod placed in the wake flow becomes 4% longer than the L_s of the undisturbed wake. However, the shorter separation bubble length during $z_b = 0$ in figure 4.10(a) may contradict some findings of Grandemange *et al.* (2014) and Haffner *et al.* (2020). Grandemange *et al.* (2014) also generated a stable symmetric wake by placing a small rod along the spanwise centerline of the wake, resulting in an even longer L_s than that of the asymmetric states. Haffner *et al.* (2020) also reported a 2% longer separation bubble length during wake switching between the two asymmetric states. The apparent discrepancy could be due to the presence of other motions in the symmetric states obtained by Grandemange *et al.* (2014) and Haffner *et al.* (2020) or the method used to obtain the symmetric states in these studies.

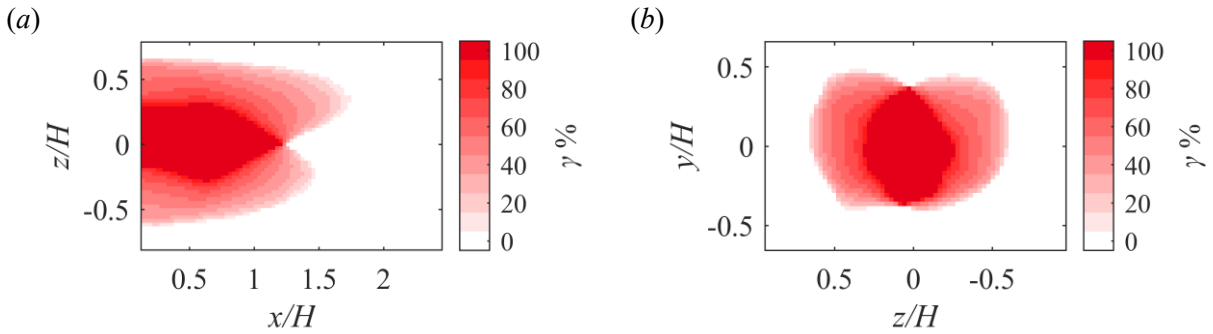

Figure 4.10 The backflow probability, γ, obtained from U_{ROM} of the first SPOD mode at $St_H = 0.007$ in the (a) $y/H = 0$ and (b) $x/H = 0.5$ planes.

Figure 4.11 demonstrates the impact of the SPOD mode at $St_H = 0.007$ on the separation bubble volume by displaying the normalized volume fluctuations of the ROM, represented by Π'_{ROM}, over a 2π duration. It is worth noting that Π'_{ROM} is calculated as $\Pi_{\mathrm{ROM}} - \langle\Pi\rangle$, where $\langle\Pi\rangle$ is the mean separation bubble volume. The figure shows that the volume fluctuations are mostly positive, with a range of $-0.01\langle\Pi\rangle$ to $0.29\langle\Pi\rangle$. This figure, together with the 3D visualizations in figure 4.9, suggest that as the wake tilts in the spanwise direction towards $\Phi_3 = 0.1\pi$ and $\Phi_1 = \pi$, the separation bubble expands. This is also in agreement with the longer L_s observed in figure 4.10 during the asymmetric states. The separation bubble returns to a similar size as $\langle\Pi\rangle$ when the wake symmetry is restored at $\Phi_2 = \pi/2$. Additionally, figure 4.11 reveals that the bi-stable motion results in relatively large variations in volume that can reach up to 30% of $\langle\Pi\rangle$. It is anticipated that the pre-multiplied PSD of Π' in figure 4.4(b) underestimates the energy of fluctuations at $St_H = 0.007$ due to the insufficient samples of wake switching captured in the time-resolved tomo-PIV data.

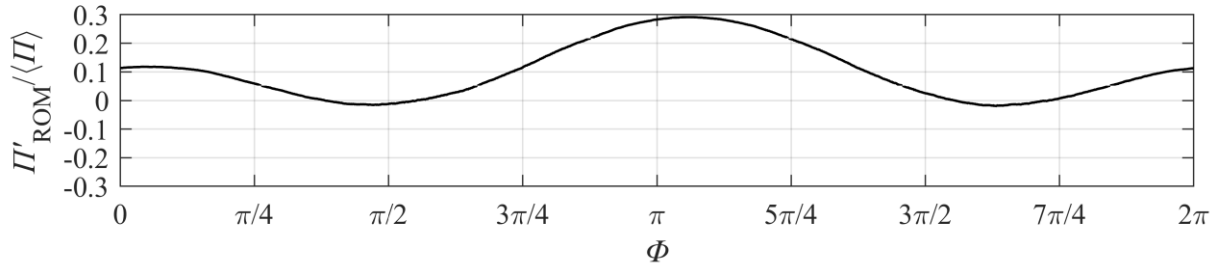

Figure 4.11 The normalized fluctuations of separation volume $\Pi'/\langle\Pi\rangle$ based on U_{ROM} obtained using the first SPOD mode at $St_H = 0.007$.

4.4.2 Swirling motions

This section provides a characterization of the first SPOD mode for the range of $0.014 \leq St_H < 0.123$. Despite the existence of 16 discrete St_H values in this range, the spatial patterns are relatively similar. As a sample, figure 4.12 presents a visualization of the first SPOD mode at $St_H = 0.021$. There are significant differences between the mode shown in figure 4.12 and the bi-stability mode shown in figure 4.7. As seen in figure 4.12(*a*) and (*b*), one of the streamwise elongated structures is weaker and is located closer to the spanwise centre of the wake at $z/H \sim 0$. In addition to the two main structures, there are smaller and weaker structures on the lower side of the wake at approximately $y/H \sim -0.3$, as seen in figure 4.12(*c*). Inspection of the SPOD modes at higher St_H of zone B shows that the strength of the lower structures increases with increasing St_H. Upon inspecting the ROM corresponding to figure 4.12, it is found that the structures are confined to $z/H > -0.4$, implying that this mode primarily affects the flow in the spanwise half of the wake with positive z. Additionally, it depicts the two smaller structures that increase in strength as Φ increases and reach their maximum at $\Phi = \pi/4$ and $5\pi/4$. Unlike the u_{ROM} corresponds to the bi-stability mode in figure 4.7, which demonstrates spanwise switching, these structures demonstrate counterclockwise rotation with increasing phase angle. These observations indicate that the SPOD mode at $St_H = 0.021$ has distinct characteristics that set it apart from the bi-stability mode discussed earlier.

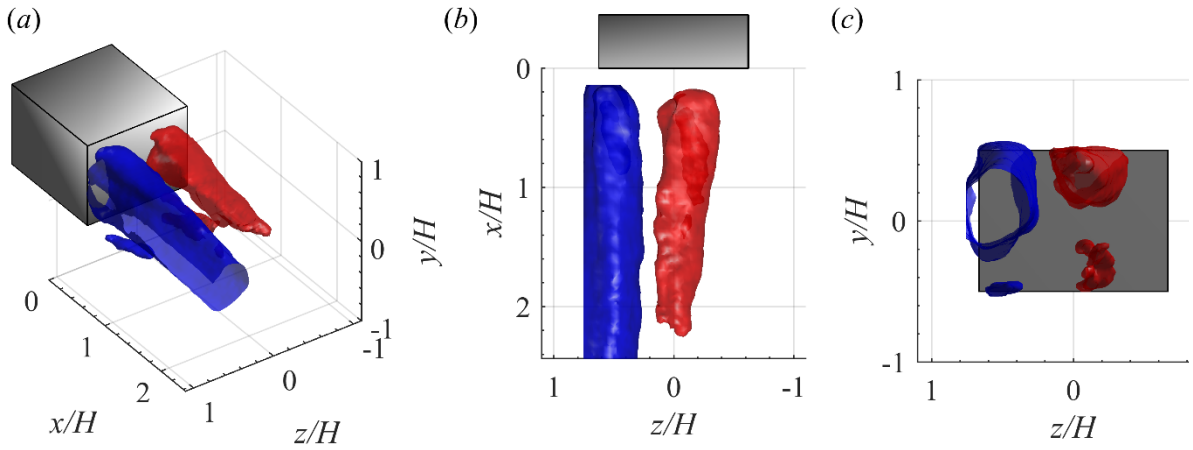

Figure 4.12 Spatial organization of the first SPOD mode at $St_H = 0.021$ in (*a*) isometric view, (*b*) top view, and (*c*) back view. The red and blue isosurfaces show $\Psi_{u,l}/U_\infty = \pm 0.10$ for $l = 4$.

Figure 4.13 illustrates the motion of the barycentre derived from the ROM of each St_H value in the range $0.014 \leq St_H < 0.123$. The figure displays all trajectories with thin blue lines, except for $St_H = 0.021$, which is represented with a black line. For $St_H = 0.021$, the z_b/H fluctuates within a range of −0.01 to 0.07, which is smaller than the spanwise displacement caused by the bi-stability in figure 4.8. The extremums of the z_b/H motion are labeled as $\Phi_1 = 0.1\pi$ and $\Phi_3 = 1.1\pi$, while the phase corresponding to $z_b/H = 0$ is labeled as $\Phi_2 = 0.9\pi$. Although the spanwise motion of the barycentre is small, its vertical location fluctuates approximately from $y_b/H = -0.04$ to -0.02, which is larger than the vertical displacement of the bi-stability in figure 4.8.

All barycentre trajectories in figure 4.13(*a*) indicate that the wake undergoes a swirling motion, consistent with the name given to the motions in this St_H zone. The trajectories display a range of spanwise and vertical displacements, with some exhibiting larger spanwise displacements and others larger vertical displacements. Upon inspecting the St_H of trajectories, it becomes clear that the principal axes of the trajectories gradually transition from a spanwise orientation to a vertical orientation with increasing St_H in figure 4.13(*a*). Figure 4.13(*b*) shows that for $St_H = 0.021$, the streamwise displacement of the barycentre is smaller than its spanwise and vertical motions. The maximum streamwise extension of the barycentre also occurs during the asymmetric state of $\Phi_1 = 0.1\pi$. However, the streamwise displacements of figure 4.13(*b*) reach approximately $0.04H$, indicating that the wake undergoes a combination of displacements in all three directions.

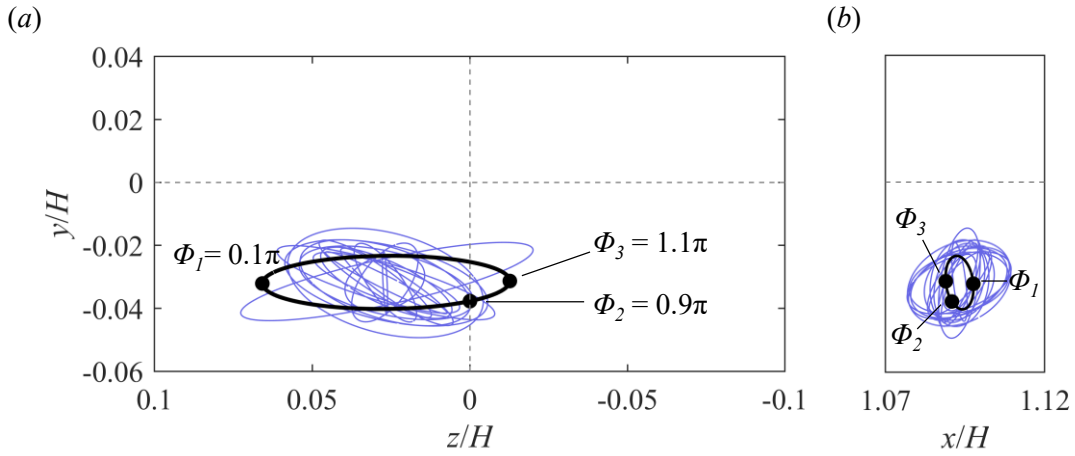

Figure 4.13 The trajectory of the wake barycentre projected in (*a*) *yz* and (*b*) *xy* planes. The coordinates of the barycentre (x_b, y_b, z_b) are obtained from U_{ROM} of the first SPOD mode for each St_H within $0.014 \leq St_H < 0.123$. The black line indicates the U_{ROM} for $St_H = 0.021$, while the blue lines show the trace of other St_H values.

The SPOD mode at $St_H = 0.021$ has been reconstructed at Φ_1, Φ_2, and Φ_3, and the spatial organization is presented in figure 4.14. The top visualizations of the figure show 3D vortical structures and the separation bubble, while the lower figures present 2D contours of streamwise mode magnitude ($\Psi_{u,l}$) and streamlines in $x/H = 1.33$ plane. At Φ_1, as shown in figure 4.14(*a*), the separation bubble is skewed towards the positive z direction, and the toroidal vortex is tilted away from the positive z side of the rear-face. The reconstruction exhibits two counter-rotating streamwise vortices, with the top vortex being stronger and rotating clockwise. This is consistent with the 2D streamlines of figure 4.14(*d*) indicating a mushroom-shape structure. This mushroom-shape structure is skewed towards the region of blue isocontour with higher momentum deficits. In contrast, the reconstructed flow at Φ_2 in figure 4.14(*b*) shows a symmetric separation bubble and toroidal vortex without any indication of a strong streamwise vortex. Inspection of the 2D streamlines in figure 4.14(*e*) reveals a hook-shape structure showing a weak streamwise vortex that was not detected at the Q' threshold used in figure 4.14(*b*). At Φ_3 in figure 4.14(*c*), the separation bubble and the toroidal vortex are approximately symmetric. A pair of weak counter-rotating streamwise vortices appear attached to the upper side of the toroid. The stronger streamwise vortex rotates in the counter-clockwise direction, while the weaker clockwise vortex appears as discontinued isosurfaces. This vortex pair is also seen in figure 4.14(*f*), while the weaker vortex appears as a small spiral attached to the larger vortex. This flow pattern is different from the Φ_3 organization of the bi-stable mode in figure 4.9(*f*) due to higher symmetry and the presence of both streamwise vortices at the top edge of the toroid.

Inspection of the flow reconstruction corresponds to figure 4.14 (*a*-*c*) highlights that the two counter-rotating streamwise vortices gradually decrease in strength, and the toroid becomes symmetrical when it reaches $\Phi_2 = 0.9\pi$. After this phase, two streamwise vortices emerge from the upper part of the toroid and expand fully in the *x* direction at $\Phi_3 = 1.1\pi$, while the separation bubble and toroid become slightly asymmetric. As Φ increases further, the initial counter-rotating streamwise vortices start to form once more and the flow approaches the asymmetric state again. Therefore, the wake oscillates between an asymmetric state (Φ_1) and a symmetric state (Φ_2, Φ_3). This is in contrast to the bi-stability motion in which the wake oscillates between two opposing asymmetric states. However, the asymmetric states observed for $St_H = 0.021$ and $St_H = 0.007$ are similar as both similar counter-rotating streamwise vortices seen in figure 4.9(*a*) and figure 4.14(*a*).

The dynamics of the motions captured at $St_H = 0.021$ resembles those reported by Fan *et al.* (2020) as “switching attempt” The SPOD results suggest that the wake could occasionally retreat from an asymmetric state to a symmetric state instead of a complete switching to the opposing asymmetric state. This motion is also reminiscent of the "swinging motion" observed by Pavia (2019) and Pavia *et al.* (2020) at St_H of 0.02. However, the swinging motion was noted in these investigations as a replacement for bi-stability due to the higher viscous blockage introduced by the wheels of the Windsor model.

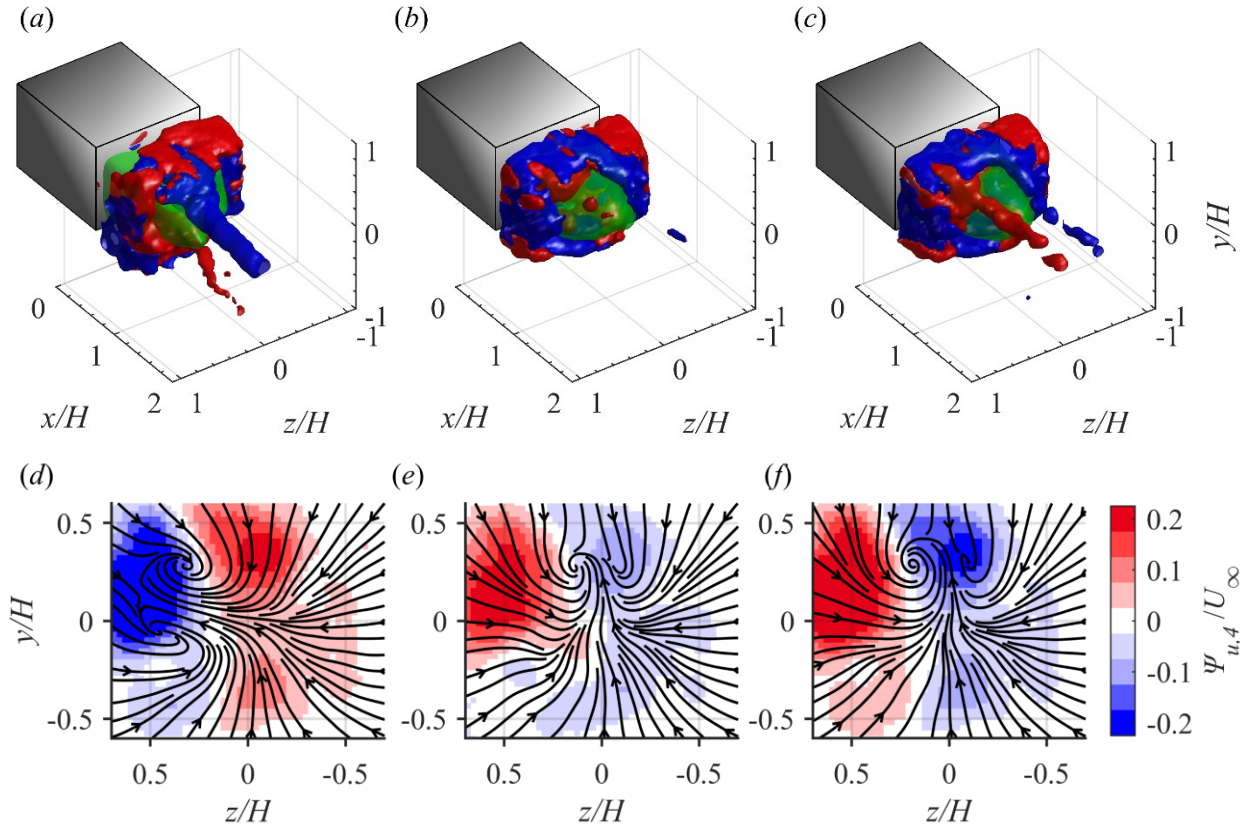

Figure 4.14 Visualizations of the ROM reconstructed from the SPOD mode at $St_H = 0.021$ at (*a*, *d*) $\Phi_1 = 0.1\pi$, (*b*, *e*) $\Phi_2 = 0.9\pi$, and (*c*, *f*) $\Phi_3 = 1.1\pi$. In (*a-c*), the green isosurface shows $U_{\mathrm{ROM}} = 0$, red shows $Q' = 0.24$, and blue shows $Q' = -0.24$. In (*d-f*), 2D streamlines correspond to V and W components of the ROM, and the contours show u_{ROM} for $l = 4$ at the crossflow plane of $x/H = 1.33$.

The probability of backflow based on the U_{ROM} of SPOD mode at $St_H = 0.021$ is depicted in figure 4.15 for *xz* and *yz* cross-sections. Overall, the displacements of the backflow region are relatively small and approximately $0.2H$. The edge of the backflow region oscillates between $x/H = 1.2$ and 1.4 in the streamwise direction, and between $z/H = 0.45$ and 0.62 at the positive spanwise edge. A similar small oscillation is also observed in the vertical direction of figure 4.15(*b*) from $y/H = 0.34$ to 0.42. Therefore, the spanwise displacements are negligible compared to the bi-stable mode in figure 4.10, as there is no indication of a bi-stable motion between two asymmetric states.

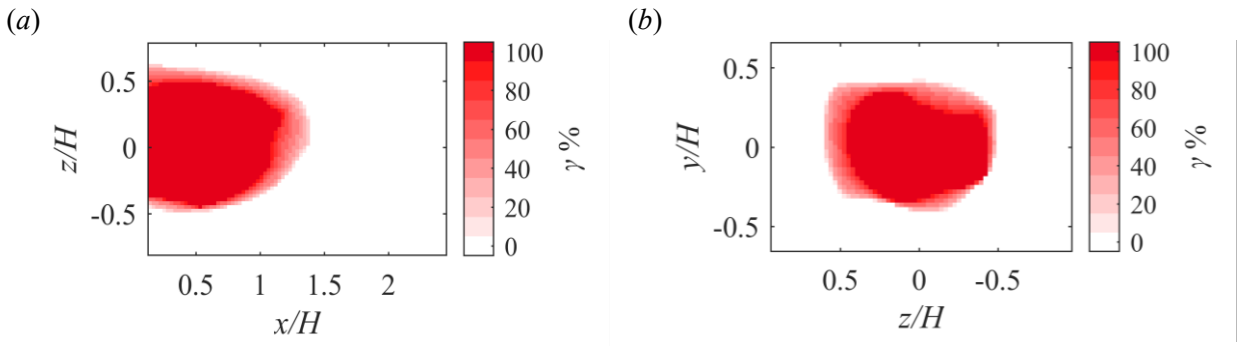

Figure 4.15 Backflow probabilities of U_{ROM} reconstructed using thefirst SPOD mode at $St_H = 0.021$, at (*a*) $y/H = 0$ and (*b*) $x/H = 0.5$ planes.

Figure 4.16 presents the variations in recirculation volume obtained from ROM for each St_H within the range of $0.014 \leq St_H < 0.123$. Thin blue lines represent all St_H cases, except for $St_H = 0.021$, which is illustrated with a black line. The figure shows that the separation volume at $St_H = 0.021$ fluctuates between $\pm 0.03\langle \Pi \rangle$, while for other St_H cases, it can reach larger variations of up to $\pm 0.08\langle \Pi \rangle$. The variations demonstrate that Π' crosses zero near the symmetric states identified by $\Phi_2 = 0.9\pi$ and $\Phi_3 = 1.1$ in figure 4.13. In general, the results indicate that the motions within $0.123 \leq St_H < 0.212$ result in the expansion and contraction of the separation bubble, although the variations are smaller than those of the bi-stable motion depicted in figure 4.11. Moreover, the correlation between volume fluctuations (Π') and the coordinates of the barycentre in figure 4.4(*c*) indicates that Π' within $0.014 \leq St_H < 0.123$ range corresponds to the streamwise oscillations of the wake barycentre. This suggests that the primary cause of volume oscillations is the streamwise motions of the swirling motion.

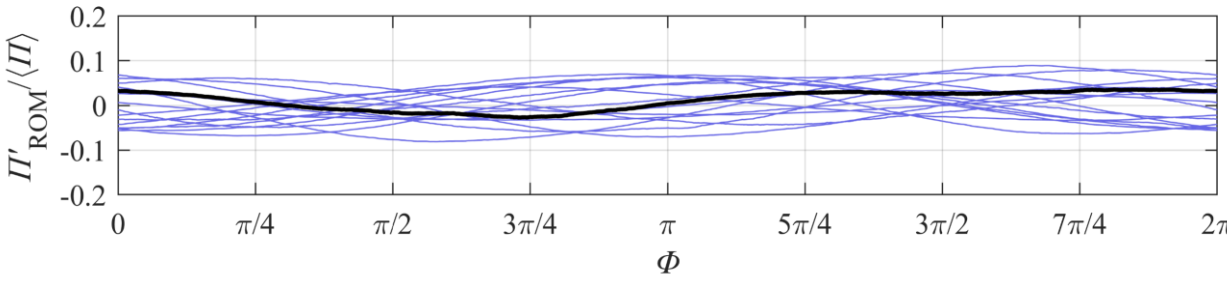

Figure 4.16 The normalized fluctuations of separation volume $\Pi'/\langle \Pi \rangle$ obtained from U_{ROM} for each St_H within $0.014 \leqslant St_H < 0.123$ range. The black line indicates the U_{ROM} for $St_H = 0.021$, while the blue lines show the $\Pi'/\langle \Pi \rangle$ of other St_H values.

The SPOD analysis revealed distinct flow behaviors within the range of $0.014 \leq St_H < 0.123$, characterized as the swirling motion. This swirling motion induces rotational movement of the

wake's barycentre in the *yz* cross-section, leading to oscillations between asymmetric and symmetric wake states. The rotational motion is accompanied by streamwise oscillations of the barycentre, resulting in variations in the separation volume. In the asymmetric state, two counter-rotating streamwise vortices were situated near the vertical edge of the tilted separation bubble. Conversely, in the symmetric state, two counter-rotating vortices originate from the upper edge of the separation bubble.

The observed swirling motion shares similarities with the bubble-pumping mode documented in previous studies. It occurs within the range of $0.014 \leq St_H < 0.123$, which overlaps with the range of $0.04 \leq St_H \leq 0.08$ associated with the bubble pumping mode in prior research (Duell & George 1999; Khalighi *et al.* 2001; Volpe *et al*. 2015; Pavia *et al*. 2018). Furthermore, the dynamics of the swirling motion align with the observed phase relationship of pressure fluctuations on the rear face during the bubble-pumping motion. Specifically, the SPOD mode at $St_H = 0.021$ demonstrates in-phase motions along the vertical edge of the rear face and out-of-phase fluctuations in the spanwise direction, consistent with previous behavior associated with the bubble pumping mode (Volpe *et al.* 2015; Pavia *et al.* 2018). The swirling motion also leads to variations in the separation volume, consistent with observations by Haffner *et al.* (2020). Consequently, the results suggest that the previously identified bubble pumping motion may also encompass wake motions in the vertical and spanwise directions, in addition to streamwise expansions and contractions. The swirling components of the motion might have been overlooked in previous investigations due to the limitations of pointwise and planar measurements.

4.4.3 Vortex shedding

This section investigates the SPOD mode for a range of $0.123 \leq St_H < 0.212$, encompassing 13 discrete frequencies located within zone C. Within this zone, the distinguishing characteristic of the SPOD mode is the manifestation of multiple alternating structures in the streamwise direction. These alternating structures, which exhibit opposite signs in the SPOD modes, result in vortex-shedding behavior. The ROMs of the flow provide further confirmation of this, revealing the presence of large vortical structures that are shed downstream. Such unique features set these structures apart from those observed in other zones.

In figure 4.17, the SPOD mode for a sample $St_H = 0.164$ is displayed. This St_H corresponds to the high energy peak seen in the eigenvalue spectrum of figure 4.6. The SPOD mode displays two vertically oriented pairs of structures with opposite signs, spaced approximately $1H$ apart in the streamwise direction. This spatial arrangement bears resemblance to the third POD mode in figure 4.5(*d*), which was attributed to the wall-normal vortex shedding. However, in contrast to the POD mode, the structures observed in figure 4.17 are exclusively located on the positive spanwise side of the wake ($z/H > 0$). This observation implies a vertical vortex shedding process occurs only at one spanwise side of the rear face. The ROM corresponding to figure 4.17 also demonstrates that these structures are shed from the positive spanwise side of the wake.

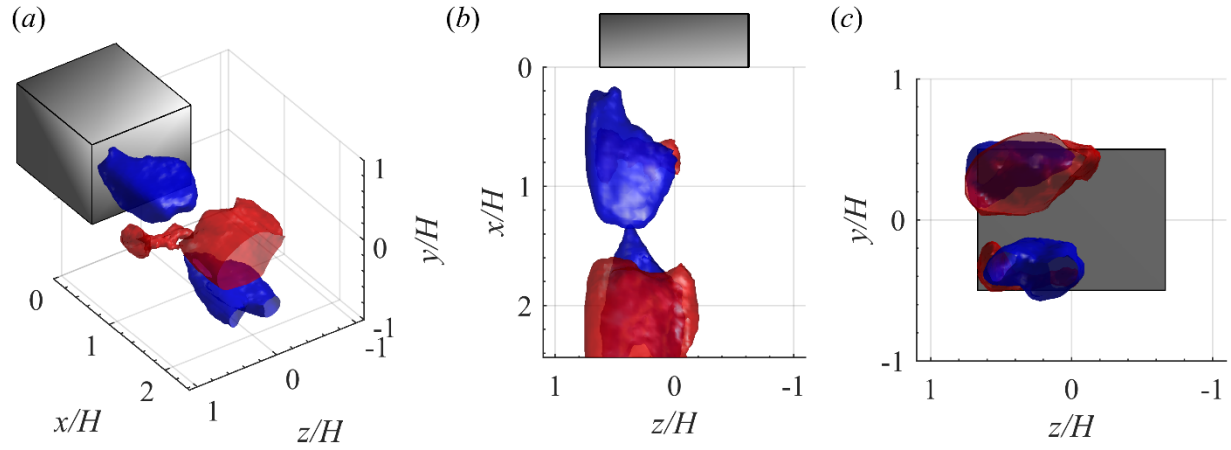

Figure 4.17 Visualization of the first SPOD mode at $St_H = 0.164$ in (*a*) isometric view, (*b*) top view, and (*c*) back view. The red and blue isosurfaces show $\Psi_{u,l}/U_\infty = \pm 0.12$ for $l = 25$.

The barycentre location from the ROM of the modes within $0.123 \leq St_H < 0.212$ range is depicted in figure 4.18. All trajectories are represented by thin blue lines, except for $St_H = 0.164$, which is shown with a thick black line. The barycentre motion for $St_H = 0.164$ follows oblique trajectories in both *yz* and *xy* planes. Specifically, x_b and y_b oscillate over a distance of approximately $0.05H$, while z_b oscillates by a smaller distance of approximately $0.02H$. The order of the motions in each direction is consistent with the order of the magnitudes of spectral peaks observed at $St_H \sim 0.15$ in figure 4.4(*a*). It is also noteworthy that the y_b component exhibits a particularly strong and narrow peak at $St_H = 0.16$ in figure 4.4(*a*), aligning with the St_H of the mode investigated here. The trajectories for most other St_H values show similar orientation and range of motion, with the

exception of a few St_H values that exhibit diagonal displacements in different directions. Overall, the spanwise range of the fluctuations is smaller than that observed for the barycentre displacements caused by bi-stability and swirling motions in figures 4.8 and 4.13. However, the vertical displacement for the vortex shedding motions is larger than those observed for bi-stability and swirling motions. Interestingly, the x_b component follows an oblique trajectory that moves the barycentre upwards and away from the wall, then downwards and closer to the rear face. Therefore, the barycentre motions generated by the vortex shedding motions are distinct from those caused by bi-stability and swirling motions.

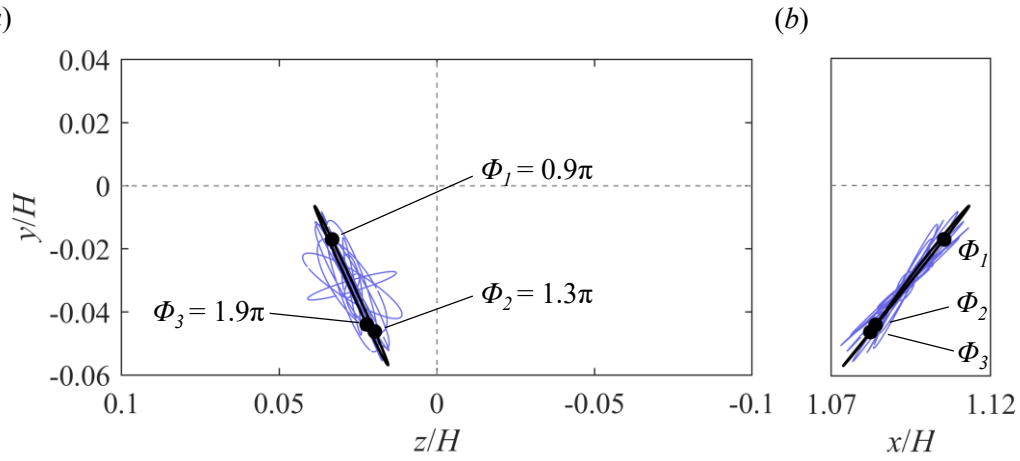

Figure 4.18 The trajectory of the wake barycentre in (*a*) *yz* and (*b*) *xy* planes. The coordinates of the barycentre (x_b, y_b, z_b) are obtained from U_{ROM} of the first SPOD mode for each St_H within $0.123 \leq St_H < 0.212$. The black line indicates the U_{ROM} for $St_H = 0.164$ and the blue lines show the trace of other St_H values.

Figure 4.19 shows the spatial organization of vortical structures at three selected phases of the ROM reconstructed using the SPOD mode at $St_H = 0.164$. These three phases, Φ_1, Φ_2, and Φ_3, are indicated on the barycentre trajectory in figure 4.18. At $\Phi_1 = 0.9\pi$, figure 4.19(*a*) displays two counter-rotating quasi-streamwise vortices that have just detached from the toroidal vortex and extended outwards in the downstream direction. Further inspection of figure 4.19 reveals that the counterclockwise rotating vortex (red isosurface) is located at $z/H = 0.3$, while the clockwise vortex (blue isosurface) is positioned at $z/H = -0.1$. Consequently, the structures are biased towards the positive z region of the wake where the barycentre is located. These quasi-streamwise vortices move downstream and out of the measurement domain with increasing Φ. At $\Phi_2 = 1.3\pi$, only the tail of these vortices is visible in the downstream region of figure 4.19(*b*). As Φ increases further, a new pair of quasi-streamwise vortices with an opposite direction of rotation emerged from the

toroid's centre. In figure 4.19(*c*) at $\Phi_3 = 1.9$, the new vortex pair is extended in the downstream direction, and their rotation is opposite to those observed at Φ_1. Here, the most important finding is that the shedding structures are in the form of quasi-streamwise vortices. Upon examining other ROMs in the St_H range of zone C, the results indicate that the shedding process mainly consists of quasi-streamwise vortices.

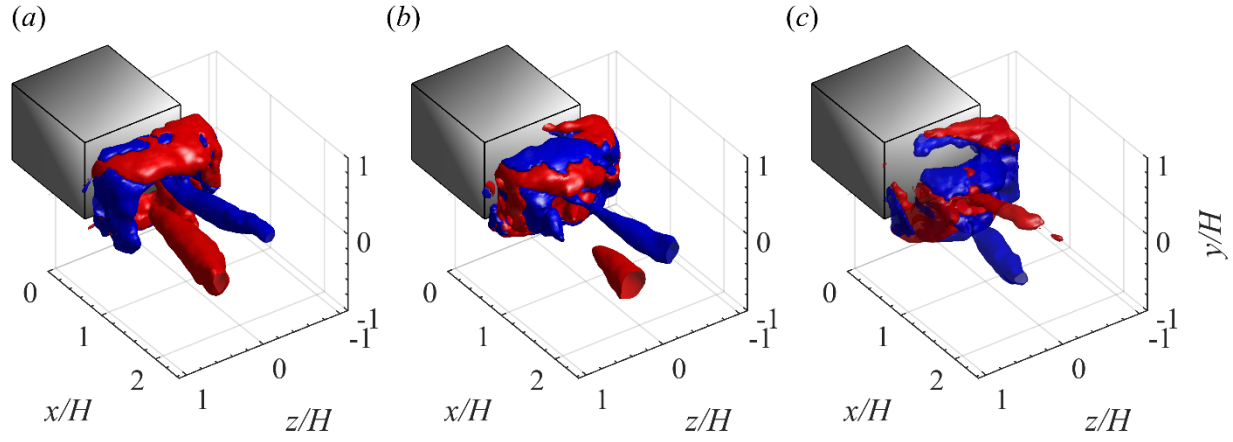

Figure 4.19 Visualizations of the ROM reconstructed from the first SPOD mode at $St_H = 0.164$ at (*a*) $\Phi_1 = 0.9\pi$, (*b*) $\Phi_2 = 1.3\pi$, and (*c*) $\Phi_3 = 1.9\pi$. The red isosurface shows $Q' = +0.52$, and blue shows $Q' = -0.52$.

To demonstrate how vortex shedding results in velocity fluctuations, figure 4.20 illustrates v_{ROM} and w_{ROM} of the SPOD mode at $St_H = 0.164$. The reconstructions correspond to the three selected phases, Φ_1, Φ_2, and Φ_3. At $\Phi_1 = 0.9\pi$ in figure 4.20(*a*), the velocity field displays two large zones of upward and downward velocity fluctuations, centered at $z/H = 0.17$ and alternating in the streamwise direction. The two streamwise vortices seen in figure 4.19(*a*) generate the Y-shaped downward velocity region, while they induce a combined zone of upward velocity. These vortices also generate strong spanwise motions, as seen in figure 4.20(*d*). The spanwise motion near the rear face is towards negative z, forming a spanwise asymmetric structure, while farther away, two zones with positive and negative spanwise motions are present. The spanwise motions are mainly in the positive z region, which is consistent with stronger streamwise vorticity observed at positive z region for this mode. These vertical and spanwise motions persist and advect downstream, as seen at $\Phi_2 = 1.3\pi$ in figure 4.20(*b*) and (*e*). Similarly, figure 4.20(*c*) and (*f*), corresponding to $\Phi_3 = 1.9\pi$, show similar structures as Φ_1 but with opposite magnitudes, consistent with the reversal of the direction of rotation of the vortices in figure 4.19(*c*).

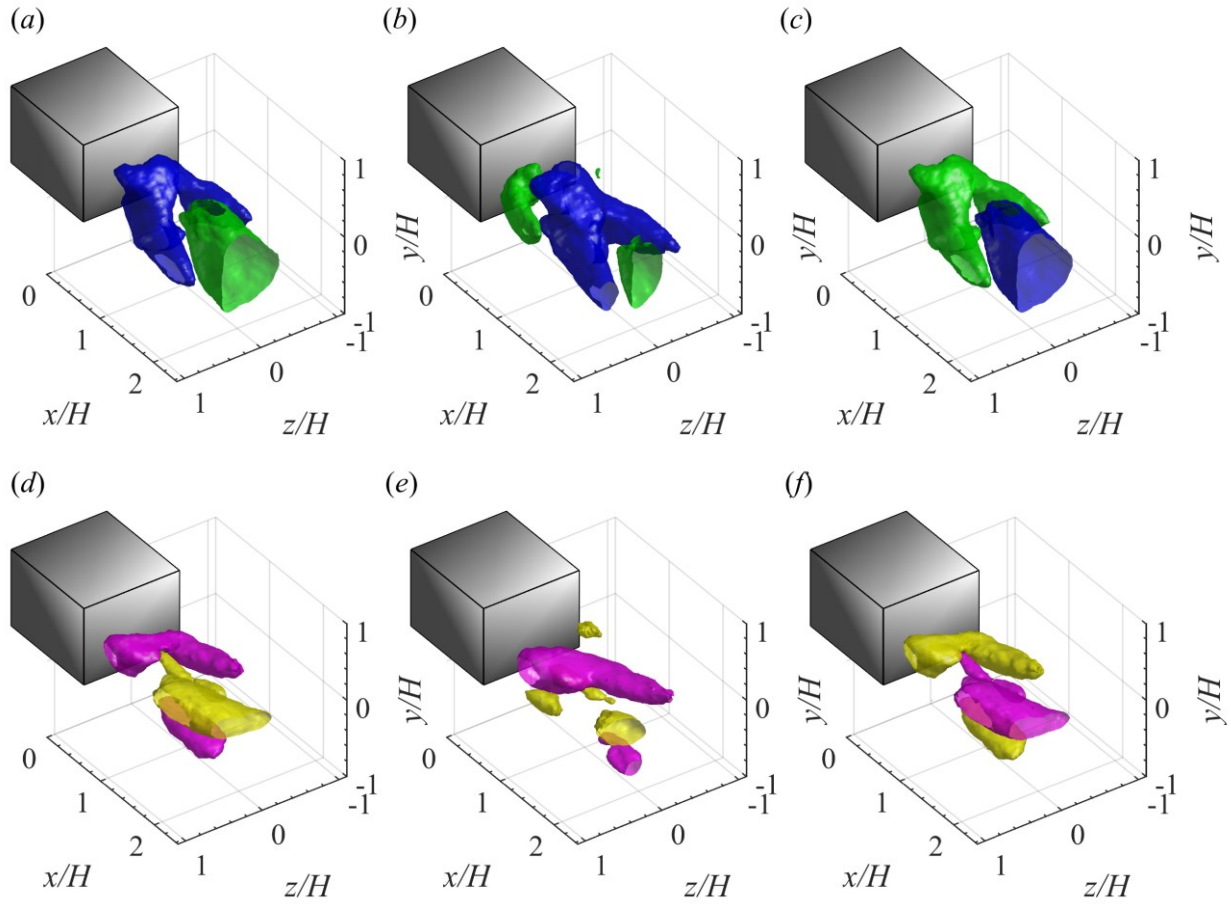

Figure 4.20 Visualizations of the v_{ROM} and w_{ROM} of the SPOD mode at $St_H = 0.164$ at (*a*, *d*) $\Phi_1 = 0.9\pi$, (*b*, *e*) $\Phi_2 = 1.3\pi$, and (*c*, *f*) $\Phi_3 = 1.9\pi$. In (*a*-*c*), the green isosurface shows $v_{ROM} = +0.1$, and blue shows $v_{ROM} = -0.1$. In (*d*-*f*), yellow isosurface shows $w_{ROM} = +0.1$, and pink shows $w_{ROM} = -0.1$.

Figure 4.21 illustrates the variations of the recirculation volume for the vortex shedding modes. All trajectories are shown with thin blue lines except for $St_H = 0.164$, which is shown in black. The ROM shows that Π' varies between $-0.06\langle\Pi\rangle$ to $+0.09\langle\Pi\rangle$ at $\Phi_1 = 0.8\pi$ and $\Phi_3 = 1.9\pi$, respectively. Inspection of the ROM corresponding to figure 4.19 reveals that the minimum Π' corresponds to the moment when the streamwise vortices have reached full extension but are still connected to the toroidal vortex. As the new vortices form and grow, Π' gradually increases and reaches its maximum value. The magnitude of volume fluctuations is comparable to those of the swirling motion seen in figure 4.16 but smaller than the bi-stable motion illustrated in figure 4.11.

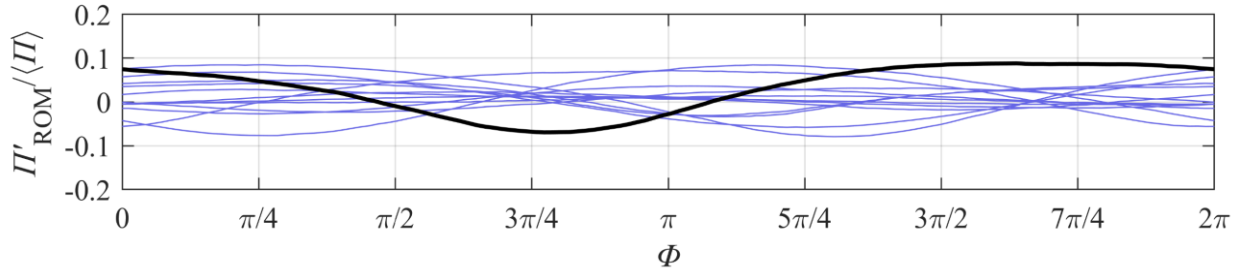

Figure 4.21 The normalized fluctuations of separation volume $\Pi'/\langle\Pi\rangle$ obtained from U_{ROM} of the SPOD modes within $0.123 \leqslant St_H < 0.212$ range. The black line indicates $St_H = 0.164$, while the blue lines show other St_H.

The present investigation highlights that the shedding of a pair of counter-rotating quasi-streamwise vortices is the primary mechanism behind vortex shedding, leading to regions of spanwise and vertical velocity fluctuations. Notably, flow visualization experiments conducted by Grandemange *et al.* (2012) at $Re_H = 365$ also indicate the presence of alternating quasi-streamwise vortices shed from the centre of the toroid, although they referred to them as vortex loops. Similarly, phase-averaged visualizations by Evstafyeva *et al.* (2017) based on simulations at $Re_H = 435$ showed that vortex shedding primarily involved quasi-streamwise structures extending from the toroid's centre and skewed towards one spanwise side. Based on analyzing the coherence function and spectra of hotwire measurements at Re_H of 9.2×10^4, Grandemange *et al.* (2013) suggested that separate vortex loops shed from the vertical and horizontal edges of the rear-face at different frequencies. They explained that the rotational direction of vortex loops shed from the horizontal edges alternate, while the rotation direction of vortices shed from the vertical edge remained consistent due to the spanwise bi-stability. Grandemange *et al.* (2013) noted the difficulty of presenting a combined sketch of the two shedding loops due to their distinct frequencies. The simulation conducted by Lucas *et al*. (2017) also provides some evidence of one-sided vortex loops shed in instantaneous visualizations. However, at the high Re_H of 4.0×10^5, the cluttered nature of the vortical structures made it challenging to accurately characterize the vortex topology. The shapes of these vortex loops bear resemblance to the shedding of instantaneous hairpin-like structures observed just before the wake switching in numerical simulations by Dalla Longa *et al.* (2019) and Fan *et al.* (2020).

4.4.4 Shear layer instability

To examine the spatiotemporal dynamics of fluctuations within the $1.024 \leq St_H < 1.228$ range, the SPOD mode at $St_H = 1.147$ is presented in figure 4.22. This St_H corresponds to the peak in the eigenvalue spectrum shown in figure 4.6. Figure 4.22 shows small structures with alternating sign along the shear layers. Stronger structures are observed in the vertical shear layers while the structures in the lower shear layer are weak and barely visible in figure 4.22. Throughout the periodic cycle, the ROM corresponding to figure 4.22 demonstrates that these structures evolve along the shear layers and gradually diminish as they move downstream.

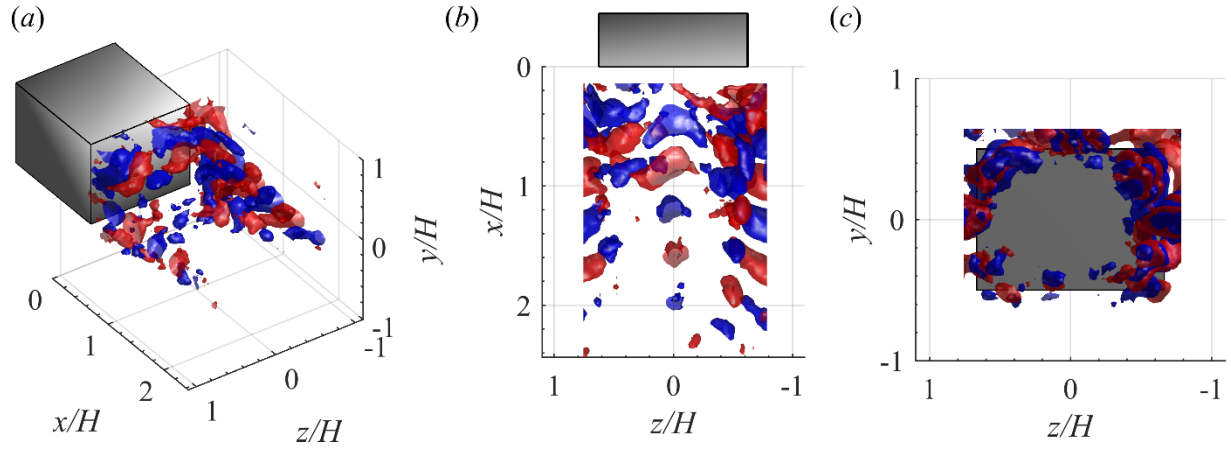

Figure 4.22 Spatial organization of the first SPOD mode at $St_H = 1.147$ in (*a*) isometric view, (*b*) top view, and (*c*) back view. The red and blue isosurfaces show $\Psi_{u,l}/U_\infty = \pm 0.025$ for $l = 169$.

To understand the source of the structures observed in figure 4.22, their Strouhal number is calculated using the local thickness of the shear layer (ξ), which is obtained based on the thickness of the layer with intense vorticity measured using planar PIV. At $x/H = 0.3$, ξ is found to be $0.16H$ for both upper and lower shear layers. The Strouhal number of the structures, calculated as $St_\xi = f \times \xi / U_\infty$ with $f = 15.14$ Hz and $\xi = 0.16H$, is determined to be 0.18. This value is similar to the Strouhal number of 0.2 obtained from the linear stability theory for Kelvin-Helmholtz instabilities (Monkewitz & Huerre 1982). Therefore, the analysis suggests that the structures observed in figure 4.22 are generated by the instabilities of the shear layers. The structures observed in figure 4.22 are consistent with those identified in the SPOD mode at $St_H \approx 1$ by Haffner *et al.* (2020). They applied SPOD analysis to velocity fields in the streamwise-spanwise plane and light intensity images in the wall-normal-streamwise. Their analysis revealed that the spatial pattern of the SPOD

mode at $St_H \approx 1$ is linked to the interaction between the recirculating flow and the shear layer on the opposite side, leading to the amplification of shear layer instabilities and the roll-up of vortices.

Figure 4.23(a) displays the isosurface of $Q^* = QH^2/U_\infty^2$ for $St_H = 1.147$, computed using the velocity fields obtained from the ROM at $\Phi = 0$. The visualization shows two successive toroidal vortical structures that resemble the toroidal vortex of the mean flow. In addition, the ROM corresponds to figure 4.23 shows that these toroidal vortices gradually weaken and eventually vanish as they move downstream. Furthermore, figure 4.23(b) presents the vertical velocity fluctuations, which consist of small structures along the span of the top and side shear layers. In contrast, the spanwise velocity fluctuations in figure 4.23(c) are predominantly observed in the side shear layers. After examining the spatial variations of the barycentre and the fluctuations of separation volume, it was found that they are negligible compared to those of previously discussed flow motions. As a result, the corresponding plots are not included here to keep the discussion short.

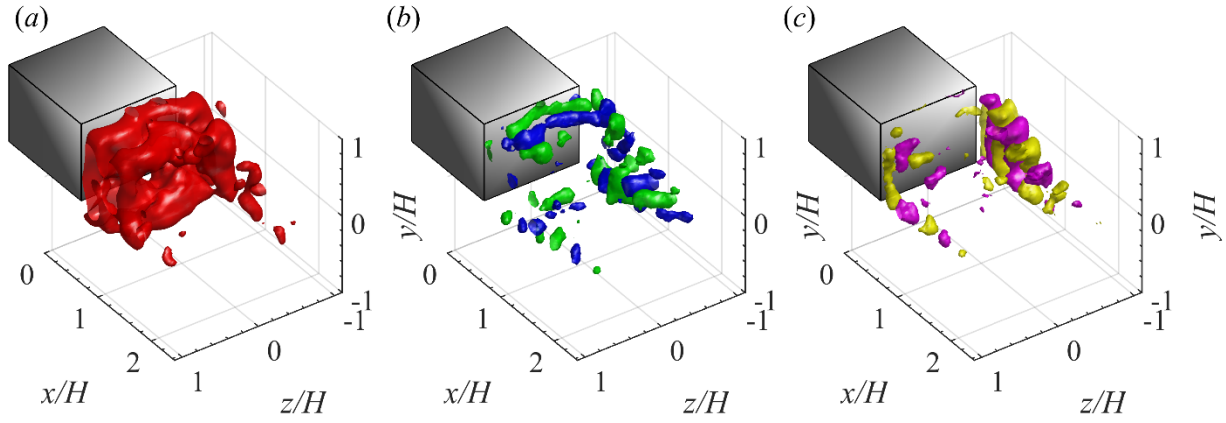

Figure 4.23 Visualizations of ROM obtained for the SPOD mode at $St_H = 1.147$ at $\Phi = 0$. (a) The red isosurface shows $Q^* = 0.16$, (b) green and blue isosurface shows $v_{ROM} = +0.035$ and -0.035, respectively, (c) yellow and pink isosurfaces show $w_{ROM} = +0.035$ and -0.035, respectively.

Chapter 5. Conclusion

The wake of a flat-back Ahmed body has been investigated at Re_H = 10,000 using planar and tomo-PIV. The motivation of the current investigation is to address the uncertainties from previous investigations stemming from measurements limitation and the inherent shortcoming of space-only POD technique in differentiating flow motions at different frequencies. Thus, a unique combination of time-resolved 3D flow measurement and SPOD was employed to discern the coherent flow motions of the wake for each discrete frequency.

In the current mean flow analysis, the topology of rear recirculation region was characterized by a symmetrical toroidal-shaped vortical structure. Furthermore, the presence of spanwise bi-stability was confirmed by examining the JPDF of the two barycentre coordinates (y_b, z_b) of the flow. The results indicated two high-probability peaks at (z, y) = ($\pm 0.05H$, $-0.03H$) that are symmetrical about the vertical symmetry plane. Moreover, spectral analysis of barycentre coordinates and Π' indicated energetic flow motions at different St_H. According to the current spectral and coherence analyses, these flow motions were speculated to be associated with the known wake dynamics, including bi-stability, bubble pumping, vortex shedding, and shear layer instability.

A 3D POD analysis was performed to investigate the energetic flow motions of the wake. The first POD mode captures the spanwise asymmetry of the wake attributed to the bi-stability with 9.1% of the total turbulent kinetic energy. The higher-order modes represent flow dynamics, such as vortex shedding and bubble pumping, with energies below 1.5%. In general, the spatial characteristics of the six leading POD modes are in agreements with previous studies.

The first SPOD mode is primarily characterized that represents the largest contribution of total turbulent kinetic energy of the flow. It was found that 78% of the total energy in the first SPOD mode is contributed by flow motions at $St_H < 1.228$. Based on the spatiotemporal characteristics of the first SPOD mode, the wake was categorized into four types of flow motions, each

corresponding to a specific range of St_H. This current study further elucidated the bi-stability, vortex shedding, and shear layer instability phenomena observed in the Ahmed body wake. Additionally, it uncovers a previously unidentified flow motion referred to as the swirling motion. An overview of each motion is listed below:

(i) At $St_H < 0.014$: the wake exhibited the spanwise bi-stability with 11% of the total energy in the first SPOD mode. This bistable motion induced prominent wake oscillations in the spanwise direction, causing the wake to alternate between two asymmetric states. In the asymmetric state, the wake topology comprised a toroidal vortex skewed towards the wake barycenter, along with a pair of streamwise vortices attached to it. These streamwise vortices were vertically oriented, in which the upper vortex demonstrated a greater strength in comparison. As the wake transitioned from an asymmetric to a symmetric state, the symmetry of the toroid and separation was recovered, while the streamwise vortices vanished. When the wake is switched to the opposing asymmetric state, the streamwise vortices gradually reappeared from the toroid, while the rotational directions of these vortices are opposite to those from the previous asymmetric state. A notable variation in the separation bubble was observed in the results as the wake transitioned from an asymmetric to a symmetric state. Specifically, the streamwise length of the separation bubble increased from $1.24H$ to $1.55H$, and its volume expanded by 30% compared to the mean separation bubble volume.

(ii) At $0.014 \leq St_H < 0.123$: The swirling motions of the wake were discovered in the current research, associating with 18% of the total energy of the flow. The flow motion resulted in a rotational movement of the wake barycentre within one spanwise half of the crossflow plane. Unlike the bi-stable motion, the swirling motion only causes the wake to oscillate between the symmetric state and one asymmetric state, for which each topology is characterized by a pair of counter-rotating streamwise structures that is horizontally or vertically oriented, respectively. This observation of the swirling motion is resembled of the "switching attempts" mentioned in previous studies. In addition to the rotational motion, the swirling motion also induced a notable displacement of the barcentre in the streamwise direction, which resulted in volume variations of the separation bubble up to about ±8% with respect to the mean volume of the separation. The current results indicate that previous investigations

have neglected the inherent swirling component of the previously identified bubble pumping motion within the crossflow plane due to limitations in measurement techniques.

(iii) At $0.123 \leq St_H < 0.212$: the vortex shedding motions were associated with 26% of the total energy. The associated topologies were primarily associated with a pair of counter-rotating quasi-streamwise vortices shedding downstream from the toroid's off-center. These vortices induced regions of wall-normal and spanwise fluctuations that advected downstream. Furthermore, the vortex shedding motions caused the wake to oscillate obliquely in the crossflow and streamwise-vertical planes. Compared to the swirling and bi-stable motions, the vortex shedding exhibited more substantial wall-normal motions. The current analysis revealed that the magnitudes of volume variations within the separation bubble for vortex shedding motions are smaller than the bi-stable motion, but comparable to that induced by swirling motions.

(iv) At $1.024 \leq St_H < 1.228$: The Kelvin-Helmholtz instability within the shear layers associated to a mere 3% of the total energy with negligible modifications to the wake barycentre and the volume of the seperation bubble. The topology of the instability was characterized by the shedding of toroidal vortices, which rapidly dissipated within the near wake as they advect downstream. The presence of vortices generates minor vertical velocity fluctuations in the upper shear layer and spanwise velocity fluctuations in the lateral shear layers. Nevertheless, the impact of these toriodal vortices on the overall dynamics of the wake is deemed relatively inconsequential, as evidenced by the minimal influences observed in the wake barycenter and separation bubble volume.

Overall, the current investigation facilitated a better understanding of the wake dyanmics in the flat-back Ahmed body by combining SPOD and time-resolved tomo-PIV techniques. covering flow motions with a broad spectrum of temporal scales. The previously discussed phenomena of bi-stability, bubble pumping, and vortex shedding were further clarified by the current study, which also introduced the novel concept of swirling motions in the wake of the Ahmed body.

Bibliography

AHMED, S. R., RAMM, G. & FALTIN, G. 1984 Some Salient Features of the Time-Averaged Ground Vehicle Wake. *SA Technical Paper*, 840300.

ATKINSON, C., & SORIA, J. 2009 An efficient simultaneous reconstruction technique for tomographic particle image velocimetry. *Exp. Fluids* 47 (4–5), 553.

BRASLOW A. L. & KNOX E. C. 1958 Simplified method for determination of critical height of distributed roughness particles for boundary-layer transition at Mach numbers from 0 to 5. *NACA TN* 4363.

BERGER, E., SCHOLZ, D. & SCHUMM, M. 1990 Coherent vortex structures in the wake of a sphere and a circular disk at rest and under forced vibrations. *J. Fluids Struct*., 4, pp. 231–257.

BARLOW, J., GUTERRES, R., RANZENBACH, R., AND WILLIAMS, J. 1999 Wake Structures of Rectangular Bodies with Radiused Edges Near a Plane Surface. SAE Technical Paper, 1999-01-0648.

BEARMAN, P. W. 1997 Near Wake Flows Behind Two- and Three-Dimensional Bluff Bodies. J. Wind. Eng. Ind. Aerodyn., 69–71, pp. 33–54.

BEWLEY G.P., SREENIVASAN, K.R. & LATHROP, D.P. 2008 Particles for tracing turbulent liquid helium. *Exp. Fluids* 44, pp.887–896.

BAGHERI, S. 2013 Koopman-mode decomposition of the cylinder wake. *J. Fluid Mech*, 726, 596–623.

BOOYSEN A., DAS P. & GHAEMI S. 2022 Large-scale 3D-PTV measurement of Ahmed-body wake in crossflow. *Experimental Thermal and Fluid Science*, 132, 110562, ISSN 0894-1777.

CROLL, R.H., GUTIERREZ, W.T., HASSAN, B., SUAZO, J.E., RIGGINS, A.J. 1996 Experimental Investigation of the Ground Transportation Systems (gts) Project for Heavy Vehicle Drag Reduction. *Technical Report, SAE Technical Paper*.

CABITZA, S. 2013 Active control of the wake from a rectangular-sectioned body. PhD thesis, Imperial College London.

CHOI, H., LEE, J., & PARK, H. 2014 Aerodynamics of heavy vehicles. *Annual Review of Fluid Mechanics*, 46, pp. 441-468.

CADOT, O., EVRARD, A. & PASTUR, L. 2015 Imperfect supercritical bifurcation in a three-dimensional turbulent wake. *Phys. Rev.*, E 91 (6), 063005.

DUELL, E. G. & GEORGE, A. R. 1999 Experimental study of a ground vehicle body unsteady near wake. *SAE Trans*. 108 (6; Part 1), pp. 1589–1602.

DALLA LONGA, L., EVSTAFYEVA, O. & MORGANS, A. S. 2019 Simulations of the bi-modal wake past three-dimensional blunt bluff bodies. *J. Fluid Mech*. 866, pp. 791–809.

ELSINGA, G. E., SCARANO, F., WIENEKE, B., VAN OUDHEUSDEN, B. W. 2006 Tomographic particle image velocimetry. *Exp Fluids* 41, pp. 933–947.

ELSINGA, G. E., WESTERWEEL, J. 2012 Tomographic-PIV measurement of the flow around a zigzag boundary layer trip. *Exp. Fluids* 52, pp.865–876.

EVRARD, A., CADOT, O., HERBERT, V., RICOT, D., VIGNERON, R. & DÉLERY, J. 2016 Fluid force and symmetry breaking modes of a 3D bluff body with a base cavity. *J. Fluids Struct*. 61, pp.99–114.

EVSTAFYEVA, O., MORGANS, A. S. & DALLA LONGA, L. 2017 Simulation and feedback control of the Ahmed body flow exhibiting symmetry breaking behavior. *J. Fluid Mech*. 817, R2.

FAN, Y., CHAO, X., CHU, S., YANG, Z. & CADOT, O. 2020 Experimental and numerical analysis of the bi-stable turbulent wake of a rectangular flat-backed bluff body. *Phys. Fluids* 32, 105111.

GRANDEMANGE, M., GOHLKE, M. & CADOT, O. 2012 Reflectional symmetry breaking of the separated flow over three-dimensional bluff bodies. *Phys. Rev.* E 86, 035302(R).

GRANDEMANGE, M., GOHLKE, M. & CADOT, O. 2013 Turbulent wake past a three-dimensional blunt body. Part 1. Global modes and bi-stability. *J. Fluid Mech*. 722, pp.51–84.

GRANDEMANGE, M., GOHLKE, M., & CADOT, O. 2014 Turbulent wake past a three-dimensional blunt body. Part 2. Experimental sensitivity analysis. *J. Fluid Mech*. 752, pp.439-461.

HUNT, J. C. R., WRAY, A. A. & MOIN, P. 1988 Eddies, stream, and convergence zones in turbulent flows. In Proc. *2nd Summer Program*, *Center for Turb. Research*, *Stanford Univ.*, pp. 193–208.

HOWELL, J., SHEPPARD, A., and BLAKEMORE, A. 2003 Aerodynamic Drag Reduction for a Simple Bluff Body Using Base Bleed. SAE Technical Paper 2003-01-0995.

HANSON, R.E., BUCKLEY, H.P., & LAVOIE, P. 2012 Aerodynamic optimization of the flat-plate leading edge for experimental studies of laminar and transitional boundary layers. *Experiments in Fluids* 53, pp. 863-871.

HAFFNER, Y., BORÉE, J., SPOHN, A. & CASTELAIN, T. 2020 Mechanics of bluff body drag reduction during transient near-wake reversals. *J. Fluid Mech*., 894, A14.

KRAJNOVIC, S., & DAVIDSON, L. 2003 Numerical Study of the Flow Around a Bus-Shaped Body. *J. Fluids Eng*. 125 (3), pp. 500–509.

KANG, N., ESSEL, E.E., ROUSSINOVA, V. & BALACHANDAR, R. 2021 Effects of approach flow conditions on the unsteady three-dimensional wake structure of a square-back Ahmed body. *Phys. Rev. Fluids* 6, 034613.

KHALIGHI, B., ZHANG, S., KOROMILAS, C., BALKANYI, S. R., BERNAL, L. P., IACCARINO, G. & MOIN, P. 2001 Experimental and computational study of unsteady wake flow behind a bluff body with a drag reduction device. *SAE Paper* 2001-01-1042.

HERRY, B. B., KEIRSBULCK, L. & PAQUET, J. B. 2011 Flow bi-stability downstream of three-dimensional double backward facing steps at zero-degree slideslip. *Trans. ASME: J. Fluids Eng.* 133, 1–4.

KHALIGHI, B., CHEN, K. & IACCARINO, G. 2012 Unsteady aerodynamic flow investigation around a simplified square-back road vehicle with drag reduction devices. *ASME*. *J. Fluids Eng*. 134(6), 061101.

LAWSON, N. J., GARRY, K. P. & FAUCOMPRET, N. 2007 An investigation of the flow characteristics in the bootdeck region of a scale model notchback saloon vehicle. *Proc. Inst. Mech. Engrs D: J. Automobile Eng.* 221 (D6), 739–754.

LAHAYE, A., LEROY, A. & KOURTA, A. 2013 Characterisation of a square back Ahmed body near wake flow. *In 21eme Congres Francais de Mecanique Bordeaux* pp. 1-6.

LI, R., BARROS, D., BORÉE, J., CADOT, O., NOACK, B. R. & CORDIER, L. 2016 Feedback control of bimodal wake dynamics. *Exp. Fluids* 57 (10), pp. 158.

LUCAS, J. M., CADOT, O., HERBERT, V., PARPAIS, S. & DÉLERY, J. 2017 A numerical investigation of the asymmetric wake mode of a squareback Ahmed body – effect of a base cavity. *J. Fluid Mech*. 831, pp. 675–697.

LUMLEY, J. L. 1970 Stochastic Tools in Turbulence. *Academic Press*.

MCARTHUR, D., BURTON, D., THOMPSON, M. & SHERIDAN, J. 2016 On the near wake of a simplified heavy vehicle. *J. Fluids Struct*. 66, pp. 293–314.

NEKKANTI, A., & SCHMIDT, O. 2021 Frequency–time analysis, low-rank reconstruction and denoising of turbulent flows using SPOD. *J. Fluid Mech* 926, A26.

PATTEN, J., POOLE, G., MAYDA, W. & WALL, A. 2010 Trailer Boat Tail Aerodynamic and Collision Study. *National Research Council of Canada*. NRC Technical Report No. CSTT-HVC-TR-169.

PATTEN, J., MCAULIFFE, B., MAYDA, W. & TANGUAY, B. 2012 Review of aerodynamic drag reduction devices for heavy trucks and buses. *National Research Council of Canada*. NRC Technical Report No. CSTT-HVC-TR-205.

PERRY, A.K., ALMOND, M.T., PASSMORE, M., & LITTLEWOOD, R.A. 2016a The study of a bi-stable wake region of a generic squareback vehicle using tomographic PIV. *SAE International Journal of Passenger Cars - Electronic and Electrical Systems* 9, pp. 743-753.

PERRY, A.K., PAVIA, G. & PASSMORE, M. 2016b Influence of short rear end tapers on the wake of a simplified square-back vehicle: wake topology and rear drag. *Exp. Fluids* 57, pp.169.

PAVIA, G., PASSMORE, M. & SARDU, C. 2018 Evolution of the bi-stable wake of a square-back automotive shape. *Exp. Fluids* 59 (1), 20.

PAVIA, G. 2019 Characterisation of the unsteady wake of a square-back road vehicle (Version 1). *Loughborough University*.

PLUMEJEAU, B., DELPRAT, S., KEIRSBULCK, L., LIPPERT, M. & ABASSI, W. 2019 Ultra-local model-based control of the square-back Ahmed body wake flow. *Physics of Fluids* 31, 085103.

PAVIA, G., PASSMORE, M. A., VARNEY, M. & HODGSON, G. 2020 Salient three-dimensional features of the turbulent wake of a simplified square-back vehicle. *J. Fluid Mech*., 888, A33.

PODVIN, B., PELLERIN, S., FRAIGNEAU, Y., EVRARD, A. & CADOT, O. 2020 Proper orthogonal decomposition analysis and modelling of the wake deviation behind a squareback Ahmed body. *Phys. Rev. Fluids* 5, 064612.

PODVIN, B., PELLERIN, S., FRAIGNEAU, Y., BONNAVION, G., & CADOT, O. 2021 Low-order modelling of the wake dynamics of an Ahmed body. *J. Fluid Mech*. **927**, R6.

ROWLEY, C. W., MEZIC, I., BAGHERI, S., SCHLATTER, P. & HENNINGSON, D. S. 2009 Spectral analysis of nonlinear flows. *J. Fluid Mech*. 641, pp. 115–127

RAFFEL, M., WILLERT, C. E., WERELEY, S. T., & KOMPENHANS, J. 2018 *Particle Image Velocimetry: a practical guide*. 3rd Edition. Springer.

SAMIMY, M., & LELE, S.K. 1991 Motion of particles with inertia in a compressible free shear layer. *Phys. Fluids*, A3 (8), pp. 1915–1923.

SCARANO, F. 2013. Tomographic PIV: principles and practices. *Meas. Sci. Technol.*, 28, 012001.

SCHLICHTING, H. & GERSTEN K. 2016 Boundary-layer theory, 9th edition. Springer.

SIROVICH, L. 1987 Turbulence and the dynamics of coherent structures. I. Coherent structures. *Q. Appl. Maths* 45 (3), pp. 561–571.

SCHMIDT, O. & COLONIUS, T. 2020 Guide to Spectral Proper Orthogonal Decomposition. *AIAA Journal* 2020, 58:3, pp.1023-1033.

TAIRA, K., BRUNTON, S.L., DAWSON, S.T., ROWLEY, C.W., COLONIUS, T., MCKEON, B.J., SCHMIDT, O.T., GORDEYEV, S., THEOFILIS, V., & UKEILEY, L.S. 2017 Modal Analysis of Fluid Flows: An Overview. *AIAA Journal 2017*, 55:12, pp. 4013-4041.

TOWNE, A., SCHMIDT, O. T. & COLONIUS, T. 2018 Spectral proper orthogonal decomposition and its relationship to dynamic mode decomposition and resolvent analysis. *J. Fluid Mech*., 847, pp. 821–867.

VOLPE, R., DEVINANT, P. & KOURTA, A. 2015 Experimental characterization of the unsteady natural wake of the full-scale square back Ahmed body: flow bi-stability and spectral analysis. *Exp. Fluids* 56 (5), pp. 1–22.

WESTERWEEL J. & SCARANO F. 2005 A universal detection criterion for the median test. *Exp Fluids* 39, pp. 1096–1100.

WIENEKE, B. 2008 Volume self-calibration for 3D particle image velocimetry. *Exp. Fluids* 45, pp. 549-556.

Appendix A – Drawings of Ahmed body and assembly

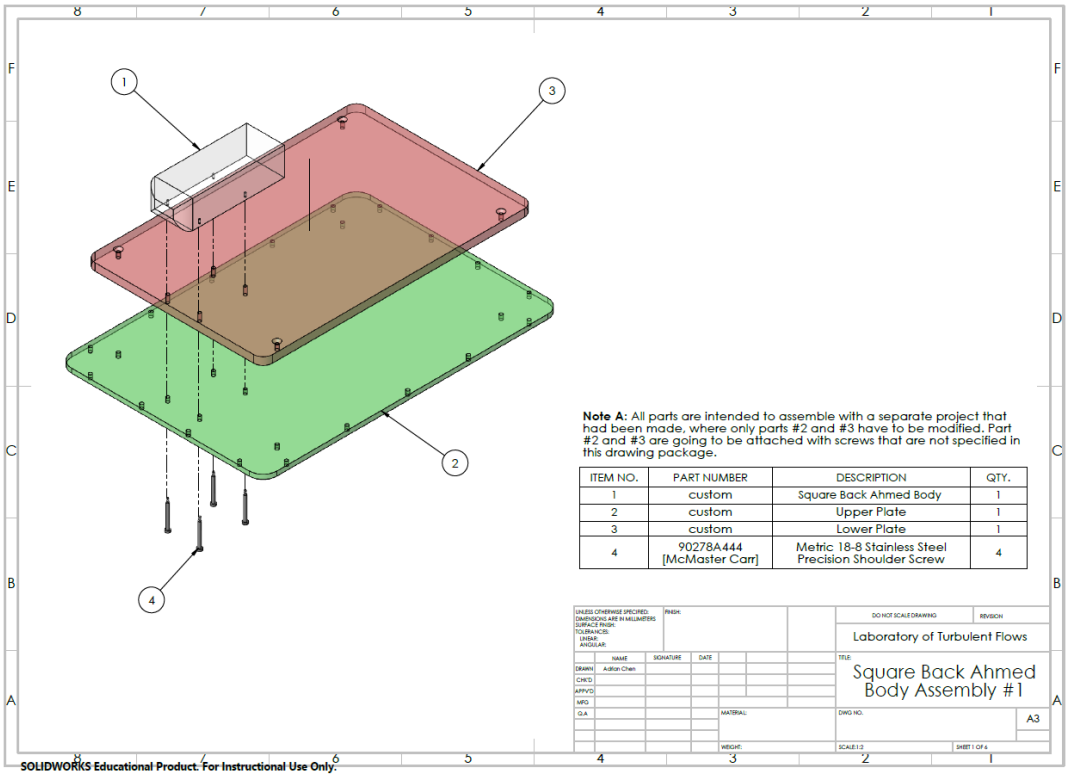

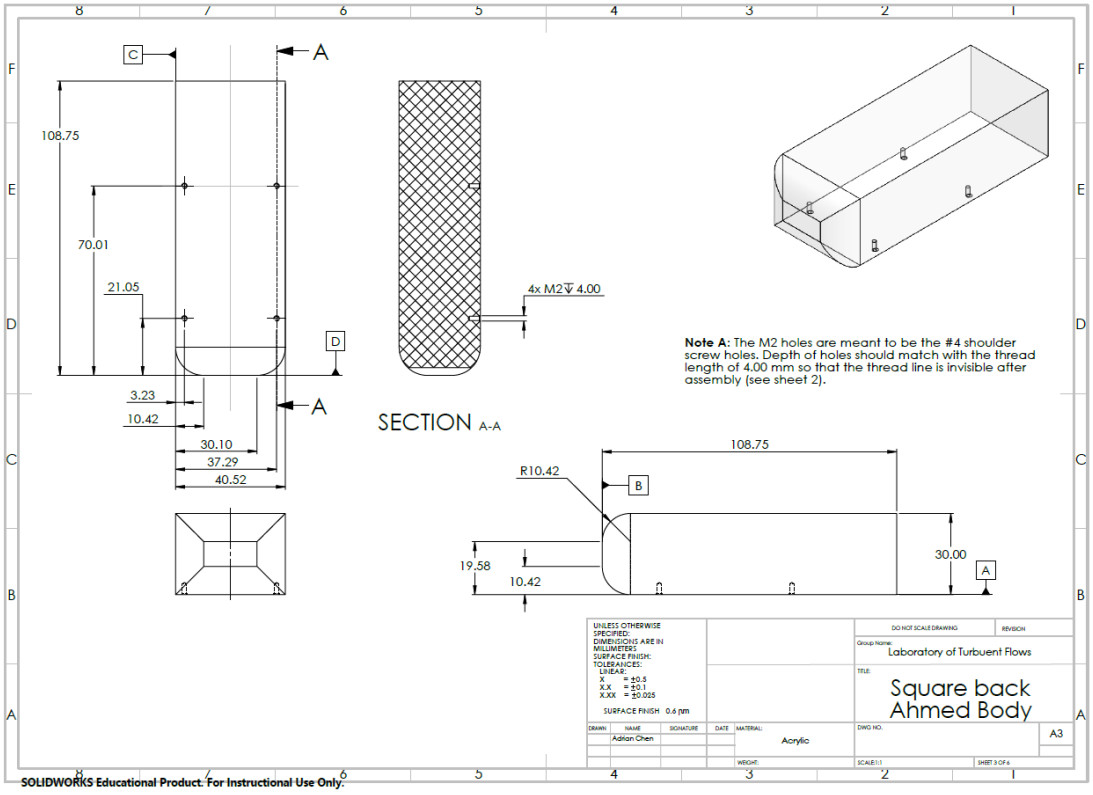

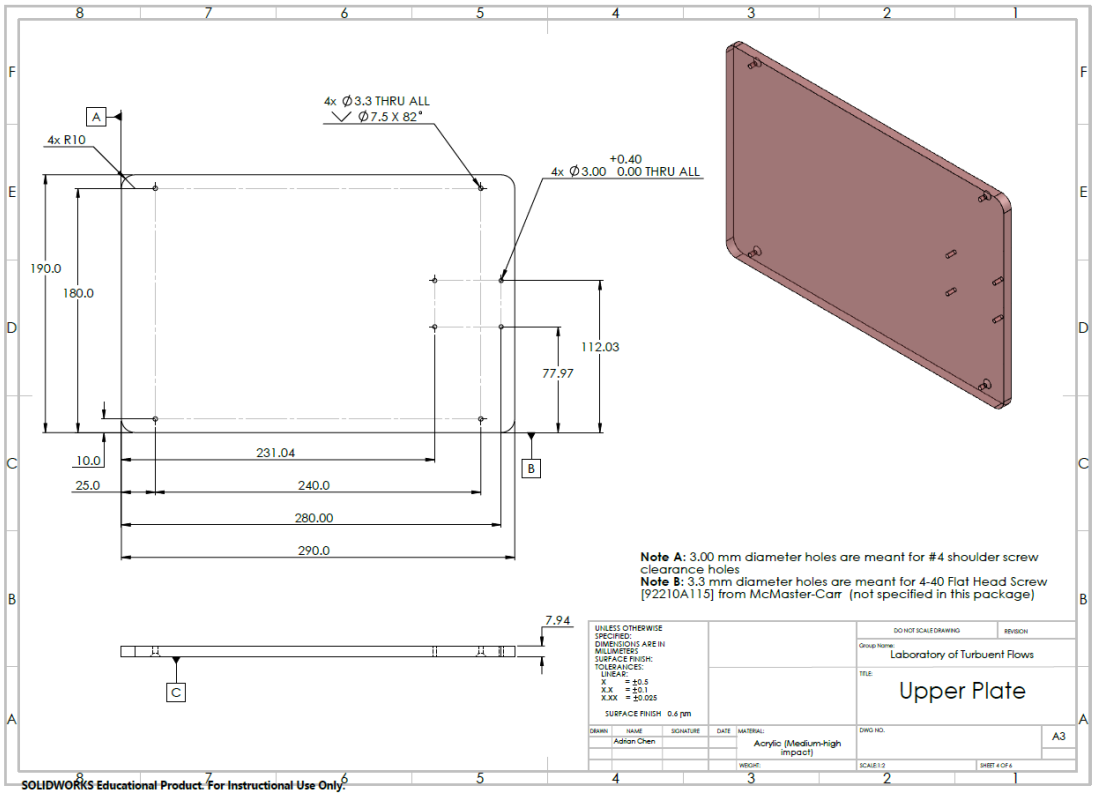
4x Ø3.3 THRU ALL
Ø7.5 X 82°
4x R10
+0.40
4x Ø3.00 0.00 THRU ALL
190.0
180.0
112.03
77.97
10.0
25.0
231.04
240.0
280.00
290.0
7.94
Note A: 3.00 mm diameter holes are meant for #4 shoulder screw clearance holes
Note B: 3.3 mm diameter holes are meant for 4-40 Flat Head Screw [92210A115] from McMaster-Carr (not specified in this package)
UNLESS OTHERWISE SPECIFIED:
DIMENSIONS ARE IN MILLIMETERS
SURFACE FINISH:
TOLERANCES:
LINEAR:
X ± 0.5
X.X ± 0.1
X.XX ± 0.025
SURFACE FINISH 0.6 µm
DRAWN Adrian Chen
MATERIAL: Acrylic (Medium-high impact)
DO NOT SCALE DRAWING
REVISION
Group Name: Laboratory of Turbuent Flows
TITLE: Upper Plate
DWG NO.
A3
SCALE:1:2
SHEET 4 OF 4
SOLIDWORKS Educational Product. For Instructional Use Only.

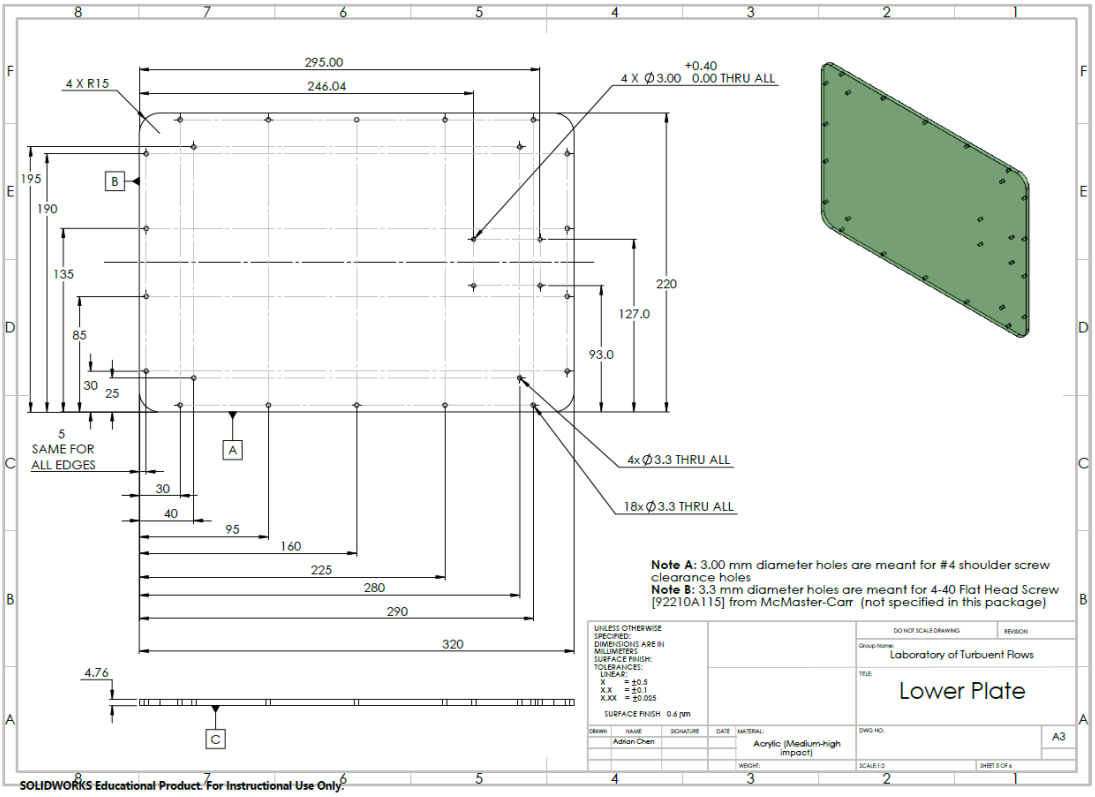
295.00
246.04
4 X R15
+0.40
4 X Ø3.00 0.00 THRU ALL
195
190
135
85
30
25
5
SAME FOR ALL EDGES
220
127.0
93.0
4xØ3.3 THRU ALL
18xØ3.3 THRU ALL
30
40
95
160
225
280
290
320
4.76
Note A: 3.00 mm diameter holes are meant for #4 shoulder screw clearance holes
Note B: 3.3 mm diameter holes are meant for 4-40 Flat Head Screw [92210A115] from McMaster-Carr (not specified in this package)
UNLESS OTHERWISE SPECIFIED:
DIMENSIONS ARE IN MILLIMETERS
SURFACE FINISH:
TOLERANCES:
LINEAR:
X ± 0.5
X.X ± 0.1
X.XX ± 0.025
SURFACE FINISH 0.6 µm
DRAWN Adrian Chen
MATERIAL: Acrylic (Medium-high impact)
DO NOT SCALE DRAWING
REVISION
Group Name: Laboratory of Turbuent Flows
TITLE: Lower Plate
DWG NO.
A3
SCALE:1:3
SHEET 5 OF 6
SOLIDWORKS Educational Product. For Instructional Use Only.

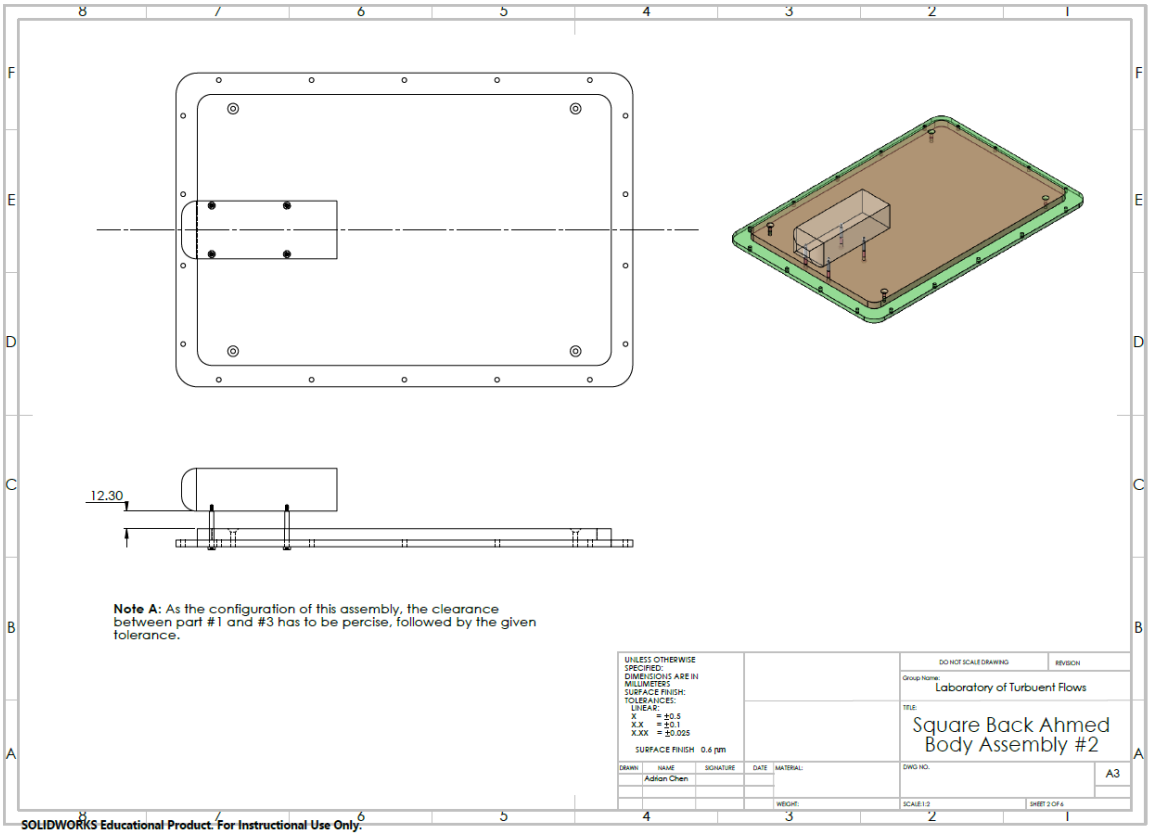
12.30
Note A: As the configuration of this assembly, the clearance between part #1 and #3 has to be percise, followed by the given tolerance.
UNLESS OTHERWISE SPECIFIED:
DIMENSIONS ARE IN MILLIMETERS
SURFACE FINISH:
TOLERANCES:
LINEAR:
X = ±0.5
X.X = ±0.1
X.XX = ±0.025
SURFACE FINISH 0.6 µm
DO NOT SCALE DRAWING
REVISION
Group Name:
Laboratory of Turbuent Flows
TITLE:
Square Back Ahmed Body Assembly #2
DRAWN
NAME
SIGNATURE
DATE
MATERIAL:
Adrian Chen
DWG NO.
A3
WEIGHT:
SCALE:1:2
SHEET 2 OF 6
SOLIDWORKS Educational Product. For Instructional Use Only.

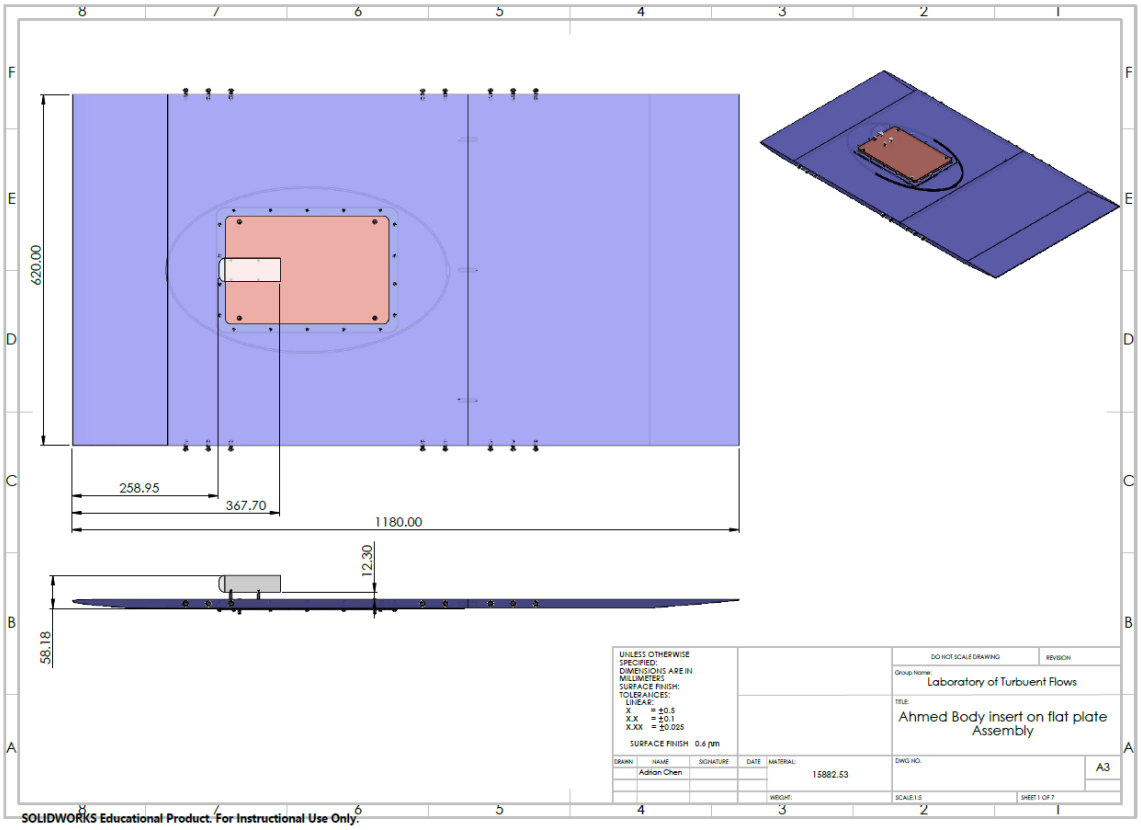
620.00
258.95
367.70
1180.00
12.30
58.18
UNLESS OTHERWISE SPECIFIED:
DIMENSIONS ARE IN MILLIMETERS
SURFACE FINISH:
TOLERANCES:
LINEAR:
X = ±0.5
X.X = ±0.1
X.XX = ±0.025
SURFACE FINISH 0.6 µm
DO NOT SCALE DRAWING
REVISION
Group Name:
Laboratory of Turbuent Flows
TITLE:
Ahmed Body insert on flat plate Assembly
DRAWN
NAME
SIGNATURE
DATE
MATERIAL:
Adrian Chen
15882.53
DWG NO.
A3
WEIGHT:
SCALE:1:5
SHEET 1 OF 7
SOLIDWORKS Educational Product. For Instructional Use Only.

Appendix B – SPOD MATLAB code

```
%%------------------------------------Spectral POD matlab code ---------------------------------------
%%s%%%%%%%%%%%%%%%%%%%%%%%%%%%%%%%%%%%%%%%%%%%%
STEP 1 –------------ Calculate and save FFT vector for step 2 -------------------
%%%%%%%%%%%%%%%%%%%%%%%%%%%%%%%%%%%%%%%%%%%%%%
clear all; close all;clc
n_block=30;                    % number of segments
n_f=3106;                      % number of frequencies or temporal length of the data
dt = 1/280;                    % delta t = 1/sampling rate (sec)
w=hamming(n_f);                % windowing function for FFT
m = 655368;                    % number of spatial dimension of tomo-PIV vector
win = repmat(w',m,1);          % create windowing function for each row of data matrix X
winWeight = 1/mean(w);         % correction factor
path_read='C:\...\SPOD\spod_X_matrix_SPOD_Blks\'; % path of experimental realizations
                                                      stored in form of segments
path_save='C:\...\SPOD\fft_matrix_SPOD\';   % path for saving the FFT realizations
f = (0:ceil(n_f/2))/n_f/dt;                 % frequency array
nfreq = length(f);
% % -------------------------- Store FFT realizations in local drive --------------------------------- %%
for i=1:n_block        % loop for FFT computations for all segments
  tic
  buff=load([path_read,'SPOD_X_Blk',num2str(i),'.mat']); % segment from path_read
  k=size(buff,1);
  buff = buff.X;                     % save segment in the variable of buff
  buff = win.*buff;                  % multiplying segment to windowing function
  buff = buff - mean(buff,2);           % subtract the mean of signals in the temporal dimension
                                                   (row)
  buff=(winWeight/n_f)*fft(buff,n_f,2);  % multiply the resulting matrix to the correction factor
   for j=[2:nfreq-1]  % loop for only the left-side spectra
      data_vector= 2*buff(:,j);        % data for a specific block and frequency
            % Multiply by a factor of 2 to correct the energy for considering only 1 sided spectra
           save([path_save,'FFTvector_Blk',num2str(i),'_fft',num2str(j),'.mat'],'data_vector','-
           v7.3');  % save FFT realization
   end
   for j=[1 nfreq]      % loop for only first and last frequency indices of the left  side spectra
      data_vector= buff(:,j);   % data for a specific block and frequency
           save([path_save,'FFTvector_Blk',num2str(i),'_fft',num2str(j),'.mat'],'data_vector','-
           v7.3');  % save FFT realization
   end
  clear buff
  toc
end
%%%%%%%%%%%%%%%%%%%%%%%%%%%%%%%%%%%%%%%%%%%%%%
```

```
%%----------------------------------Spectral POD matlab code ------------------------------------
%%s%%%%%%%%%%%%%%%%%%%%%%%%%%%%%%%%%%%%%%%%%%%%%%%%%%%%%%%%%%%%%%%%%%%%%%%%%%%%%%%%%%%%%%%%%
STEP 2 ---------- Calculate and save SPOD mode & Eigenvalues ------------------
%%%%%%%%%%%%%%%%%%%%%%%%%%%%%%%%%%%%%%%%%%%%%%%%%%%%%%%%%%%%%%%%%%%%%%%%%%%%%%%%%%%%%%%%%
clear all;close all; clc
path  = "C:\...\SPOD\fft_matrix_SPOD\*.mat"; % read path from step 1
files = dir(path);
nDFT = 3106;      % FFT length
n_block = 30;     % number of segments
m = 655368;       % length of spatial dimension
for k = 1:1554    % 1st loop for calculating SPOD modes & eigenvalues one frequency (k) at a
                        time
    tic;
    Q = zeros(m,n_block); % Create a zero matrix to storing the Fourier mode from each segment
    for i = 1:n_block  % 2nd loop for appending FFT realization at k frequency from each segment
        id =   fullfile(files(1).folder,sprintf("FFTvector_Blk"+num2str(i)+"_fft"+num2str(k)));
        buff = load(id);
        Q(:,i) = buff.data_vector; % the appended matrix Q that contains all the FFT realizations at
                                                kth frequency
    end
    CSD = Q'*Q/n_block;    % compute cross-spectra density matrix at frequency index k
    [Theta,Lambda] = eig(CSD);
    Lambda = diag(Lambda); % extract SPOD eigenvalues at kth frequency from diagonal
    [Lambda,idx] = sort(Lambda,'descend'); % sort  SPOD eigenvalues in descending order
    Theta       = Theta(:,idx);          % left-singular vector of CSD matrix
    Psi         = Q*Theta;               % SPOD modes at kth frequency
    L           = abs(Lambda);           % magnitudes of SPOD mode energy
% ----------------Store modes and eigenvalue in local drive ---------------------- %%
    save_name = sprintf('mode_eigvalue_SPOD_f%.0d',k)
    matname = fullfile('C:\Adrian\SPOD\mode_eigvalue_SPOD', [save_name '.mat']);
    save(matname,'Psi','L','-v7.3')  % save SPOD mode and eigenvalues at kth frequency
    toc
end
%%%%%%%%%%%%%%%%%%%%%%%%%%%%%%%%%%%%%%%%%%%%%%%%%%%%%%%%%%%%%%%%%%%%%%%%%%%%%%%%%%%%%%%%%
```